Macroscopic study and control of high-order harmonic and attosecond pulse generation in noble gases

PhD-thesis

EMERIC BALOGH

Supervisor:
DR. KATALIN VARJÚ
Senior research fellow
Department of Optics and Quantum Electronics, University of Szeged

University of Szeged, Physics Doctoral School

Szeged, 2014

Contents

I Introduction

The main driving force of science is our inexhaustible ambition to understand and control the world around us. People are always trying to design new tools, or push the boundaries of the existing ones to study, explain or predict yet unobserved or unexplained phenomena. As the most natural observing instruments available to us are our eyes and ears, the phenomena first studied by mankind were those that happen on the time scales these "instruments" can detect. However, our curiosity goes way beyond the scales what we can directly observe with our primary senses. This curiosity has lead our way in designing tools enabling us to reveal the hidden world of objects too small, too fast, too slow, or simply too distant to be perceived directly.

Events taking place at the very slow time scales are challenging to study, because even a whole lifetime can be too short to detect observable changes. Therefore, the study of these events requires very precise tools that can detect the smallest deviations in the signals reaching them often from very large distances. Then, by observing the generalities in their behaviour, precise predictions can be made about phenomena happening in the astronomical time scales. The study of the fastest events is a great challenge itself, and the goal of this introductory chapter is to familiarize the reader with the basic ideas behind the tools that allow researchers to study some of the fastest phenomena observable by light pulses.

In general, recording and visualizing a fast event can be done by taking still pictures of it in its different phases, then viewing these pictures in sequence gives the illusion of motion due to the phi phenomenon, hence it is called moving picture, or simply just movie. This simple idea fertilized by people's creativity gave birth to "the seventh art", called cinematography, which is still one of the most prominent meeting point of art and science. As our vision allows us to perceive and process the most information in the shortest possible time, today, movies are used not just by artists to take the viewer into their own fantasy world, but also by scientist to study or illustrate processes *measured* or *calculated* by sophisticated tools.

By the end of the 19th century the basics of the science behind photography was already available and mechanical tools were designed to capture phases of events too quick for the bare eye. These mechanical tools – now called shutters – allowed light to hit the photographic paper for just a fraction of a second, hence the picture taken showed a *frozen moment* of the event. The faster the event to be studied, the faster the shutter has to be able to react, as keeping it open for too long would result in blurring of the recorded picture. However, the speed of mechanical tools used in these experiments is limited by the relatively large inertia of its moving parts, therefore even with today's techniques, these can typically record events taking place at time scales not faster than

several microseconds (1 µs = 10^{-6} s).

The 20th century saw the very rapid growth of electronic devices that overcome this limitation by being able to be controlled using only electronic signals, eliminating the need of a mechanical shutter. As a result, the speed of these devices is limited by our expertise of controlling electronic signals in the (semi-)conductors constituting them. Hence the time resolution of these now reaches into the time scales of nanoseconds (1 ns=10^{-9} s). At this time scale even the fastest bullet would move just micrometers, so it enables the study of phenomena involving objects big enough to be observable by the bare eye. Special electronic devices – called streak cameras – are able to capture single images with picosecond integration time (1 ps = 10^{-12} s), which already allowed researchers to film a light pulse travelling in a scattering media, although the generation of such a movie requires the experiment to be repeated many times, each take capturing only a small part of a single phase of the event[1]. The response time of electronically controlled devices is currently limited to the picosecond regime, because electromagnetic pulses shorter than this cannot be transmitted through electronic circuits in today's detectors.

To record even faster phenomena other ways of taking still pictures of fast events had to be developed. Recording a picture over a relatively long time in complete darkness but illuminating the target by a very short light pulse ensures that the detector sees and records only a single phase of the event – while it is illuminated by the light pulse. By taking advantage of the fact that ultrashort electromagnetic pulses can be transmitted through air or vacuum, detectors based on light pulses initiated the next breakthrough in the available time-resolution. In this case the time-resolution is limited by the length of the light pulse, and by the precision this can be synchronized with the event in question—after all, no matter how good the picture we are taking is, if nothing is happening while it is taken. Using this method only a single phase of the event can be captured with one take, therefore the experiment has to be reproducible and repeated many times if we want to observe its time-evolution.

Ultrashort light signals became available to researchers after the invention of lasers in the middle of the 20th century. The evolution of laser technology made possible the generation of light pulses with picosecond and then even with femtosecond durations (1 fs = 10^{-15} s). As even light only travels about 0.3 mm in one ps, the processes to be studied with such high resolution involve minute particles that move very fast, like atoms under the force of electric fields. These ultrafast detection methods can thus be applied to study and control processes on the time scale of molecular reactions and they initiated the rise of a whole new research field, called *femtochemistry*[2].

This field focuses on the time-evolution of molecular processes, i.e. the motion of atomic nuclei in molecules during processes like dissociation, isomerization and other chemical reactions which take place on the femtosecond time scale. Although this field

[1] Such movies can be found for example on the MIT Media Lab's website, under "Femto-Photography".

[2] For a review and history of this topic see the Nobel lecture of Ahmed Zewail, summarized in J. Phys. Chem. A, 104, 5660-5694 (2000).

only started by researchers trying to measure the time needed for a molecule's vibrational energy to redistribute between different vibrational modes, it led to the understanding of such complex processes like the human vision. In fact, in his Nobel lecture in 1999, Ahmed Zewail (who is also known as the father of femtochemistry) stated that he believes *"every time we improve the time resolution by a factor of even a hundred or a thousand, we must be able to see new phenomena that we did not even think of"*.

Improving the time resolution further leads us to the time domain of attoseconds (1 as = 10^{-18} s), and also to smaller and faster particles interacting with these pulses and/or evolving in this time domain: the electrons. Like in femtochemistry, the study of attosecond processes promises a new, deeper level of understanding of nature and one of its most fundamental processes, the interaction of light with matter. As the formation of all molecular compounds is also governed by the Coulomb force acting on the nuclei and the surrounding electrons, it is unquestionable that the understanding of atomic and molecular processes in general also relies on understanding the motion of electrons.

Obviously, to directly study the time-evolution of these processes one needs signals which are in this time domain as well. Light pulses significantly shorter than 1 femtosecond are called *attosecond pulses* and, to date, they are the shortest experimentally demonstrated and controllably reproducible coherent light pulses available to researchers. Attosecond light pulses are synthesized from broadband extreme ultraviolet (XUV) and/or x-ray radiation, and the research field studying the generation and application of these pulses is called *attosecond science* or *attophysics*[3].

The main laboratory source of attosecond pulses today is the generation of high-order harmonics in gases by intense, femtosecond infrared laser pulses. The result of this process is a broad spectrum of XUV to x-ray radiation ending in a cutoff and containing odd harmonics of the fundamental field. The special phase-relation of these harmonics enables the synthesis of attosecond pulses by filtering out the low order harmonics from the radiation. As this process is highly nonlinear and relatively inefficient, the main focus of research today is the optimization of the generation efficiency, the isolation of a single attosecond pulse from a pulse-train, and the generation of the shortest possible attosecond pulse.

The main subject of this thesis is the numerical study of the generation of XUV radiation and attosecond pulse(train)s by the process of high-order harmonic generation (HHG) in noble gases. The first part is devoted to a theoretical introduction to HHG at both microscopic and macroscopic level while the second part enumerates the author's main research results in the subject of high-order harmonic and attosecond pulse generation.

[3]For a popular review of the research leading to the birth of attophysics see the paper of Ferenc Krausz in PhysicsWorld website, entitled "From femtochemistry to attophysics" (September 2001, pages 41-46).

II Scientific background

II.1 Background, aim and outline of this thesis

The aim of this work, which started in 2010, was to investigate high-order harmonic and attosecond pulse generation in gases by near-infrared laser pulses, with special focus on the effects of weak long-wavelength assisting fields, and on the macroscopic processes involved in the generation. In Szeged, the physics of attosecond pulse generation is a quickly developing topic, and is continuing to attract both young and experienced researchers into the city. This interest can be attributed mainly to the presence of the Extreme Light Infrastructure, a large research facility which will focus on attosecond physics and is under construction in Szeged at the moment.

I was introduced to attosecond physics in 2008 in Cluj-Napoca, where I performed the optimization of a numerical code that describes the complex, macroscopic process of attosecond pulse generation in gases. During this time I assisted a macroscopic investigation of high-order harmonic generation by mid-infrared (MIR) fields [1]. After a few adventures in interdisciplinary physics research, I arrived in Szeged with a renewed interest in attosecond science, and began working on numerical studies of isolated attosecond pulse generation by near-infrared laser pulses assisted by strong THz fields. For this purpose I used a much simpler and more intuitive model that describes the high-order harmonic and attosecond pulse generation by a single gas atom in the generating field. After a thorough investigation of this process at single-atom level [2], I continued the analysis with the 3D numerical code I got familiar with during my earlier research months in Romania [3, 4]. With this step, a long-term collaboration started between the two research groups. These results awoke interest of researchers in Max-Born-Institut, Berlin, and a 3-way collaboration still continues today, after we experimentally observed the predicted results in a similar configuration.

My research continued with the studies of THz fields on HHG, but in a different configuration: we started investigating the possibilities of using THz fields to quasi-phase-match the generated high-order harmonics. Based on the single-atom calculations I had used before, I built a one-dimensional propagation model to analyse the effect of these long-wavelength fields on the phase of high-order harmonics. This helped defining the optimal parameters of the THz field to be used in such situations and also to the understanding of the underlying physics [5, 6]. I continued the investigation of quasi-phase-matching in HHG by low-intensity assisting fields and the obtained results were collected in recently submitted paper [7].

In 2011 I was offered an opportunity to gain experience in experimental attosecond

physics in the attosecond laboratory of Lund University, Sweden. The setup has been prepared for measurements of attosecond group delays and actively stabilized to maintain interferometric accuracy of group delay measurements over long periods. I arrived at a stage when the stabilization of the system was still in progress. After reasonable stability had been achieved, we measured the variation in the group delay of attosecond pulses by changing the gas pressure in the generation cell. I assisted the research group at both preparation and measurement stages of these experiments, contributed to the analysis of the measured data, and assisted in the preparation of manuscript [8]. I also participated in experiments of photo-ionization delay measurements, summarized in a recently submitted paper [9].

Inspired by experimental advances we started another theoretical study in collaboration with Wigner Research Centre (Budapest) and Max-Planck-Institut für Quantenoptik (Garching), in which we investigated the possibilities of genetic optimisation of light-field synthesizers for attosecond pulse generation. These tools make use of a multi-parameter control over different colour ultrashort pulses, combined together to sculpt the electric field of a one-cycle pulse. I supervised the integration of a single-atom HHG model into the optimization algorithm and performed the macroscopic modelling of the process [10].

The first aim of this thesis is to provide an introduction to microscopic and macroscopic processes of attosecond pulse synthesis by HHG in inert gases. This will, hopefully, also provide the necessary theoretical background to understand both the used methods and obtained research results mentioned so far, and detailed in the second half of the thesis. To this end, in the first part, the requirement of ultrashort pulse synthesis and the main laboratory sources of XUV and x-ray radiations are briefly reviewed, also showing the main advantages of HHG in gases. Then, the theoretical background behind the generation of high-order harmonics is discussed, with special focus on the tools and models used in this thesis to study the process. Single-atom models of HHG are presented in the frame of strong-field approximation, and the main characteristics of attosecond pulses are also revealed. Macroscopic aspects of HHG are also discussed, like the main effects of phase matching, and models of quasi-phase matching. The last section of the first part presents experimental tools used to measure the duration of attosecond pulses and also to study processes on the attosecond time scale.

The second aim is to sum up the results of my research related to attosecond pulse generation in a coherent way, hopefully leading to a better understanding of macroscopic processes in HHG, especially when long-wavelength assisting fields are involved in the generation. Studies of attosecond pulse generation by laser and THz fields are presented both from a single-atom and from a macroscopic point of view, showing the advantages of using long wavelength assisting fields in HHG. Macroscopic processes arising during attosecond pulse generation by synthesized light transients are also discussed, showing the necessity of appropriate spatial filtering to obtain short, isolated attosecond pulses. Studies of quasi-phase-matching of HHG are also presented, discussing the effects of weak

assisting fields on the phase of the generated harmonics, and their ability to increase harmonic yield under unfavourable phase-matching conditions. Results obtained in group delay measurements of attosecond pulses, and their walk-off as a result of generation pressure variation is discussed in the last section of the next chapter. Finally a brief review concludes the thesis as the last chapter of the main text.

For ease of reading, in the remainder of this thesis, I shall use the word "we" as a substitute for the reader and myself, the interested scientific community, the authors of the articles I co-authored, or simply myself.

II.2 Introduction to attosecond pulse generation

II.2.1 Ultrashort pulses

The generation of short electromagnetic pulses was revolutionized by laser technology which made possible the leap from nanosecond to pico- and femtosecond time resolution. A short pulse is made from the superposition of waves with slightly different frequencies, and their phases locked to one another. The temporal and spectral structure of pulses are interrelated through the (inverse) Fourier transform:

$$\widetilde{E}(t) = \frac{1}{\sqrt{2\pi}} \int_{-\infty}^{\infty} E(\omega) e^{\imath[\omega t + \varphi(\omega)]} d\omega, \tag{II.1}$$

where $E(\omega)$ is the real spectral amplitude function, the real part of $\widetilde{E}(t)$ is the time-dependent field, and the function $\varphi(\omega)$ contains the phases of different spectral components.

A short pulse laser oscillator produces radiation with frequency components evenly distributed (called longitudinal modes) under a spectral envelope defined by the gain bandwidth of the active medium and by losses in the cavity. Such a radiation source is capable of producing short pulses, if the phase behaviour of different spectral components can be controlled. Without control over spectral phases this type of frequency comb does not produce a short pulse, but a continuous radiation with a coherence length limited by the bandwidth (like in Figure II.1.a). This type of radiation can have peaks resembling short pulses, but without the control over spectral phases these are not reproducible.

Locking the spectral phases to a constant value (e.g. $\varphi(\omega) = 0$) yields a train of short, identical pulses, with a time-shift defined by the inverse of the frequency gap[1] between adjacent spectral components ($\Delta\tau = 1/\Delta\nu$). The field in the pulse oscillates with the central frequency (ω_0) defined as the spectral centre of mass, and the oscillation is enclosed

[1]It is worth noting that the distinct spectral peaks in the spectrum of a pulse train are obviously not observable if the detector has not got the necessary spectral resolution to resolve these peaks, nor if the detector has a time-resolution superior to the time-delay between neighbouring pulses in the train. In other words, a spectrometer which is able to measure the spectrum of individual pulses in a train will record a continuous spectrum for each individual pulse, whereas a time-integrating spectrometer will record a spectrum with distinct peaks.

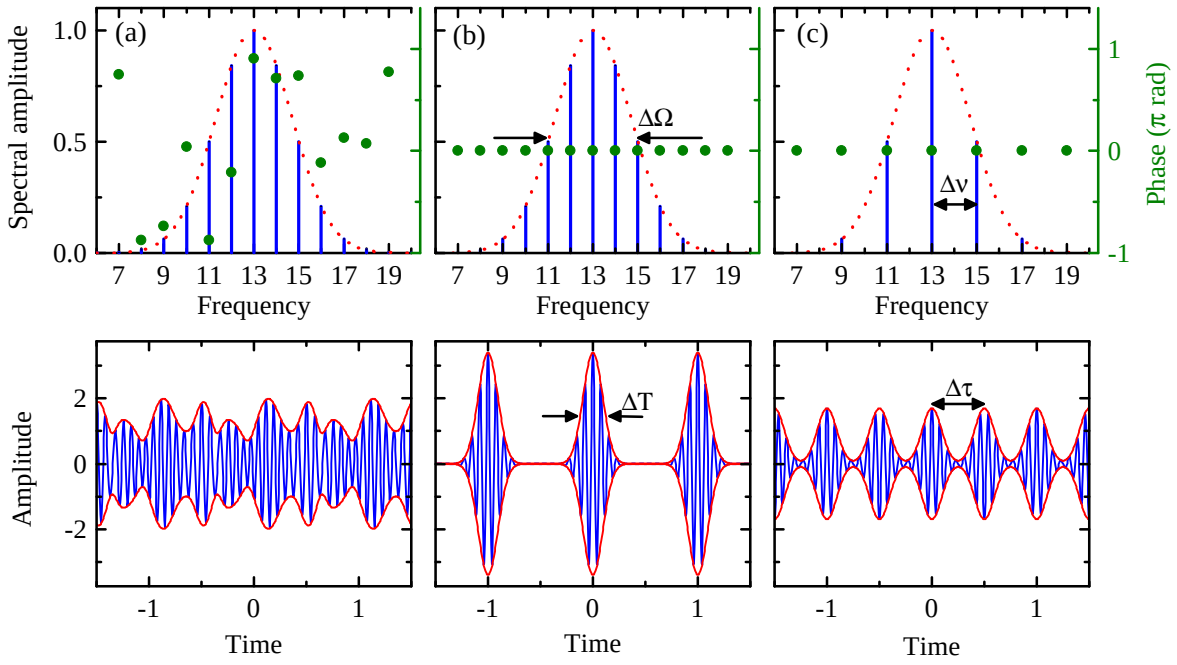

Figure II.1: *Frequency combs (top) with random (left) and locked spectral phases (middle and right), and the temporal features of synthesized pulses (bottom). Middle and right graphs show that different frequency separation between spectral peaks ($\Delta\nu$) produces pulse trains with different time-delays ($\Delta\tau$).*

under an envelope, defining the shape of the pulse(train).

A sparser frequency comb allows the generation of a pulse train with smaller time delays between individual pulses, like in Figure II.1 (b) and (c), while a continuous spectrum suggests one single pulse. The temporal width of the pulse(s) (ΔT) is inversely proportional to the spectral width of the radiation ($\Delta\Omega$). The relation between the spectral and temporal widths can be defined through the time-bandwidth product $\Delta T \times \Delta\Omega = c_b$, where the value of c_b depends on the shape of the spectrum [11]. The most widespread definition for the spectral and temporal widths are the full width at half maximum (FWHM) and the second order moment (see [11] for details).

In most of the cases the phase variation of spectral components is more complicated, requiring a more complex description. In case of smooth phase variation of a radiation with limited bandwidth, the function $\varphi(\omega)$ can be expanded into Taylor series, for example around the central frequency, and physical quantities can be assigned to the different factors:

$$\begin{aligned}\varphi(\omega)\big|_{\omega_0} &= \varphi_0 + \left.\frac{d\varphi(\omega)}{d\omega}\right|_{\omega_0}(\omega-\omega_0) + \frac{1}{2}\left.\frac{d^2\varphi(\omega)}{d\omega^2}\right|_{\omega_0}(\omega-\omega_0)^2 + \frac{1}{6}\left.\frac{d^3\varphi(\omega)}{d\omega^3}\right|_{\omega_0}(\omega-\omega_0)^3 + \dots \\ &= \varphi_0 + GD(\omega-\omega_0) + \frac{1}{2}GDD(\omega-\omega_0)^2 + \frac{1}{6}TOD(\omega-\omega_0)^3 + \dots, \qquad \text{(II.2)}\end{aligned}$$

where φ_0 is an initial phase, and the other quantities note the group delay (GD), the group delay dispersion (GDD) and the third order dispersion (TOD) of the pulse in question. These define special characteristics of the pulse: the GD represents only a shift of the

pulse peak along the time axis (see Figure II.2.a), the GDD shows the variation of the frequency in time, also causing a widening of the pulse (see Figure II.2.b) and a nonzero TOD makes the pulse asymmetric with smaller "sidewings" (see Figure II.2.c).

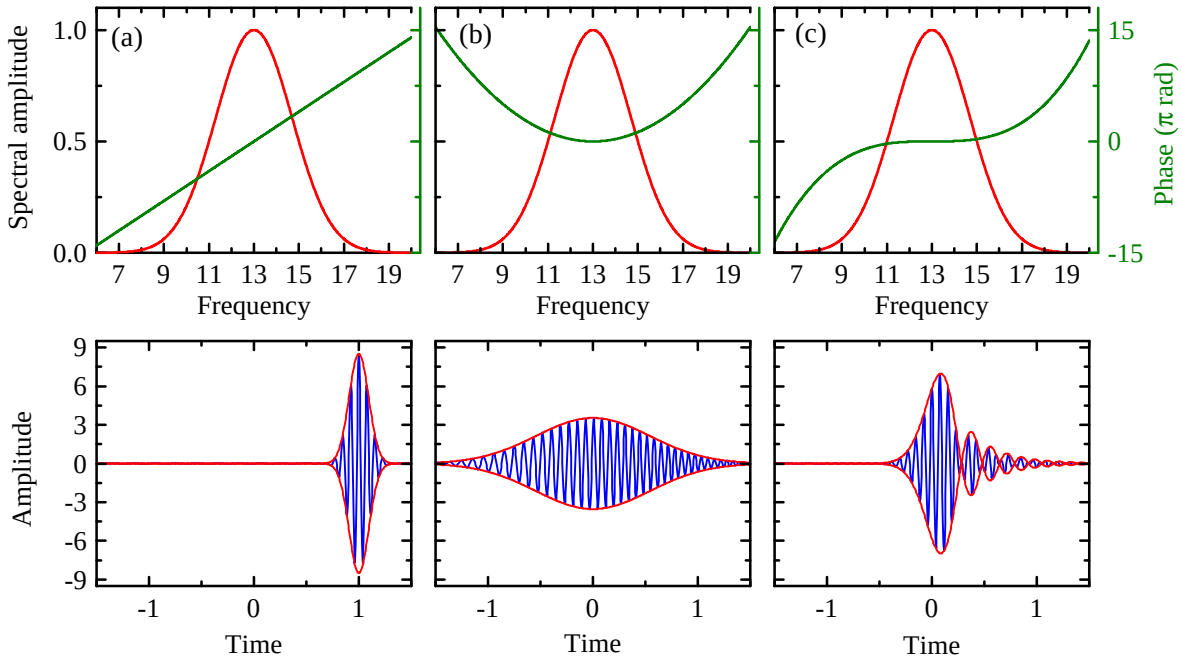

Figure II.2: *Continuum spectrum and phase (top) of three pulses with only first- (left), second- (middle) and third-order (right) spectral phases. The corresponding pulses are shown in the bottom row.*

This also shows that simply measuring the spectrum of a pulse is not enough to determine its duration. However, as it is apparent from Equation II.1, measuring the phase of individual spectral components allows the reconstruction of the complete electric field, giving all the information required to determine the characteristics of the pulse. The measurement of absolute phase is, however, not straightforward, and most measurement techniques allow the measurement of higher order phase derivatives giving access to the most important factors that determine the duration and shape of the pulse.

II.2.2 Complex representation and time-frequency map of ultrashort pulses

As the direct measurement of a laser pulse's electric field is also possible today – although requires very specialised equipment [12, 13] – and in parts of this thesis the electric field of attosecond pulses will be calculated, some of the characteristics of these pulses is discussed here and also the information obtainable from these electric fields.

In Equation II.1 it is apparent that the Fourier transform of a spectrum yields a complex, time-dependent electric field. The use of such a complex representation, although complicated and at first sight lacks a straightforward physical meaning, is very convenient in calculations, and helps the understanding of the properties of these pulses.

As it was already mentioned, the spectral amplitudes $E(\omega)$ and spectral phases $\varphi(\omega)$ contain all information about the pulse. These two independent quantities (amplitude and phase) can, however, also be represented by a single complex number (the complex amplitude) that is defined as $\widetilde{E}(\omega) = E(\omega)e^{\imath\varphi(\omega)} = E(\omega)cos(\varphi) + \imath E(\omega)sin(\varphi)$. The complex function $\widetilde{E}(\omega)$ holds information about the spectral amplitude and phase as well. These can be reconstructed as $E(\omega) = \left|\widetilde{E}(\omega)\right|$ and $\varphi(\omega) = arg\left[\widetilde{E}(\omega)\right]$, the arg function being equivalent to the $arctan$ function, but incorporating additional $\pi/2$ and π shifts depending on the sign and values of the real and complex part of $\widetilde{E}(\omega)$ (see for ex. [14] for the details).

In a similar manner, a complex electric field amplitude ($\widetilde{E}(t)$) can also be defined, that can reveal characteristics of the radiation not always apparent from the real electric field ($E(t)$). In this case the real electric field (the one that has a physical meaning and can be measured directly) is defined as the real part of the complex field ($E(t) = Re\left[\widetilde{E}(t)\right]$). By the absolute value of the complex field the envelope of the pulse is defined, and this is noted as $Env(t) = \left|\widetilde{E}(t)\right|$. This is the quantity represented by the red line in the bottom row of Figure II.2. Just like the spectral phase, the temporal phase can also be defined as $\varphi(t) = arg\left[\widetilde{E}(t)\right]$. Similarly to spectral phases, the temporal phase derivatives give us information about the pulse structure. The first derivative is essentially the instantaneous frequency $\omega(t) = \frac{d\varphi(t)}{dt}$, and the second derivative represents the "chirp" of the pulse ($\frac{d^2\varphi(t)}{dt^2}$) that is the variation of the instantaneous frequency with time. As is apparent, the chirp and GDD are also interrelated, although analytical correspondence between the two is only possible for well-defined pulse-shapes [11, 15].

Experimental measurements of the spectral amplitudes and phase-derivatives allows one to determine the complex amplitudes, and, as we have seen above, the determination of pulse envelope and the reconstruction of the complete electric field. Direct measurements of the electric field can yield the same information, and allows the calculation of the different spectral phases by the inverse Fourier transform. A basic property of the Fourier transform is that a real function is transformed to a hermitian function, meaning that the real part of the function is symmetric and the imaginary part is antisymmetric to 0 ($f(-x) = [f(x)]^*$). In our case it means that the inverse Fourier transform of the electric field produces a spectrum with positive and negative frequencies[2] having the same amplitudes and absolute phases, thus containing the same information. Thus transforming only the positive frequencies back to time domain gives us a complex electric field, and allows the study of time-frequency properties of the radiation. These calculations, although might seem simple, have limitations, as the arg function projects the phase into the $[0, 2\pi)$ domain. Due to this, especially when higher order phase derivatives are present and only

[2]Negative frequencies, in most cases, are used just for their mathematical convenience. They possess the same role as positive frequencies, just representing waves moving in another direction. For example, if we define the displacement in a harmonic oscillator as the projection of a clockwise rotating vector to the oscillator plane, then the same definition can also be applied using the same vector rotating counter-clockwise. In this case the two rotation direction can represent positive and negative frequencies, although the physical quantity they describe (the displacement) is the same in both cases.

limited density data is available, unravelling the correct phases and phase-derivatives can be tedious.

Another way of determining the characteristics of a pulse is the calculation of the Wigner distribution [16], or that of a short-term Fourier transform, like the Gabor transform [17]. The Wigner distribution, unfortunately, is not applicable to pulse trains, only individual pulses, because it requires the calculation of an autocorrelation, that introduces a cross-term (interference of separate pulses), giving misleading results [18].

The Gabor transform is free of this cross-term problem, therefore it can be applied to individual pulses as well as pulse trains [18]. In the Gabor transform, a short Gaussian window function is applied to part of the pulse, then the Fourier transform is calculated revealing the spectral components present under the applied window. By moving this window along the pulse and repeating the calculation it is possible to obtain a time-frequency map of the pulse. This transformation is defined as:

$$G(\tau,\nu) = \int_{-\infty}^{\infty} e^{-\frac{4ln(2)(\tau-t)^2}{\Delta T^2}} E(t) e^{-\imath 2\pi\nu\tau} d\tau. \tag{II.3}$$

The first exponential in the integrand represents the Gaussian window function with a FWHM of ΔT, the rest being a simple inverse Fourier transform. The value of ΔT defines the achievable time resolution of the time-frequency map. However, the use of a short window function also means that the iFT is applied to a short pulse, therefore we are introducing an uncertainty in the frequency domain. Other types of window functions can be used instead of the Gaussian, but this one has the smallest uncertainty. Based on the definition above, the frequency uncertainty of the Gabor transform is given by $\Delta\nu = 2ln(2)/(\pi\Delta T) \approx 0.44/\Delta T$.

Applying this transform to the pulses shown in Figure II.2 the time-frequency distribution shows clear signature that a linear spectral phase synchronizes all frequency components (Figure II.3.a). The positive GDD is transformed into a positive linear chirp

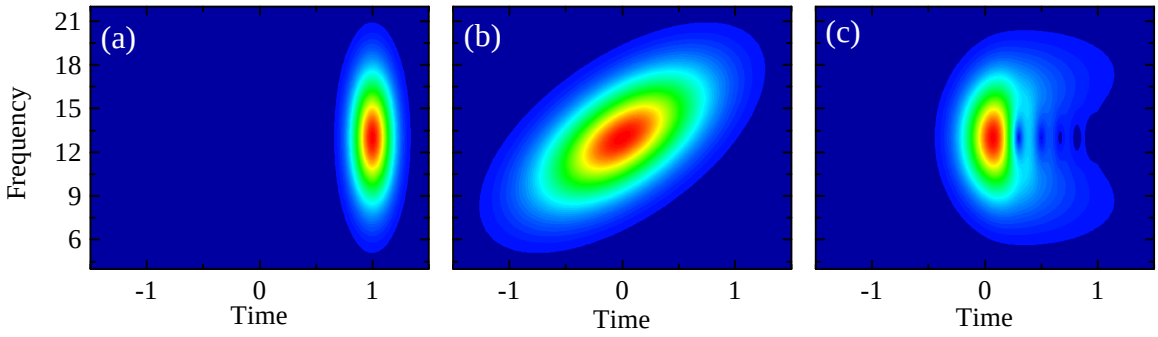

Figure II.3: *Normalized time-frequency map of pulses with linear, quadratic and cubic spectral phase (also shown in Figure II.2), calculated using the Gabor transform.*

(Figure II.3.b), showing the increasing central frequency towards the trailing edge of the pulse (at increasing time values). The positive TOD introduces asymmetric oscillations

at the trailing edge of the pulse, and the "C-shaped" quadratic time-frequency distribution is also a signature of third order spectral phase. Along the vertical, frequency axis – especially in Figure II.3.b – the distribution is widened due to the time-frequency uncertainty of the Gabor transform. Projecting the two-dimensional time-frequency map to the time axis would give information about the temporal shape of the pulses (as seen in the bottom row of Figure II.2), while projecting it to the frequency axis would reveal the characteristics of its spectrum, which is the same for all three cases.

The resolution can be increased by combining the Gabor transform with Wigner distribution calculations, yielding the Gabor-Wigner distribution that is also free of the cross-term problem (if the chosen window function is shorter than the separation between neighbouring pulses) [18].

It is apparent both from Figure II.2 and Figure II.3 that higher-order phase derivatives can increase the length of a pulse. In fact, pulses having no higher than first order spectral phase derivatives are the shortest possible for a given spectrum and are called transform limited pulses. The duration of such a pulse is the Fourier transform limit (FTL) of the spectrum. Gaussian pulses have the smallest time-bandwidth product, showing a physical limit for the shortest possible pulse for a given bandwidth[3]. As the largest achievable spectral bandwidth of a pulse is related to the central frequency, the duration of a short pulse is limited by the period of the radiation producing it (the shortest pulse consist only of a single cycle of the central frequency). For example, the widely used near-infrared (NIR) lasers producing pulses with 800 nm central wavelength have a period of $T = \lambda/c = 2.66$ fs, therefore the shortest possible pulse with this central frequency is 2.66 fs long, although when using the FWHM as a measure of pulse duration this limit can be broken slightly. Visible light (between about 400 and 700 nm wavelength) also has a period of a few femtoseconds, hence the prerequisite of attosecond pulse generation is the use of broadband, coherent UV, XUV or x-ray radiation.

II.2.3 Sources of x-rays and attosecond pulses

As argued above, high-frequency radiation is needed to produce short pulses: going into the sub-femtosecond domain requires the use of at least UV, but more preferably XUV or x-ray frequencies, a wide bandwidth and control over spectral phase. In this frequency region primary sources of radiation are mainly due to electron acceleration (or deceleration) and electronic dipole radiation: transitions from highly excited electronic states to ground state, inner-shell transitions, bremsstrahlung, synchrotron and free electron laser (FEL) radiation, high-order harmonic generation, plasma oscillation, Thomson (or Compton) backscattering, etc.

The use of electron transitions between different shells has several drawbacks. In the absence of a seed pulse it is driven by spontaneous emission (one of the two possible sources

[3]Smaller time-bandwidth products than that of a Gaussian exists, but only for different definitions than the second-order moment.

of radiation in x-ray tubes), thus the phase-behaviour of the produced spectrum cannot be controlled. Moreover, these sources usually have a limited bandwidth making them more suitable for the generation of longer pulses and, as a result, their development is concentrated around techniques that improve their spatial and temporal coherence rather than short pulse production.

Bremsstrahlung (the other source in x-ray tubes), produced by decelerating electrons, can emit radiation with a wide bandwidth, however this is also an incoherent process, therefore not suitable for controlled short-pulse generation.

X-ray lasers

In the visible and IR region mode-locked lasers revolutionised ultrashort pulse generation, but it is not straightforward to transform the concept to the x-ray regime. The most widespread gain materials in this frequency region are hot dense plasmas, and a population inversion in these can be kept only for picoseconds. Moreover they would very quickly destroy any optics in their vicinity. The short lifetime of excited states combined with high photon energies causes the pump energy requirement to scale with the central frequency as ω^5, making x-ray lasers very demanding and impractical [19].

The main difficulty with short pulse production from these lasers, however, is not the large pump energy requirement, but the lack of mode synchronization, which, in general requires an oscillator or pre-seeding of the XUV generation process. Oscillators that can achieve mode-locking require a relatively long lifetime gain medium (the laser pulse has to travel back and forth in the oscillator at least several times before the gain is depleted) and high reflectivity mirrors, therefore this is not straightforward to achieve in this region, and usually x-ray lasers rely on single-pass amplified spontaneous emission.

Synchrotrons, free-electron lasers and Thomson backscattering

These (and several other) limitations drove scientists to develop other sources of broad-band XUV and x-ray sources. In free-electron lasers and modern synchrotrons x-rays and gamma rays are generated by a high-energy electron beam being steered into an undulator or wiggler (a series of magnets with alternating poles) that makes the relativistic electrons oscillate in the periodically alternating magnetic field. The oscillating electrons emit a radiation whose properties depend on that of the electron beam, the strength of the magnetic field (distinguishing the undulator and wiggler regime) and on the density of magnetic pole switches. There are great advantages in using relativistic electron beams (the electron bunch travels through the undulator with a velocity close to speed of light), as this narrows the radiation cone and increases the frequency of the produced radiation due to both Lorenz contraction and Doppler shift [19]. The length of the generated pulse in this case depends on the length of the electron bunch, and, although there are proposals for short pulse generation, to date, the shortest pulses generated this way are still of the order of 10 fs [20], and their precise synchronization (below $\approx$100 fs precision) with other

sources is still not resolved [20, 21].

Another way of x-ray generation is by undulating the electron beam using counter-propagating laser pulses instead of periodic magnets [22, 23, 21]. This technique is usually referred to as Thompson (or Compton) backscattering, and has several advantages over "traditional" FELs, like the short wavelength of the laser field (≈µm) that is not possible to achieve with magnets in undulators. This technique, however, is still very much in the development stage, and only very few research groups have the capability of generating relativistic electron beams and synchronising them with high-intensity laser pulses.

High-order harmonic generation on solid surfaces

A promising way of pulsed x-ray generation is the interaction of intense ultrashort laser pulses with solid targets. Depending on the laser intensity there are two mechanisms that result in the generation of high-order harmonics of the fundamental laser field, called coherent wake emission (CWE) and relativistic oscillating mirror (ROM) [24]. In both cases the leading edge of the laser pulse ionizes the surface of the solid target generating a dense plasma that reflects the incident laser beam (plasma mirror).

The free electrons oscillate in the laser field, and, upon returning to the surface they can induce plasma oscillations at a characteristic frequency (plasma frequency) which produce high-order harmonic radiation (CWE). The plasma frequency changes with the free electron density, and the steep gradient of the plasma density allows the generation of different harmonics close to the surface. This mechanism is the dominant source of harmonic emission below relativistic intensities [25].

At intensities which can accelerate electrons to relativistic velocities ($> 1.37 \times 10^{18}$ Wcm^{-2}µm^2) a new mechanism appears [24]. In every optical cycle of the laser field, relativistic electrons leave the surface of the target and reflect the incident beam. Due to Doppler shift, the reflected beam now contains x-ray bursts separated by one optical cycle (ROM harmonics).

Generation of high-order harmonics on solid surfaces has the advantage that it has not got a known upper limit to the applicable laser intensity, therefore it is a possible source of very bright x-rays. This process is under intense investigation, and it might, one day, be a widespread method for attosecond pulse generation. However, because of the large intensities required to produce these harmonics, the large divergence of the generated radiation, the technical difficulties risen by the need for "fresh" solid surface at every laser shot and the challenges in stabilization of the beam reflected from the moving surface, these methods of x-ray generation are still not widespread, and limited to smaller repetition rates.

High-order harmonic generation in gases

Today, attosecond pulses are most widely generated by the process of high-order harmonic generation in gas targets [26]. This mechanism produces XUV to x-ray photon energies

with very wide bandwidth and excellent temporal and spatial coherence. It is demonstrated that this process works at very high repetition rates (≈MHz) and can produce attosecond pulses [27], although with relatively low efficiency. Due to this, it is actively researched not just for its direct applications in attophysics, but also for its possible use in generating seed pulses for some of the more efficient schemes which are able to produce very intense radiation, like FELs or x-ray lasers [28].

In this scheme an intense, femtosecond, IR laser pulse is focused into a gas cell or jet placed inside a vacuum chamber. The vacuum is needed to prevent: 1) the destruction of

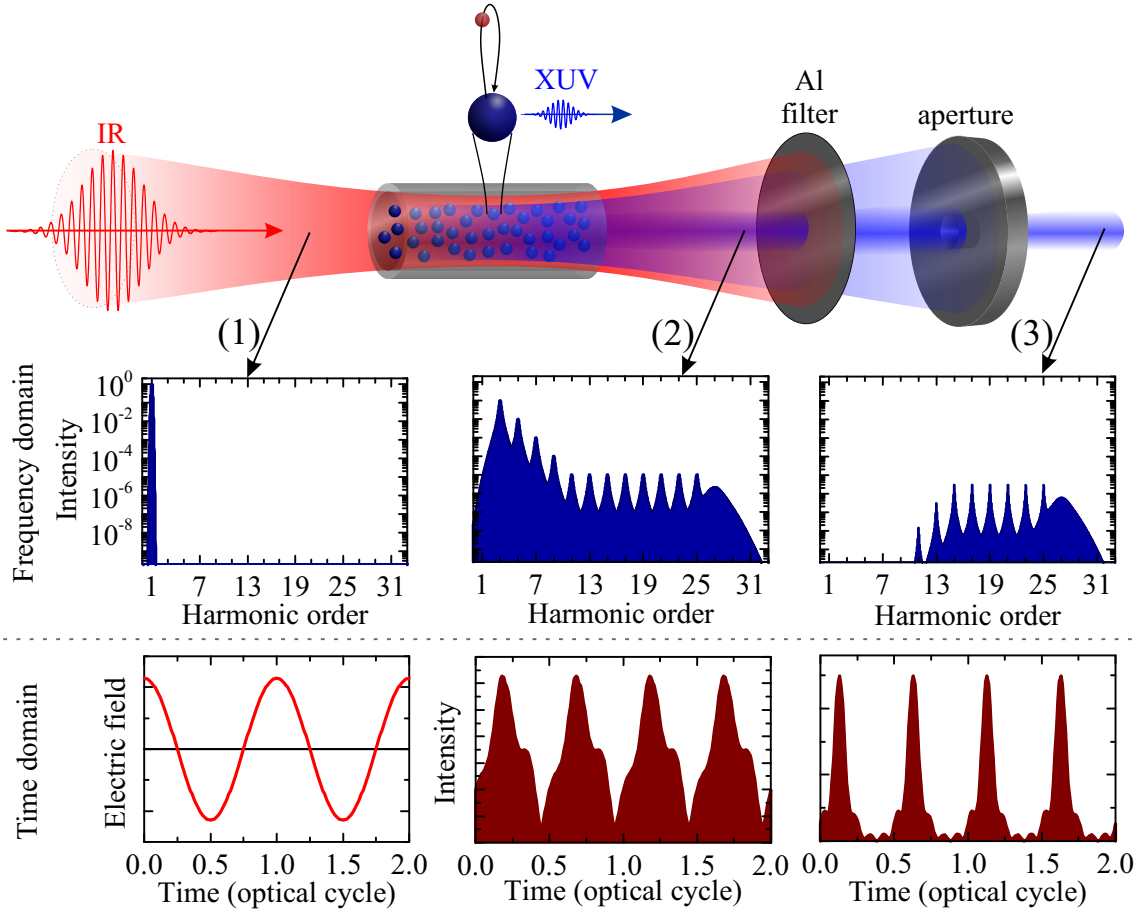

Figure II.4: *Schematic representation of high-order harmonic generation. Spectral and temporal structure of the (1) laser and (2) generated radiation before filtering. (3) Harmonic spectrum and attosecond pulses after spectral and spatial filtering. Temporal intensities are not to scale.*

the pulse before the focus by nonlinearities in air, and 2) the absorption of the generated radiation. The gas jet (or cell) contains a gas with high ionization potential (in most cases a type of noble gas), that can withstand intense laser radiation without complete ionization. Through interaction of the laser pulse with gas particles, high-order harmonic generation takes place inside the gas cell, and the unconverted laser pulse and the harmonic beam leave the target gas together. At this point, the spectrum is dominated by the low-order harmonics, hence the duration of the pulses is in the femtosecond domain (see (2) in Figure II.4). After leaving the target cell, a thin metallic foil (Aluminium, Zirconium etc.) blocks the IR beam and also the low-order harmonics while letting the XUV beam

through [29]. An aperture is usually used to block the divergent part of the beam [29]. The remaining harmonic beam – now collimated and free of low-order harmonics – contains a train of attosecond pulses (see (3) in Figure II.4), which can be manipulated with specialised XUV optics and used in applications. The processes taking place in the gas cell are discussed in the next sections, and, in fact in most of this thesis.

II.3 Single-atom description of high-order harmonic generation by ultrashort infrared laser pulses

The subject of this thesis being the study of HHG in noble gases by infrared laser fields, the physics leading to the understanding of this process is discussed in this section. In this area of physics some approximations are straightforward, and these are used in the descriptions to follow. The major approximations used are the following: (1) the laser frequency is far from any resonant transition of the gas in which HOHs are generated, (2) the laser intensity is low enough so that relativistic effects, and the effect of its magnetic field on the wiggling electrons are negligible, and (3) the wavelength of the generated harmonic radiation is significantly larger than the atom emitting it (called dipole approximation).

To introduce the used models we summarize very briefly the perturbative approach to light-matter interaction, then discuss the corrections needed to describe intense pulses propagating through gaseous media and the appearance of high-harmonics in this regime. Major part of this section is devoted to the description of HHG by the interaction of intense laser field and a single atom.

II.3.1 The breakdown of perturbative description

The complexity of the description of light-matter interaction greatly depends on the intensity of the light and the type of material in question. At low intensities, in non-magnetic, dielectric materials, far from resonant transitions, light-matter interaction is well characterized by the electronic susceptibility, responsible for the refractive index, the relation being $n = \sqrt{1+\chi}$. In a simplistic model, the polarization of the matter follows the electric field of the light – just like a forced, damped, harmonic oscillator – continuously absorbing and re-emitting radiation with different phases set by the sum of contributions from all resonant frequencies. In this approximation the magnitude of the generated polarization is given simply as $\boldsymbol{P} = \epsilon_0 \chi \boldsymbol{E}$. As a result, light only experiences a phase shift, macroscopically observable as a matter specific phase velocity described by the refractive index. The magnitude of the interaction and the phase shift itself depends on the frequency offset from the resonant transition, hence the refractive index is itself frequency dependent. This causes the phenomenon called dispersion, transforming the phase behaviour ($\varphi(\omega)$) of the radiation passing through the material.

The above description explains phenomena apparent at low light intensities, where the

strength of the light electric field is much lower than the fields binding the electrons to the core, and can be considered a weak perturbation. With the invention of lasers the analysis of light-matter interaction at high intensities became possible, and the study and use of nonlinear interactions became common in laser laboratories. At higher intensities the polarization of matter is not following the light field directly, and the previous description needs refinement. Still, treating the external field as a perturbation, and expanding the susceptibility into Taylor series, an accurate description of laser matter interaction at moderate intensities becomes possible. The generated polarization now becomes

$$\boldsymbol{P} = \epsilon_0 \chi^{(1)} \boldsymbol{E} + \epsilon_0 \chi^{(2)} \boldsymbol{E}^2 + \epsilon_0 \chi^{(3)} \boldsymbol{E}^3 ... \tag{II.4}$$

Higher orders of the Taylor series become significant at increasing field strengths, the step size between orders being a characteristic of the material, and depending on the field strengths electric charges experience inside it [11, 30]. As a result, the contribution to the final polarization of different order susceptibilities usually decreases very quickly[4]. Even order susceptibilities are present only in atomic structures without inversion symmetry [30], and they are responsible for processes like second harmonic generation and frequency mixing. As a result, the first nonlinear processes observable in monatomic gases are described by the third order susceptibility ($\chi^{(3)}$), responsible for the optical Kerr effect and third harmonic generation for example.

Further increasing the laser intensity the Taylor expansion of the susceptibility fails. At field strengths which cause dielectric breakdown of the material, free electrons appear and disturb the propagation of light pulses. In noble gases irradiated by IR pulses this can be caused by multiphoton or optical ionization of the atoms, requiring field strengths comparable to the Coulomb field binding the valence electron to the atomic core. At these high intensities, electrons can tunnel into the continuum, creating a plasma that changes the interaction of laser with matter significantly. In noble gases this process becomes observable at laser intensities as "low" as 10^{13} W/cm^2 in Xenon, and slightly higher for others with higher ionization energies.

At these intensities the generation of harmonics above 15th order were observed already at the end of the 1980s using both ultraviolet and infrared lasers [31, 32]. The first HOH spectra recorded showed an interesting characteristic: after the first few harmonics with perturbatively decreasing intensity, a plateau was observable containing odd harmonics with similar intensities, and ending in a sharp cutoff. These high harmonics (especially above the ionization energy) with constant amplitude are not explained by perturbation theory, thus it was clear that new approaches were necessary to describe the phenomenon.

The accurate description of light-matter interaction would be the solution of the time-

[4]It is worth noting that an nth order susceptibility is not a simple number, but an $n+1$th order tensor, thus (depending on the order) giving a polarization vector that is sensitive not just to the amplitude but the phase and polarization of the E vector and also to possible combinations of different E vectors (for more details see [30, 11]).

dependent Schrödinger equation for the atomic response coupled with Maxwell's equations for the electromagnetic wave. This, however, is computationally demanding, and the extraction of illustrative and intuitive physics behind the process is very challenging. Just as the approximation of the matter's response by susceptibility proved very useful for the low-order harmonics, in HHG there are also simplified models, which, depending on their complexity, can give different levels of understanding of the process. In the next sections we present some of the most widespread models of HHG in gases used today, starting from the simplest semi-classical model, and advancing to strong field approximation.

II.3.2 Classical model of HHG

The first successful model that explained the process in an intuitive manner used an approach from plasma physics: it assumed that the laser field forces the electrons into continuum by tunnelling ionization, and there they move in the field of the laser, unaffected by the Coulomb field of the parent ion [33, 34]. This approach then gained the name of classical or three step model of HHG.

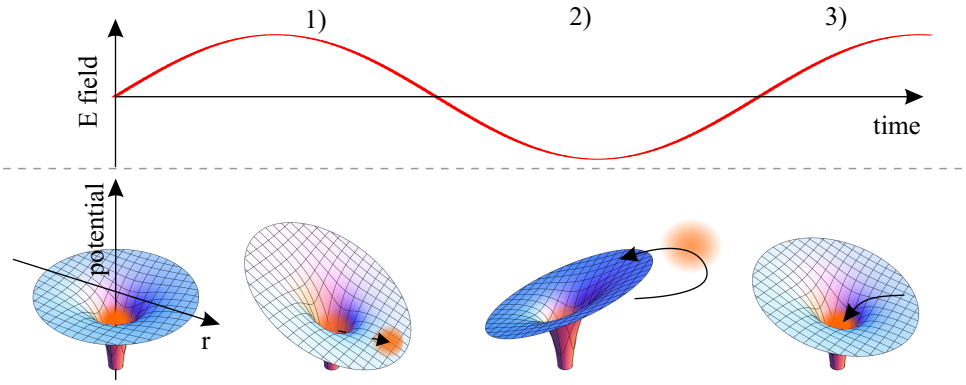

Figure II.5: *Scheme illustrating the initial state of the system (left) and the three steps of the HHG process.*

This model is based on the fact that the laser electric field strengths used in HHG are already comparable with the Coulomb field acting on the outermost electron. Together they create a potential barrier through which electrons can tunnel into the continuum, and quickly departing from the ionic core they become unaffected by the Coulomb field so their movement in the laser field can be treated classically. As they oscillate in the laser electric field, some of them re-encounter the parent ion, recombining and releasing their energy in form of a high-harmonic photon. In this simple model a few assumptions are made: 1) the electrons appear in the continuum very close to the nucleus with 0 initial velocity, 2) after ionization, the motion of the electrons in the continuum is governed by Newton's equations, while the classical laser electric field is the only force acting on them, 3) if the electrons re-encounter the core, they emit a photon, whose energy is the sum of the electron's kinetic energy at the moment of recombination and the ionization energy.

Using these assumptions, some of the most fundamental properties of HOHs can be calculated. Taking a linearly polarized laser electric field with amplitude E_1 and angular

frequency ω_1, described as

$$E(t) = E_1 \, cos(\omega_1 t + \varphi_0) \tag{II.5}$$

causes the electron to wiggle with an average kinetic energy of

$$U_p = \frac{e^2 E_1^2}{m_e \, \omega_1^2}, \tag{II.6}$$

where e and m_e are the electron charge and mass respectively, and U_p is called the ponderomotive energy.

Depending on the instant the electron "appears" in the continuum, it may drift away, producing above threshold ionized (ATI) electrons, or return to the nucleus, recombining and emitting a harmonic photon[5]. The highest kinetic energy at the moment of first return is calculable to be $3.17U_p$, which explains both the presence and position of the sharp cutoff observed in the experiments, and shown to be at $I_p + 3.2U_p$ [35].

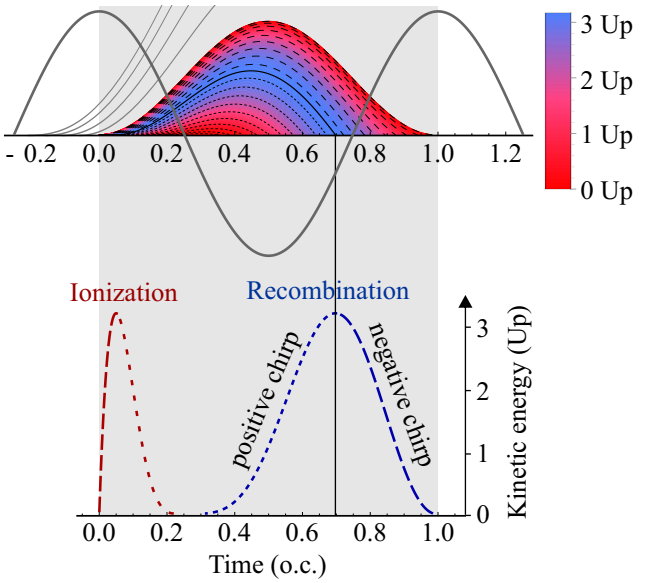

Figure II.6: *Electron trajectories (top) calculated from the classical model with final kinetic energies shown by colour-codes. On the bottom the ionization times (red lines) and return times (blue) of short (short dashed) and long (long-dashed) trajectories is also shown.*

The instant of ionization unambiguously determines the electron trajectory, its possible time of return and final kinetic energy. The process has half-cycle periodicity, and in a single half-cycle there are two possible paths with the same final energy (except for the cutoff). The two electron paths producing the same energy radiation are called short and long trajectories, the long ones starting earlier and returning later. The distribution of the return energy as a function of electron trajectory is also illustrated in Figure II.6. These properties of the returning electron are transformed to the generated photon, defining its "emission time" and photon energy ($h\nu = I_p + E_{kin}$) . As a result the harmonic radiation resulting from short (long) trajectories possesses an intrinsic positive (negative) chirp.

[5]Upon re-encountering the ionic core the electrons can also rescatter, and elastically rescattered electrons driven by the laser field produce the long second plateau of the ATI electron spectra.

Already at the dawn of HHG studies it was shown that longer wavelength fields can produce harmonics with higher photon energies [36]. This model (more precisely Equation II.6) also explains why the position of the cutoff increases with the second power of the generating field's wavelength, showing the main advantage of longer wavelength IR and MIR pulses in HHG. As a result, although ultraviolet lasers have been used since to produce HOHs [37] and excimer UV lasers remain useful in high-efficiency generation of low-order harmonics with femtosecond durations [38, 39], the most widespread tools for HHG are still near- and mid-infrared femtosecond lasers [40, 41].

This classical model proved to be very valuable in understanding the fundamental physics of HHG, but it is unable to account for any quantum-mechanical effects, which are clearly present in all three steps of the process. Therefore, more accurate descriptions are needed to study the properties of the generated radiation.

II.3.3 Strong-field approximation

One of the most successful quantum-mechanical treatments of the process was introduced by Lewenstein et al. [42], known as the strong field approximation (SFA) model of HHG. The derivation of this model is rather involved, and the interested reader can find it in [42, 43], or a rather detailed description in chapter 5 of [44]. Below the approximations and steps leading to the final result – that is the time-dependent dipole moment of a model atom generated by a strong, long-wavelength laser field – are briefly discussed. Atomic units are used in this section.

The Lewenstein integral

Further approximations (to those mentioned in the beginning of section II.3) used in the SFA model are [42]: 1) there is a single active electron in the ground state, and the contribution from all excited states is negligible. 2) the population-depletion of this state during the interaction can be neglected. 3) the electron in the continuum can be treated as a free particle, under the influence of the laser electric field.

As discussed by Lewenstein et al., these approximations hold in the strong-field regime, characterized by a Keldysh parameter ($\gamma = \sqrt{I_p/2U_p}$) smaller than one[6], showing that the application of SFA model requires a laser intensity and wavelength to satisfy $2U_p > I_p$.

Under these assumptions, and treating the continuum electron wavepacket as a plane

[6]The Keldysh parameter distinguishes the strong-field interaction regimes based on the ratio of U_p and I_p. Initially it related the "classical" tunnelling time for the given potential barrier to the laser oscillation period (lifetime of barrier). Although the tunnelling time has more than half a dozen different definitions [45] and it is an ongoing debate if such a time delay actually exists or not [46, 47], in the region of $\gamma < 1$ the SFA model produces good results for HHG by NIR and MIR fields.

wave (Volkov state), the time-dependent dipole moment can be calculated as [42]:

$$x(t) = 2Re\Big\{\imath \int_{-\infty}^{t} dt' \Big(\frac{\pi}{\epsilon + \imath(t-t')/2}\Big)^{3/2} E(t') d^*[p_s(t',t) - A(t)] d[p_s(t',t) - A(t')] \times exp[-\imath S_s(t',t)]\Big\}, \tag{II.7}$$

where $E(t)$ and $A(t)$ denote the time dependent electric field and vector potential of the laser pulse, $d(p)$ denotes the atomic dipole matrix element for the bound-free transition, ϵ being a small positive number to remove the singularity at $t = t'$, while p_s is the stationary point of the canonical momentum, and $S(t', t)$ is the quasi-classical action defined as:

$$S(p_s, t', t) = \int_{t'}^{t} \left(\frac{[p_s + A(t'')]^2}{2} + I_p \right) dt''. \tag{II.8}$$

The stationary point of the canonical momentum selects the contributions to the dipole moment of those electrons which have appropriate initial momentum at t' to return to the nucleus at t:

$$p_s(t', t) = \frac{1}{t - t'} \int_{t'}^{t} A(t'') dt''. \tag{II.9}$$

The transition probabilities can be determined for known electron states. For a hydrogen-like ground state, with I_p ground-state energy, the transition probability is approximated by [48]

$$d(p) = \imath \left(\frac{1}{\pi 0.8 I_p} \right)^{3/4} \frac{p}{0.8 I_p} exp\left[\frac{-p^2}{2 \cdot 0.8 I_p} \right]. \tag{II.10}$$

In the following Equation II.7 will be referred to as the Lewenstein integral. These equations can be calculated analytically for some specific electric fields, and numerical calculations can be performed on any type of field, described either analytically or numerically. This freedom makes the use of the Lewenstein integral very convenient in numerical models.

From the dipole moment $x(t)$ the dipole spectrum $x(\omega)$ can be calculated by Fourier transformation Figure II.7.

$$\widetilde{x}(\omega_q) = \frac{1}{\sqrt{2\pi}} \int_{-\infty}^{\infty} x(t) e^{-\imath \omega_q t} dt. \tag{II.11}$$

The source of the produced radiation is the dipole acceleration, which is proportional to $\widetilde{h}(\omega_q) \propto \omega_q^2 \, \widetilde{x}(\omega_q)$. Attosecond pulses are then obtained by filtering out the low order harmonics – as is done in experiments – and inverse Fourier transforming the remaining part of $\widetilde{h}(\omega_q)$.

For a quasi-monochromatic generating field, equally spaced odd harmonics of the fundamental are obtained, as one expects from any centrosymmetric system. By calculating the temporal structure of the radiation from the plateau region one gets two attosecond

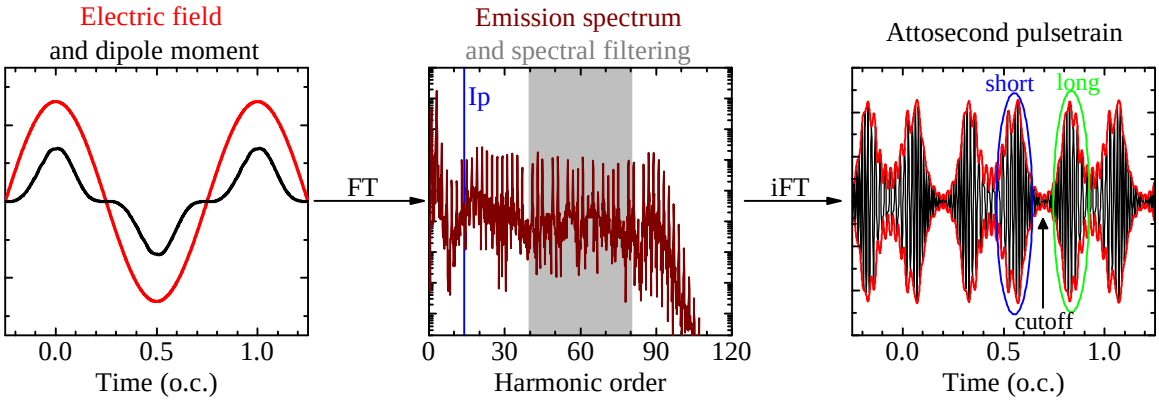

Figure II.7: *Dipole moment (left), harmonic spectrum (middle, on logarithmic scale) and attosecond pulses (right) calculated using the the Lewenstein integral. Attosecond pulses are synthesized from the middle plateau region of the spectrum, hence at the expected position of the cutoff there is a gap separating the pulses from short and long trajectories. 800 nm quasi-monochromatic laser pulse is used with* 6×10^{14} *W/cm*^{2} *intensity.*

pulses in every half-cycle of the fundamental. As is apparent from Figure II.7, the subsequent pulses are delayed and possess opposite chirp, in accordance with the classical model that showed the presence of short and long trajectories constituting the high-order harmonic radiation.

Saddle-point approximation of the Lewenstein integral

Further approximations can be used to calculate the dipole spectrum also helping to gain further insight into the process [42, 48]. By inserting $x(t)$ from Equation II.7 to Equation II.11, a double integral (over t and t') is obtained, with an integrand having an exponential with a phase factor of $\Phi(p_s, t, t') = \omega_q t - S(p_s, t, t')$. Integrals of this type can be approximated using the saddle point method [49], according to which the main contributions to the final result arise from the saddle-points of the exponent[7], namely at (t, t') points where $\nabla\Phi(p_s, t, t') = 0$. This means that the approximation of this integral involves the search for those values of t and t' which satisfy:

$$\left.\frac{\delta\Phi}{\delta t'}\right|_{t'_s} = \frac{(p_s - A(t'_s))^2}{2} + I_p = 0, \tag{II.12}$$

$$\left.\frac{\delta\Phi}{\delta t}\right|_{t_s} = \omega_q - \frac{(p_s - A(t_s))^2}{2} - I_p = 0. \tag{II.13}$$

With n number of different saddle points for a given final photon energy (ω) the value

[7]The saddle-point method is an extension of the Laplace method to the complex Ω plane. The Laplace method is an asymptotic expansion of integrals of type $F(\lambda) = \int_\Omega f(x)e^{\lambda S(x)}dx$, that uses a Taylor expansion of the $S(x)$ function to approximate the value of the integral by transforming it to Gaussian-type integrals. It is discussed for example by A. Erdélyi [50], and by M. Dahlström et al. who focused on its applications in attosecond physics [51].

of the Equation II.11 is approximated as

$$\widetilde{x}(\omega_q) = \sum_n \frac{\imath 2\pi}{\sqrt{det(-\Phi'')}} \Big(\frac{\pi}{\epsilon + \imath(t-t')/2}\Big)^{3/2} E(t') d^*[p_s(t',t) - A(t)] d[p_s(t',t) - A(t')] \\ \times exp[-\imath S_s(t',t) + \imath\omega_q t], \tag{II.14}$$

where Φ'' denotes the Hessian matrix containing the second order partial derivatives of $\Phi(p_s, t, t')$ around the saddle points. Its determinant takes the following form[8]

$$det(-\Phi'') = \left[\frac{\partial^2\Phi}{\partial t \partial t'}\right]^2 - \frac{\partial^2\Phi}{\partial t^2}\frac{\partial^2\Phi}{\partial t'^2}. \tag{II.15}$$

Calculating the derivatives around the saddle points and inserting it to Equation II.14 gives the spectral amplitudes of the harmonic in question.

Equations II.12,II.13 and II.9 have nice physical interpretations, enforcing energy conservation during ionization and recombination, and also showing that the electron has to return to the core to emit a photon, proving the basic assumptions of the semi-classical model.

These solutions can also be interpreted in the frame of Feynman's path integral formalism of quantum mechanics [52]. It has been discussed that the HHG photon emission is a result of the coherent sum of all possible quantum orbits (trajectories) weighted by their probability factor, the most probable quantum orbits being those that satisfy equations II.9,II.12 and II.13, their probabilities given by the product of ionization and rescattering probability taking into account the diffusion of the continuum electron wavepacket.

From a practical point of view, the saddle point approximation has the disadvantage that equation Equation II.13 can only by satisfied by complex p_s or A values, which arise only from complex time instants. As a consequence, the functions $E(t)$ and $A(t)$ have to be defined for complex variables, enforcing the use of analytically defined laser electric fields in the calculations.

For the same parameters as before, this approximation also yields the short and long trajectory pairs. This model enables the separation of the contributions from the two pairs, and it becomes apparent that indeed the opposite chirp of subsequent pulses seen in the previous section is a result from the contribution of the two trajectory sets (see Figure II.8). The spectrum from each trajectory set can also be calculated separately, showing that a continuum is generated in each half-cycle, and the frequency comb is, as expected, the result of interference from radiation produced in consequent half-cycles. As will be shown later, in experiments short and long trajectories can be spatially separated, and most practical uses favour the use of short trajectory radiation, making the saddle-point approximation a useful tool in single-atom calculations.

[8] According to Schwarz' theorem, as Φ is a continuous function of t and t' in the region concerning us, the differentiation order in mixed partial derivatives is exchangeable.

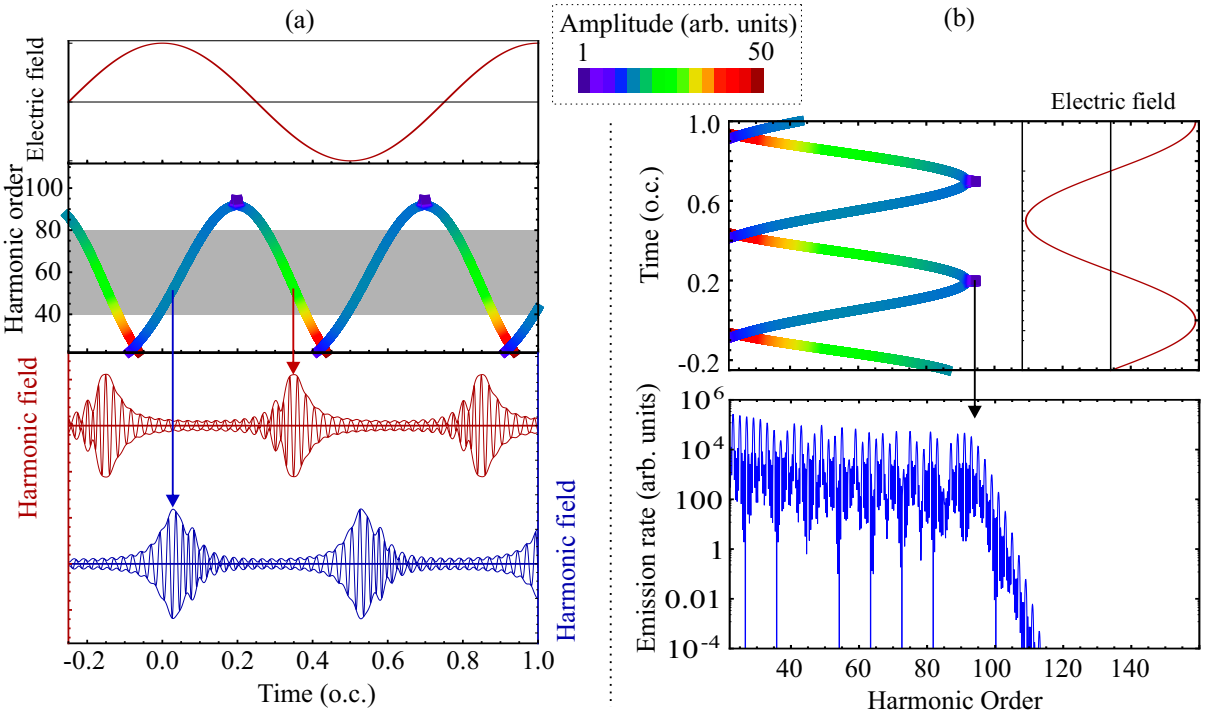

Figure II.8: *Returning electron trajectory parameters (time, energy, probability) and the generated harmonic radiation described in (a) time and (b) frequency domain, calculated from the solutions of the saddle-point approximation.*

Comparison of the models

The three different levels of approximation presented before give different levels of understanding of the process, but analysing them make clear that they contain the same physics at different levels of accuracy. A comparison of emission times calculated from the

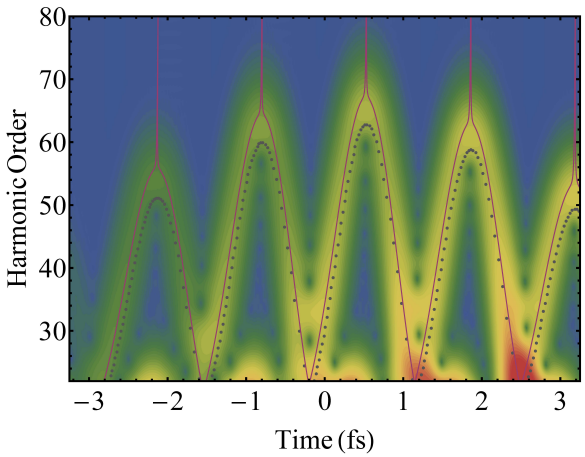

Figure II.9: *Density plot of time-frequency analysis of the dipole moment calculated by the Lewenstein integral, its saddle-point approximation (continuous line), and from the classical model (grey dots). For all three calculations an 800 nm,* 4×10^{14} *W/cm*^{2}*, 8 fs long laser pulse has been used.*

time-frequency map of the dipole radiation from the Lewenstein integral, the frequency-dependent electron return times of the classical model and the same quantities from the saddle-point equations shows a remarkably good agreement (see Figure II.9). The saddle-

point method can also be used to determine the exact position of the cutoff, which is at $1.32I_p + 3.17U_p$ in the high-intensity limit [42]. There are, however, inaccuracies in all of the above mentioned models, which are briefly discussed in the following subsection.

Accuracy of the Lewenstein model

In case of low-order harmonics (below I_p) the presented models are obviously not accurate, as those harmonics can be emitted by electrons remaining bound to the core, which is not described well by the approximations.

For higher harmonics, although not quantitatively accurate, the Lewenstein integral gives a good approximation of the HHG spectrum amplitude, especially for monatomic gases. The lack of quantitative agreement is partly due to the problem that the approximations used in the derivation make the application of the Ehrenfest theorem – which states that the wavepacket acceleration can be calculated as the second time-derivative of the wavepacket centre of mass position – inappropriate [53], especially for molecules [54]. For some atomic gases an improved description of the rescattering part enhances accuracy, especially around Cooper minima – apparent around 40 eV in Argon for example [55, 56]. The main problem here is the Volkov state approximation of the continuum electron wavefunction at the rescattering process, which can be corrected by improved cross-section calculations [57, 58].

Considering the phase of the produced harmonics, the agreement is a lot better, giving very good quantitative results when compared to the solution of the Schroedinger equation, especially for the phase derivatives [59, 60], with only minor misbehaviour shown to be present in case of two-centre molecules with vibrational motions [60]. The phase derivatives from the saddle-point approximation have also been shown to give excellent quantitative agreement with measurement data [61, 15, 62].

II.3.4 Phase of the generated high-order harmonics

As argued earlier, the spectral phase of a radiation also defines the temporal characteristics of the resulting pulse. The initial phase of harmonic q is given by $\varphi_q = arg\,[x(\omega_q)]$. A scrutinous examination of Equation II.14 reveals that the harmonic phase arising from a single trajectory is defined by $\frac{1}{\hbar}S_s(p_s, t'_s, t_s) + \omega_q t_s$, and also by a phase-factor arising from the rest of the integral. The latter can be discarded as it adds a very small contribution, therefore only the phase arising from $\frac{1}{\hbar}S_s(p_s, t'_s, t_s) + \omega_q t_s$ is of importance.

The $\omega_q t_s$ part describes the phase resulting from the time moment the electron returns to the core and "emits" the photon. At a fixed laser intensity the S_s part remains constant for a given harmonic. However, the start and finish of electron trajectories shift together with the laser field, therefore this relation shows that the phase of harmonic q ($\varphi_q \equiv \varphi(\omega_q)$) is directly inherited from the phase of the laser pulse as $q\varphi_1$. The relation also shows that the group delay of the attosecond pulse ($d\varphi_q/d\omega$) shifts together with the phase-delay of the generating laser pulse, as expected from the three-step model. From this equation it

also becomes apparent that the harmonic radiation inherits the coherence properties of the generating laser radiation.

If the laser intensity is changed, however, the other part of the phase – which arises from the quasiclassical action denoted $\frac{1}{\hbar}S_s(p_s, t'_s, t_s)$ – is also changed. From Equation II.8 it is clear that this part of the harmonic phase describes the phase of the electron accumulated along its journey in the continuum $\frac{1}{\hbar}\int_{t'}^{t}\left(\frac{[p_s+A(t'')]^2}{2}\right)dt''$ as compared to its bound counterpart $\frac{1}{\hbar}\int_{t'}^{t}(I_p)\,dt''$. Due to this, the intensity-dependent part of the phase – from the quasiclassical action and intensity-dependent return time t_s – is also called the *atomic phase*[9]. It is apparent that it depends on the length of the trajectory, and also on the average kinetic energy during the electron's travel. For a given harmonic order, both of these change if the intensity of the laser is changed. The total phase of the harmonic q is thus the sum of the phase inherited from the laser field and the atomic phase

$$\varphi_q = q\varphi_1 + \varphi_{at}. \tag{II.16}$$

Fortunately, this intensity dependent (atomic) phase can be approximated well with a simple formula

$$\varphi_{at} = \frac{-\alpha U_p}{\hbar\omega_1}, \tag{II.17}$$

where α can be calculated from the quasi-classical or saddle-point approximation [63]. It can also be approximated with constant values for short, long and cutoff trajectories [64, 65], when precise calculations are not feasible. The saddle-point calculation gives the value of α as a function of trajectory length defined by the energy of the emitted photon (see Figure II.10).

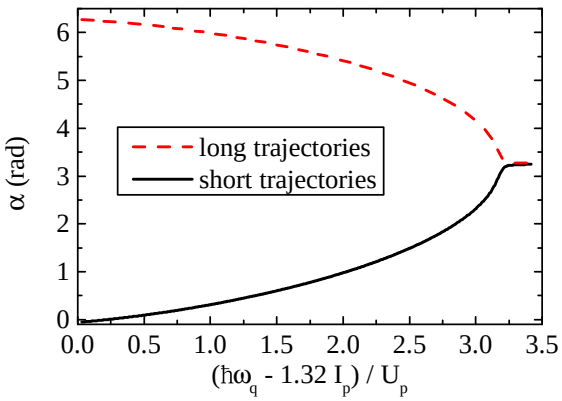

Figure II.10: *Coefficient of intensity dependent harmonic phase for different trajectories.*

The dependence of the atomic phase on the intensity has important consequences. If short laser-pulses are used, the phase of a harmonic generated at each half-cycle will be slightly different. This causes a shift of the frequency for which constructive interference

[9]The dipole oscillation emitting the harmonics can be understood as a result of the interference between the ground state electron wavepacket and the returning continuum wavepacket. The interference part depends on their phase difference, hence, it is oscillating exactly with $(E_{kin} + |I_p|)/\hbar$.

occurs in consecutive half-cycles, therefore in the rising and trailing edge of the pulse the generated harmonics are blue- and red-shifted with respect to odd harmonics of the fundamental radiation. A result of this is a broadening of the individual harmonic lines, which is more pronounced in case of long trajectories, because of their stronger intensity-dependent phase [43]. The broader spectrum of harmonics from long trajectories also means that their temporal coherence properties are worse [66], making radiation from short trajectories more suitable for most applications in attophysics.

II.4 Macroscopic processes in HHG

To accurately describe HHG in gases the entire macroscopic generation process has to be modelled. Because HHG is a highly nonlinear process, it is very sensitive to the shape and intensity of the laser field. A focused laser beam, however, has a spatial intensity distribution through the cross-section of the beam, and also different phase velocities on and off-axis around the focus. There are also propagation effects arising as the laser pulse propagates through the gas cell, like absorption and dispersion, and nonlinear interactions appear at high intensities, like self-focusing and plasma generation. These effects create different conditions for HHG in different parts of the gas cell.

Because HHG is a coherent process, perfect constructive interference from all radiating sources in the cell can cause the harmonic intensity to increase quadratically with the number of interacting particles, but destructive interference can eliminate the harmonic radiation altogether at the detection target. The phase difference between the atomic sources depends not only on the phase with which harmonics are generated, but also on their phase velocities in the generation medium. These processes altogether define the characteristics of the harmonic beam, and they can also significantly alter the intensity and structure of the attosecond pulses.

In this section details of the above-mentioned relations and processes are discussed and tools used to model HHG in macroscopic media based on the Lewenstein integral are presented.

II.4.1 General phase-matching considerations

Phase matching is a well-known phenomenon in nonlinear optics, and an important factor to deal with in second harmonic and sum frequency generation [30, 11]. It also plays an important role in high-order harmonic generation, but its source is different, and so are the possible ways to improve it. In this subsection general formulas and some quantities are introduced that are necessary to understand the concept of phase-matching and its role in HHG. Some of the discussed relationships are illustrated by one-dimensional examples, where the z axis is the common propagation axis of the laser and XUV radiation.

Phase matching, as its name suggests, describes how well the phases of harmonics generated at different parts of the cell matches each-other. To illustrate the importance

of phase-matching two radiating dipoles are singled out and studied along the z axis. One

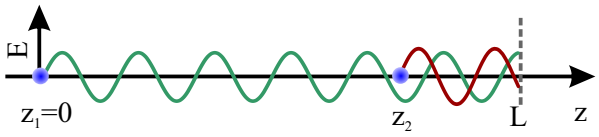

is placed at the origin $z_1 = 0$, radiating with an initial phase of $\varphi_q(z = 0)$, the other at an arbitrary distance z_2, radiating with initial phase $\varphi_q(z = z_2)$. The radiation produced by these sources interfere, and the resulting field is highest if the phase-difference at the detection point – for example at the end of the L long gas cell – is 0. This is the case of perfect phase-matching.

At any other phase-difference, the total field will be smaller, or even 0 when the two sources produce radiation with exactly opposite phase and the same amplitude. Therefore, to describe phase-matching the following has to be known: 1) the phase accumulated during the propagation of a harmonic from one part of the cell to the other (from z_1 to z_2), and 2) the differences in phase between harmonics generated at different parts of the cell (i.e. the $\varphi_q(z)$ function).

The first part of phase-matching (phase accumulated during propagation) depends on the properties of medium the harmonic propagates through, more precisely on the refractive index of the medium. Along a chosen direction it can be described by the wavevector $\boldsymbol{k}_q$, whose norm is given by

$$|\boldsymbol{k}_q| = \frac{n_q \omega_q}{c}, \tag{II.18}$$

where n_q denotes the refractive index for harmonic q.

The second part (phase of the generated harmonic) depends on the properties of the generating laser pulse in that particular point in the cell. Its evolution in the cell can be described by the gradient of φ_q, or in mathematical terms by

$$\boldsymbol{\kappa}_q = \nabla \varphi_q, \tag{II.19}$$

In the one-dimensional case the operator ∇ is replaced by the derivative $\nabla_z \equiv \partial/\partial z$. As shown in the previous section the phase of the generated harmonic ($\varphi_q(z)$) is related to the phase of the laser field, and to its intensity. Considering that the propagation of the laser field along z is described by the wavevector $\boldsymbol{k}_1 = \nabla \varphi_1$, the evolution of the generation phase of harmonic q can be described as

$$\varphi_q(z) = q\varphi_1(z) - \alpha \frac{U_p(z)}{\hbar \omega_1} = q k_1 z - \alpha \frac{U_p(z)}{\hbar \omega_1}, \tag{II.20}$$

where it was taken into account that the laser intensity, and therefore the ponderomotive energy may change along z. The first part of the right hand side describes the evolution of the laser's phase along the axis times the harmonic order, while the second part originates

from the intensity-dependent atomic phase discussed earlier. A wavevector $\boldsymbol{K}_q$ can also be assigned to the gradient of this atomic phase, and the following relation can be written

$$\boldsymbol{K}_q = -\alpha \nabla \frac{U_p(z)}{\hbar\omega_1} = -\alpha' \nabla I_1(z). \tag{II.21}$$

Here α' is derived from α, and includes all the constants so that the equation can be written in terms of laser intensity ($\alpha' = \frac{\alpha e^2}{2c\epsilon_0 m_e \hbar \omega_1^3}$). The wavevector describing the phase of the generated harmonics thus is given by the sum of q times the wavevector of the laser field plus the wavevector from the gradient of the atomic phase [64]

$$\boldsymbol{\kappa}_q = q\boldsymbol{k}_1 + \boldsymbol{K}_q. \tag{II.22}$$

Using the above-mentioned quantities, the condition for phase-matching can be described by a simple relation

$$\boldsymbol{k}_q = \boldsymbol{\kappa}_q, \tag{II.23}$$

meaning that for phase-matching to be achieved the wavevector of the qth harmonic in the medium should be matched with the wavevector of the qth component of the polarization [64].

This formulation of the phase-matching condition allows the definition of related quantities useful in the description and analysis of this phenomenon. The quantity defining the amount of phase-mismatch along a chosen direction is described by

$$\boldsymbol{\Delta k}_q = \boldsymbol{\kappa}_q - \boldsymbol{k}_q, \tag{II.24}$$

where $\boldsymbol{\Delta k}_q$ is called the wavevector mismatch.

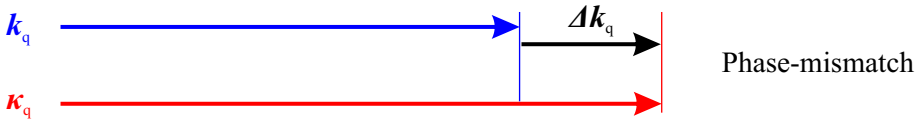

It should be mentioned that, in a real, three-dimensional description, the three wavevectors above does not have to be collinear. Thus, non-collinear phase-matching

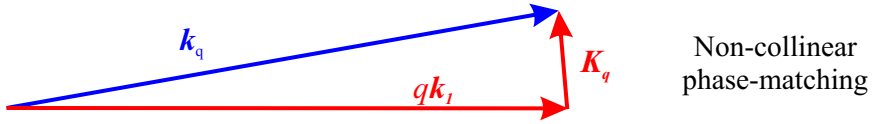

also becomes possible. This situation can arise when through the cross-section of the

laser beam the intensity is changing, creating a $\boldsymbol{K}_q$ that points outward from the centre of the beam [64]. The presence of such an outward-pointing $\boldsymbol{K}_q$ vector also causes the divergence of harmonic beam to increase, which is much more pronounced in case of long trajectories [29, 67]. The detailed discussion of this, however, is not the subject of this thesis.

II.4.2 One-dimensional description

To present the effects of phase-mismatch a one-dimensional case is considered and it is assumed that Δk is constant along the propagation axis. The harmonics generated at each point in the medium interfere with all the radiation generated before that point, hence, the harmonic field at any z point in a cell beginning at $z_0 = 0$ is given by integrating all the radiation up to z

$$\widetilde{H}_q(z) = \int_0^z h_q(z') e^{\imath[\varphi_q(z') + (z-z')k_q]} dz' = \int_0^z h_q(z') e^{\imath[\varphi_q(0) + zk_q + \Delta k_q z']} dz', \tag{II.25}$$

where $h_q(z)$ is the emission rate of harmonic q at any z point, and for the second equality the wavenumber mismatch is introduced.

To illustrate the evolution of harmonics along the axis, the zk_q part of Equation II.25 is discarded for the moment[10], and the emission rate is taken to be unity. The field along the z axis is then given by

$$\begin{aligned}\widetilde{H}_q(z) &= \int_0^z e^{\imath\Delta k z'} dz' = \frac{1}{\imath\Delta k}\left(e^{\imath\Delta k z} - 1\right) = \frac{e^{\imath\Delta k z/2}}{\Delta k} \cdot \frac{e^{\imath\Delta k z/2} - e^{-\imath\Delta k z/2}}{\imath} \\ &= 2\frac{sin\left(\frac{\Delta k z}{2}\right)}{\Delta k} e^{\imath\Delta k z/2} = z \cdot sinc\left(\frac{\Delta k z}{2}\right) e^{\imath\Delta k z/2}.\end{aligned} \tag{II.26}$$

The equation above shows that the field intensity is oscillating with a period

$$L_c = \frac{2\pi}{|\boldsymbol{\Delta k}_q|}, \tag{II.27}$$

where L_c is called the coherence length[11], an important and commonly used quantity in nonlinear optics[12]. It also shows that the phase of the propagated field $\phi_q(z) = arg[\widetilde{H}_q(z)]$ has exactly half the value of the generated field at the same point in the medium, or in other words: the harmonic phase at any z is the average of the phases generated before z [69]. Thus the phase difference between the propagated and generated fields $(\varphi_q(z) - \phi_q(z))$ is exactly half the value of the phase-difference between $\varphi_q(0)$ and $\varphi_q(z)$ (see Figure II.11.a). Due to this, the intensity of the radiation increases until $z = \pi/\Delta k$

[10] Later it will be shown that this is equivalent to describing the process in a different coordinate frame, and does not affect the results discussed here.

[11] It is a somewhat unfortunate name, because it has no direct relation to the coherence length of a radiating source. The latter is directly related to the coherence time which characterises the *temporal* coherence of a radiating source and is inversely proportional to the emission's bandwidth [68].

[12] Some textbooks use the definitions of $L_c = \pi/|\Delta k|$, that is half the length of L_c used here.

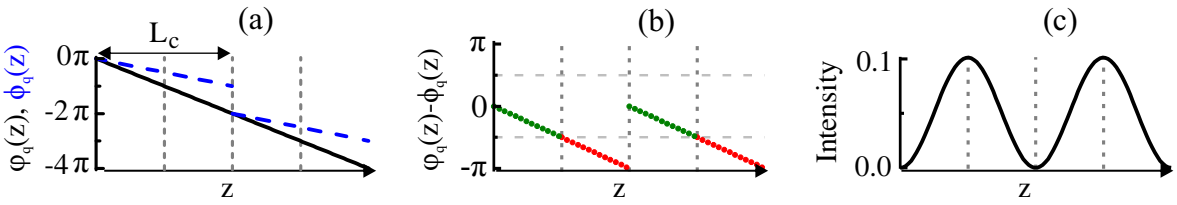

Figure II.11: *(a) Phase of the generated ($\varphi_q(z)$, black line) and that of the propagated ($\phi_q(z)$ blue dashed line) harmonic radiation along the propagation axis. (b) Phase difference ($\varphi_q - \phi_q$) between fields generated at and propagated until z, and (c) the normalized intensity of the field.*

is reached, i.e. when the phase difference between the harmonic generated at z and the radiation generated before z is $\pi/2$.

The right-hand side of Equation II.26 also shows that the intensity of the radiation at the exit of a one-dimensional L long cell is given by [30]:

$$I_q(L) = \frac{cn_q\epsilon_0}{2}\left|\widetilde{H}_q(L)\right|^2 \propto L^2 sinc^2\left(\frac{\Delta k_q L}{2}\right). \tag{II.28}$$

Thus, in case of perfect phase-matching $\Delta k = 0$ the harmonic intensity (and the generated number of photons) scales quadratically with the length of the cell ($I \propto L^2$). With a nonzero phase-mismatch on the other hand, a longer cell can reduce the intensity of the harmonic radiation.

By controlling the phase mismatch in a fixed-length medium, the intensity varies as in Figure II.12, a well-known feature in nonlinear optics, and it is responsible for the observation of the "Maker fringes" [70].

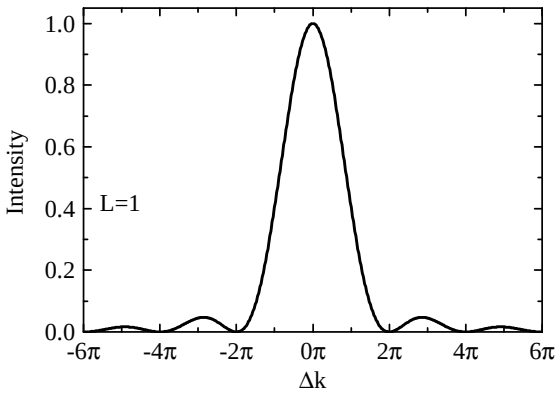

Figure II.12: *Intensity of the radiation in a fixed-length medium, as a function of the phase-mismatch.*

These relations above constitute the basis of phase-matching calculations. In the next section a more detailed view of phase-matching is presented through a one-dimensional model, where physical quantities are inserted in the equations, revealing general conditions for phase-matching.

II.4.3 Sources of phase-mismatch

To describe phase-matching the evolution of a harmonic signal is considered in one dimension, along the propagation axis of the laser field (z), in a medium that begins at the origin and has a length of L. In this frame only the projection to the z axis of all the above-mentioned wavevectors is important, and this can be described by simple wavenumbers.

Controlling the phase-mismatch is done by balancing the sources producing negative and positive wavevector mismatches. For this description it is convenient to use a frame of reference, moving with c in the propagation direction, thus transforming the coordinate system as $t' = t - z/c$ and $z' = z$. To illustrate the sources of phase-mismatch, the wavenumbers can also be illustrated within such a reference frame, thus their definitions become $k' = k - \omega/c$. In this frame a negative wavenumber is assigned to any wave with a phase-velocity higher than c ($n < 1$), and a positive to any wave with a phase-velocity smaller than c ($n > 1$). In the following part of this section this frame of reference and illustration method is used, but the prime symbol ($'$) in the notation is dropped for simplicity.

A) Neutral dispersion

Most commonly high-order harmonics are produced in noble gases, which have ionization energies between 12.1 eV (Xenon) and 24.5 eV (Helium). The plateau of a high-order harmonic spectrum begins at harmonics with photon energies higher than I_p, therefore these harmonics are above the absorption line in the respective gas[13]. Due to this, the refractive index is slightly smaller than 1 (the phase velocity of the harmonics is higher than c). The wavenumber of the propagating XUV field in the moving frame is $k_q = \omega_q(n-1)/c$.

The refractive index in this region can be measured experimentally, or calculated from the Kramers-Kronig relation[14] from experimentally measured absorption spectrum [19, 71, 72, 73]. Databases containing the values of *atomic scattering factors*[15] for different gases are freely available [74]. The refractive index is related to these scattering factors by the relation [19]:

$$n(\omega) = 1 - \frac{2\pi N_a r_e c^2}{\omega^2}[f_1^0(\omega) - \imath f_2^0(\omega)], \tag{II.29}$$

where N_a is the atomic density and $r_e = e^2/(4\pi\epsilon_0 m_e c^2)$ is the classical electron radius (here e denotes the elementary charge).

To exemplify the arguments refractive index data is presented for neon gas

[13] Absorption lines of inner-shell electrons are usually weaker and at much higher energies than the cutoff energy of the high-harmonic radiation, therefore these do not add a significant contribution to the refractive index in this region.

[14] The Kramers-Kronig relation connects the real and imaginary parts of a physical system's "response" to a "stimulus". It is applicable to linear, stable and casual systems, and it is widely used in optics for calculations of the part of the refractive index that is not directly accessible through measurements.

[15] These factors relate the scattering of a multi-electron atom to the scattering of a single, free electron.

($I_p = 21.56$ eV), at 1 bar pressure (see Figure II.13). As expected, the refractive index is

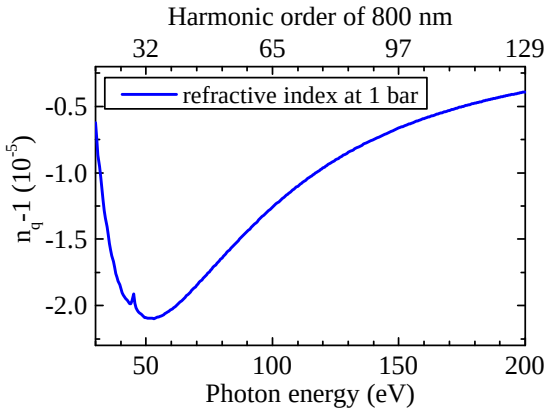

Figure II.13: *Refractive index in the XUV and lower part of the x-ray region of 273 K neon with 1 bar pressure. $n_q - 1$ scales linearly with pressure.*

smaller than 1, therefore it adds a negative contribution to the wavenumber k_q.

As seen above, the wavenumber κ_q depends on the phase-velocity of the laser field, and its intensity gradient. The frequency of IR lasers producing the harmonics, lays well below I_p and below all stronger resonance peaks in noble gases. As a result, in this region, normal dispersion is present, and the refractive index is higher than 1 (see Figure II.14). Refractive index in the IR region can be calculated from the Sellmeier equation using coefficients form experimental measurements [75].

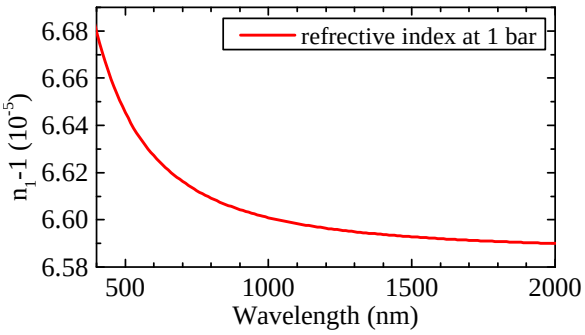

Figure II.14: *Refractive index in the visible and NIR region of 273 K neon gas with 1 bar pressure. $n_1 - 1$ scales linearly with pressure.*

Due to this difference in phase-velocities between the generating IR and the XUV field, phase-mismatch is naturally present during HHG. If the wavenumber of the generated polarization were to depend only on the refractive indices, the wavenumber of the polarization for harmonic 29 would be $\kappa_q = (n_1 - 1)29\omega_1/c$. At a pressure of 1 bar this would produce a coherence length of just 0.3 mm, limiting the useful length of a gas cell to just 150 µm.

B) Plasma dispersion

However, there are other contributions to the phase velocities, the most significant being the presence of free electrons, due to ionization. Free electrons contribute to the refrac-

tive index through their large negative polarizability. This adds a frequency-dependent susceptibility of

$$\chi_p = -\frac{N_e e^2}{\epsilon_0 m_e \omega^2}, \tag{II.30}$$

where N_e denotes the density of free electrons. Introducing the plasma frequency $\omega_p = \sqrt{N_e e^2/\epsilon_0 m_e}$ in the equation above, the plasma contribution to the refractive index can be written as

$$n_p(\omega) = \sqrt{1 - \frac{\omega_p^2}{\omega^2}} \approx 1 - \frac{\omega_p^2}{2\omega^2}. \tag{II.31}$$

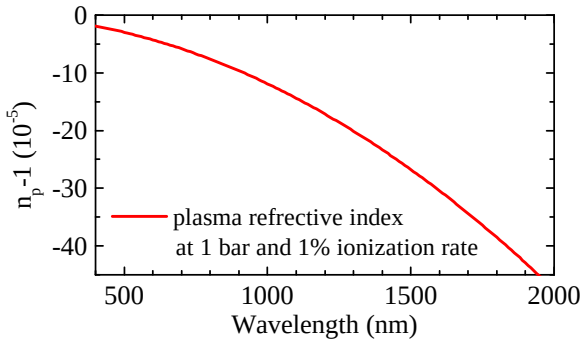

Figure II.15: *Plasma contribution to the refractive index in the visible and NIR region of 273 K neon gas with 1 bar pressure and at* 1% *ionization rate.*

This contribution (like neutral dispersion) scales linearly with the particle density, therefore, at a fixed ionization rate, the gas has a refractive index that also scales linearly with pressure. Because of the ω^{-2} scaling of the plasma refractive index, it quickly becomes negligible for high-order harmonics, and has to be taken into account only for the IR field. For 800 nm laser field the refractive index in neon becomes 1 at 0.8 % ionization rate (a method to calculate the ionization rate is discussed in Appendix A). At even higher ionization rates this contribution can balance the difference between IR and XUV refractive indices. For harmonics around 45 eV, at an ionization rate of 1.1 % the refractive indices of the laser and harmonic field are matched.

Focusing effects

In most laser systems beams are attempted to be as close as possible to a Gaussian beam (TEM_{00} transversal mode [76]). The electric field of a focused, Gaussian beam along the propagation axis is given as

$$\widetilde{E}(z,t) = E_1 \frac{w_0}{w(z)} exp\left[\imath\left(-\omega t + k_1 z + \varphi_G(z)\right)\right]. \tag{II.32}$$

Here φ_G is called the Gouy phase shift, and its value around the focus is given by

$$\varphi_G(z) = -\arctan(z/z_r), \tag{II.33}$$

where $z_r = \pi w_0^2/\lambda_1$ denotes the Rayleigh range, i.e. the distance from the focus where the radius of the beam $w(z)$ becomes $\sqrt{2}$ times larger than the beam waist w_0.

C) Gouy phase

From the equation above, it becomes apparent that around the focus of a laser beam the phase experiences a shift of π, increasing the phase-velocity of the focused laser field on axis, as compared to a plane-wave. It is apparent that the Gouy phase shift is quicker

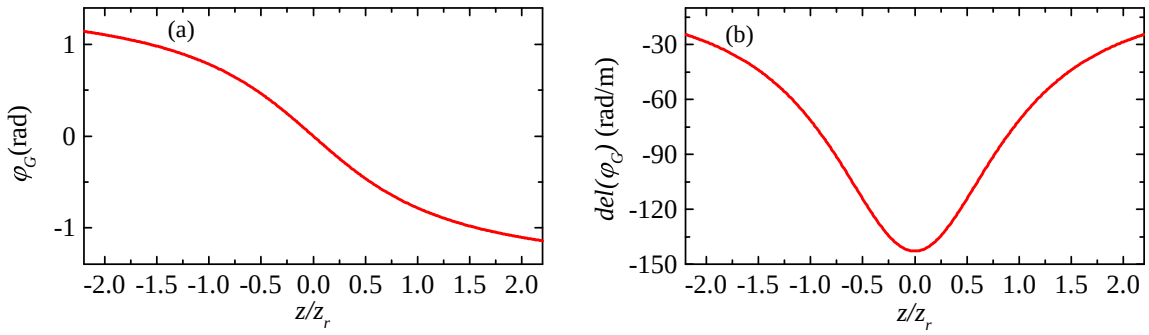

Figure II.16: *(a) Gouy phase (φ_G) around the focus of a Gaussian beam, and (b) its derivative ($\nabla_z \varphi_G$) calculated for 800 nm laser beam with $z_r = 7$ mm Rayleigh range.*

for tightly focused beams (when z_r is small). For example, using 800 nm laser source and focusing a $w = 3$ mm wide Gaussian beam with $f = 50$ cm optics produces a Rayleigh range of $z_r = 7$ mm and $w_0 = 42$ µm beam waist, and a phase-derivative as shown in Figure II.16.b.

D) Atomic phase

The last contribution to the wavenumber mismatch is the atomic phase. The intensity of a Gaussian beam around the focus is given by

$$I(z) = \frac{I(0)w^2(0)}{w^2(z)}, \tag{II.34}$$

where $I(0)$ is the peak intensity of the beam at the focal spot, and $w(z) = w(0)\,(1 + z^2/z_r^2)$ is the radius of the beam at z distance from the focal spot. Due to the variation of the driver intensity (see Figure II.17.a), the atomic phase is also changing, according to Equation II.21. This introduces a contribution which depends not only on the focusing geometry, but also on the peak intensity of the laser beam, and on the length of trajectory.

The value of the K vector varies from negative to positive while passing through the focal spot (Figure II.17). For short trajectories this contribution is small, and its positive value after the focus slightly increases the optimal ionization rate and thus the

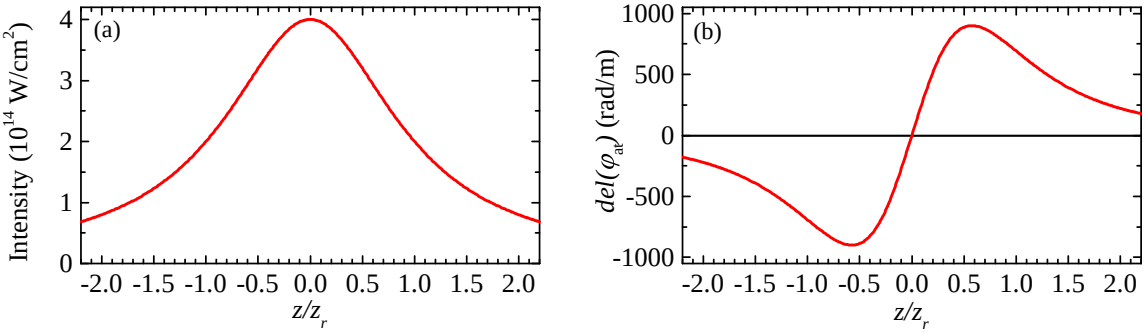

Figure II.17: *(a) Intensity variation of a Gaussian beam around the focus, along the propagation axis. (b) The derivative of the atomic phase for short trajectories (from the lower plateau region, where $\alpha \approx -2\pi/10$), in case of 800 nm driver field with 4×10^{14} W/cm^2 peak intensity. For long trajectories the magnitude of the K vector is ≈ 10 times larger.*

optimal laser intensity. As a result, placing the cell after the focus can yield more intense harmonics.

Long trajectories have an atomic phase about 10 times larger, which adds a very large positive contribution to K_q. This contribution also changes very quickly along the axis, and severely limits the length of the cell over which the phase-matching of long trajectories is achievable after the focus. However, for these trajectories non-collinear phase-matching is achievable before the focus [64]. In most phase-matching calculations, however, only short trajectories are taken into account, which have a weak intensity dependent phase, and this contribution sometimes is considered negligible [77].

Summary of phase-matching

As the efficiency of harmonic generation is quite low ($\approx 10^{-5}$ at 800 nm) and decreases further by using longer wavelengths ($\lambda^{-5.5}$ - $\lambda^{-6.5}$) [78, 79], efficient generation relies on involving as many coherent generation centres as possible. This can be achieved in a large interaction volume that requires good phase-matching conditions. In summary it can be said, that for phase-matching to be achieved several linear and nonlinear contributions to phase-mismatch have to be finely balanced, which depend on the type of gas, pressure, focusing geometry, cell position, length of trajectory and laser intensity. These sources define the phase-matching conditions in HHG, and methods to balance them are still researched today [77, 80, 41]. A summary of different contributions is presented in Figure II.18, where contributions to the XUV wavevector ($\boldsymbol{k}_q$) and polarization wavevector ($\boldsymbol{\kappa}_q$) are listed. For comparison, the values of these contributions are listed in Table II.1 for a specific focusing geometry and neon gas.

In the last two decades several phase-matching models have been developed for HHG, where some of the contributions were considered insignificant in a limiting case. For example taking into account the neutral and plasma dispersion is already a reasonable approximation to phase-matching conditions, when harmonics are generated by loosely

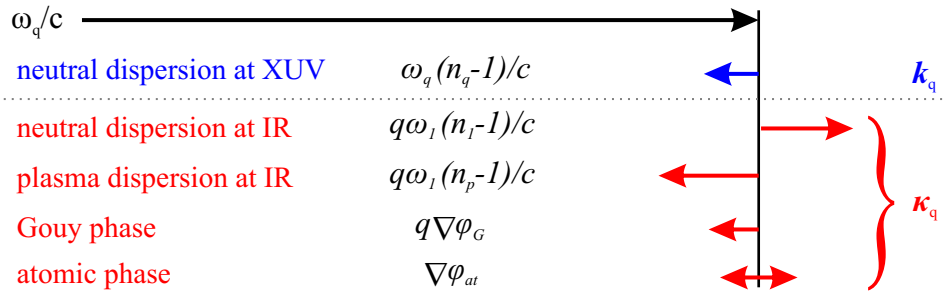

Figure II.18: *Summary of contributions to wavevectors of the propagating (blue) and generated (red) harmonics. Vector lengths are not to scale.*

$\Delta k(n_{XUV})/p$ (rad/m)/bar	$\Delta k(n_{IR})/p$ (rad/m)/bar	$\Delta k(n_p)/N_e$ (rad/m)/(bar×%$_{ion}$)	$q\nabla\varphi_G$ rad/m	$\nabla\varphi_{at}$ rad/m
−4370	15053	−17486	> -4140	$< \|900\|$

Table II.1: *Contributions to wavevector mismatch from different sources, calculated for harmonic 29 of a 800 nm laser field, focused to 42 μm spot into neon. Atomic phase approximated for short trajectories and at 4×10^{14} W/cm^2 peak laser intensity. Note: in equations II.30 and II.31 the electron density (N_e) is used in unit of m^{-3}, not in the very specific unit given in this table, which is used only to make the comparison easier.*

focused IR beams [41]. In this approximation the coherence length is maximised by balancing out the phase-mismatch from neutral dispersion with the plasma dispersion. This results an optimal ionization rate which is independent of pressure, as plotted in Figure II.19.a for the specific case of harmonics around 45 eV generated in neon gas.

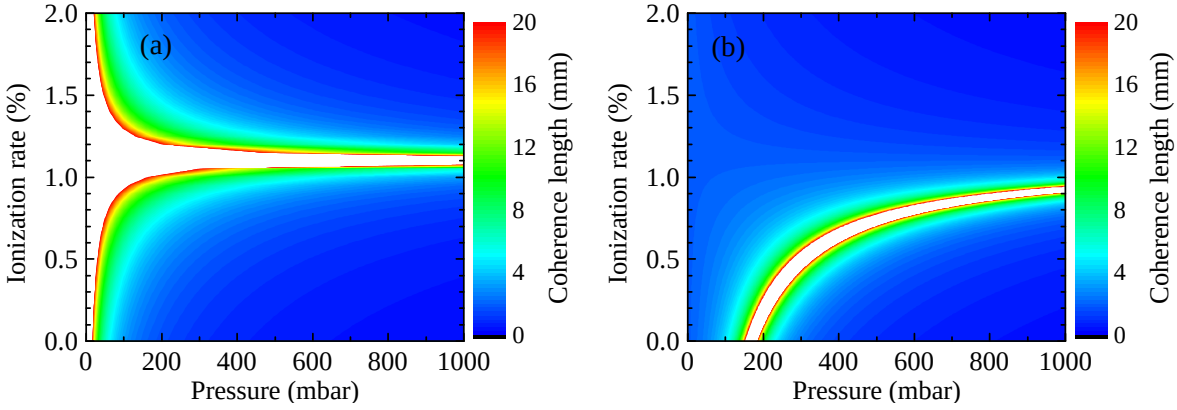

Figure II.19: *Coherence length in neon for 45 eV radiation produced by 800 nm laser field, as a function of pressure and ionization rate, calculated in (a) plane wave approximation, and (b) for a focused beam with $w_0 = 42$ μm beam waist.*

However, the presence of the Gouy phase shift adds a pressure-independent contribution to κ_q. In this case the balancing of refractive indices for the XUV and IR does not produce good phase-matching conditions. As a result, the coherence length is now defined by the ionization rate, pressure, focusing geometry and position of the cell relative to the focal position. Due to this, the optimal ionization rate and/or pressure becomes dependent on the generation geometry. For the focusing geometry discussed so far, the

coherence length in the focus evolves like in Figure II.19.b.

The generation geometry and ionization rate now also define the optimal pressure, which maximizes the coherence length [81, 82, 77]:

$$p_{match} = -\frac{\Delta k_G}{\frac{\partial(\Delta k_n)}{\partial p}}, \tag{II.35}$$

where Δk_n contains all the pressure-dependent contribution to the wavenumber mismatch (i.e. those contributions that depend on the refractive index).

Because the wavevector mismatch arising from the Gouy phase shift Δk_G is negative, the formula above also shows that phase-matching is not possible when the contributions from the refractive index is negative. This sets an upper limit to the ionization rate where phase-matching still can be achieved [83, 77]. This limit is called the *critical ionization rate*, and is defined by the neutral refractive indices at the IR and XUV. This critical ionization rate sets a limit to the highest laser intensity that can be used for HHG, and this also limits the achievable cutoff energy under conventional phase-matching [84, 83, 40, 41]. The critical ionization rate depends on the driver wavelength and gas type: for 800 nm driver field in neon it is around 1.1% and in argon around 4.8% (these values slightly depend on the harmonic order). Using three-cycle driver pulses for example, these values are achieved at laser intensities capable of producing high-order harmonics up to 70 eV in argon and 120 eV in neon [41].

II.4.4 The effects of absorption

The refractive index given by Equation II.29 is a complex quantity, but so far only its real part has been addressed. $n(\omega)$ can be split into a real and imaginary part like $n(\omega) = \delta(\omega) + \imath\beta(\omega)$[16]. In this description δ describes the evolution of the radiation's phase in the medium, while β the evolution of its amplitude. Radiation in a one-dimensional, linear medium propagates as (see equation II.18 and II.25)

$$\widetilde{E}(\omega, z) = \widetilde{E}(\omega, z = 0) \cdot exp\left[\imath\frac{n(\omega)\omega}{c}z\right]. \tag{II.36}$$

Inserting the complex refractive index into the equation above, yields an amplitude that is exponentially decreasing with the propagation distance as $exp(-\beta\frac{\omega}{c}z)$. Without an emission source, under absorption the intensity of the radiation decreases, and drops to $1/e$ of the initial value over the absorption length given by

$$L_{abs} = \frac{\lambda}{4\pi\beta}. \tag{II.37}$$

Under absorption the highest intensity of the generated radiation is limited and does not increase quadratically with cell length even if there is no phase-mismatch. As seen

[16] Different notations are used in the literature regarding the sign of β.

in Figure II.20 the absorption length in neon, especially for lower harmonics, can be very short at high pressures. If the absorption length is much smaller than the length of

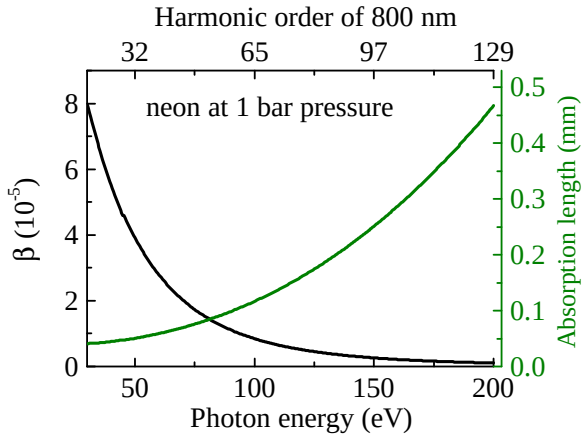

Figure II.20: *Attenuation coefficient (β, black line, left scale) and absorption length (L_{abs}, green line, right scale) of XUV radiation in neon at 1 bar pressure.*

the medium, only radiation generated around the end of the cell can leave the medium, therefore it is an important factor to consider in optimization of the generation parameters.

In an absorbing medium the intensity of the harmonics at the end of an L long cell assuming constant h_q emission rate is given by [85]

$$I_q(L) \propto h_q^2 \frac{4L_{abs}^2}{1+16\pi^2(L_{abs}/L_c)^2}\left[1+exp\left(-\frac{L}{L_{abs}}\right)-2cos\left(-\frac{2\pi L}{L_c}\right)exp\left(-\frac{L}{2L_{abs}}\right)\right]. \tag{II.38}$$

One effect of the absorption is that it washes out intensity oscillations at the coherence length and stabilizes the intensity even under phase-mismatch. Under perfect phase-matching the intensity saturates after a few L_{abs} [85], converging to the absorption limited intensity that is defined by the generation efficiency and absorption length.

Depending on the absorption length, the minimum values of the coherence length (L_c) and medium length (L_{med}) are defined by the equations [85]:

$$L_{med} > 3L_{abs}, \tag{II.39a}$$

$$L_c > 5L_{abs}. \tag{II.39b}$$

These ensure that the harmonic intensity at the end of the cell is at least half of the absorption limited intensity. For Figure II.20 it is apparent that absorption limits the achievable harmonic intensity at lower photon energies. At high photon energies on the other hand, phase-mismatch becomes the main limiting factor.

II.4.5 Quasi-phase matching in HHG

At photon energies where conventional phase-matching is hard to achieve, quasi-phase matching (QPM) schemes are often used to increase harmonic yield [41]. QPM is a

powerful tool when conventional phase matching is not possible, thus phase-mismatch (PMM) arises, resulting an oscillating harmonic intensity along the propagation axis (see Figure II.11). The zones where harmonic intensity increases/decreases are called zones of constructive/destructive interference. The basic idea of QPM is to eliminate harmonic emission in destructive zones, or switch these into constructive zones, thus increasing the harmonic yield over longer propagation distances.

As in gas HHG the traditional QPM schemes based on birefringence (achieved by periodic poling of the nonlinear crystal [86]) are not possible other methods have been proposed. These are based on some type of periodic modulation along the propagation axis, which includes atomic density, driving field intensity, or modulation caused by a secondary periodic field, which is either static [87], or propagating in another direction than the driving field [88, 65, 89, 90, 91, 5].

Periodic modulation of gas density is able to induce QPM in HHG with the possibility to select short and long trajectory components by changing the length of the modulation period, and even spectral selection can be achieved this way [92, 93, 94, 95]. The use of acoustic waves or multi-jet configuration target gas to obtain the required density modulation is also feasible theoretically [93, 94]. The principle of high photon flux soft x-ray generation in the QPM regime was already demonstrated experimentally using consecutive gas sources[17] [100]. The use of multi-jet systems employing two different gas types where harmonics are only generated in one type of gas from the two, the second only contributing to the phase-shift, was also demonstrated recently [101, 102].

Periodic modulation of the driver field intensity to induce QPM is also feasible in waveguides [103, 104], and has been already demonstrated experimentally at extreme ultraviolet [105] and at soft x-ray photon energies [106]. Periodic refocusing of the beam in the hollow core fibre, and QPM by multimode beating in capillaries has also been demonstrated [107, 108, 109].

The periodic modulation of the generated harmonic's phase by a weak assisting field, which propagates in another direction than the driver is also able to induce QPM [110, 111]. In the following section these methods are briefly reviewed.

General description of quasi-phase-matching methods employing low-intensity assisting fields

To describe the QPM process it is convenient to use a coordinate frame moving with the phase velocity of the harmonic in question ($z' = z, t' = t - z/v_q$). PMM can be assumed to grow linearly over shorter distances for harmonics generated in a waveguide [84, 83], and in some case also for harmonics generated in gas cells, or jets [63], therefore, when shorter periods are discussed, Δk_q can be considered constant over z. The phase of the generated

[17] Enhancement of HHG by using two consecutive gas targets of different gas types was demonstrated earlier [96, 97], however the enhancement observed in this case was shown to be present because XUV pulses generated in the first gas replace the role of tunnelling ionization in the second target allowing the control of quantum trajectories [98, 99] and improving phase matching, not due to QPM.

harmonic field in the moving frame can be expressed as $\varphi_q(z) = -2\pi z/L_c$ where L_c is the coherence length (see Equation II.27). The generated harmonic field at any given z then can be described as $\widetilde{h}_q(z) \propto h_q(z)exp[\imath\varphi_q(z)]$, where $h_q(z)$ is the emission rate for harmonic q.

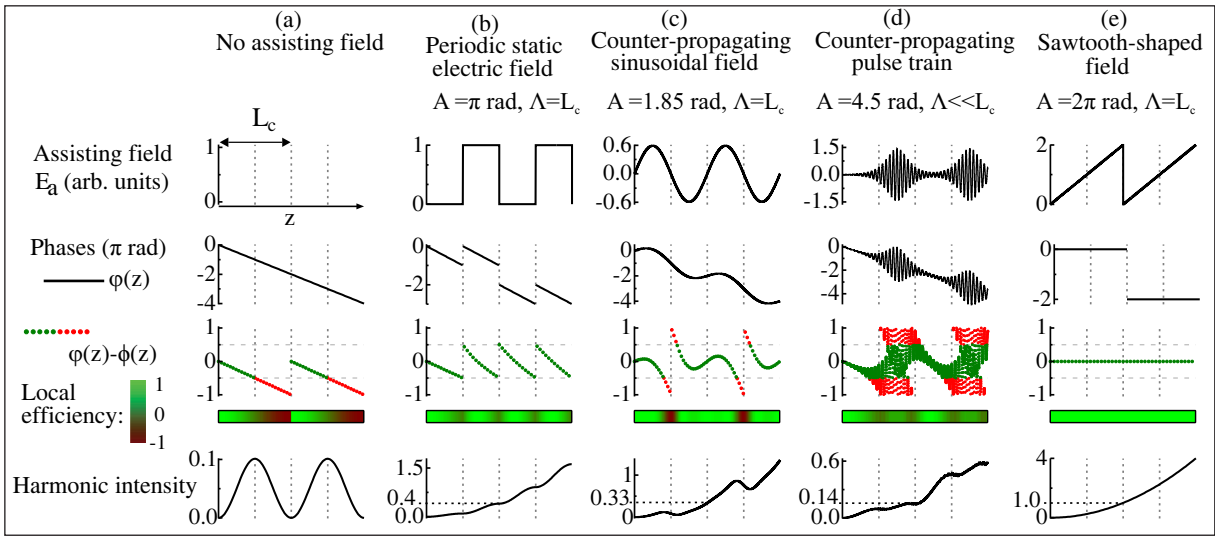

Figure II.21: *(a) Illustrating phase-mismatch in harmonic generation via phase and intensity variation along the propagation direction z. (b)-(e) Schematic presentation of QPM methods employing periodic assisting fields. Top row: illustration of the assisting field distribution. Second row: Effect of the assisting field on the generated harmonic's phase. Third row: Phase difference (modulo 2π) between the generated and propagated fields and local efficiencies shown in colour scale. Bottom row: Harmonic intensities, whose values at L_c also show the overall efficiency of the process. φ and ϕ denote phases of the generated and the propagated harmonic fields, as in Figure II.11.*

An assisting electric field periodic in space induces a periodic modulation of the polarization phase, so this becomes $\varphi_q(z) = -2\pi z/L_c + Af(z)$, where A is the amplitude of the phase-modulation induced by the assisting field and $f(z,t)$ is a normalized function with Λ spatial periodicity in the moving frame. QPM methods employing low-intensity assisting fields are based on the fact that the phase-shift induced by the assisting electric field scales linearly with its amplitude (E_a) in the limit when that is much weaker than the amplitude of the generating field ($E_a \ll E_1$, see [89] for details), and the shape of the phase-modulation resembles that of the assisting field. The phase-modulation amplitude can be expressed as

$$A = \zeta E_a, \tag{II.40}$$

where ζ is a scaling factor.

The efficiency of the phase-matching method can be defined as

$$\eta_q = I_q(L)/I_q^{PM}(L), \tag{II.41}$$

where $I_q^{PM}(L)] \propto |\widetilde{H}_q^{PM}(L)|^2 = \left|\int_0^L h_q(z)dz\right|^2$, i.e. it is the intensity of the propagated field produced with perfect phase-matching.

As seen in Figure II.21, in QPM the intensity of the generated harmonic increases approximately quadratically with the length of the cell as $\eta \cdot (L/L_c)^2$, with only slight sub-coherence-length oscillations around the parabola. The intensity in optimal QPM conditions might increase until it reaches the absorption limit. Whereas in the case of PMM, the peak intensity is reached at half of the coherence length, severely limiting the achievable photon number in macroscopic media.

Periodic assisting fields that can induce QPM can be of many types: to date periodic static electric fields, perpendicularly propagating THz fields, and counterpropagating (to the IR) quasi-cw laser and sawtooth-shaped fields and pulse trains have been proposed or used.

Periodic static electric fields

QPM in HHG by using periodic static electric field has been proposed by Biegert et al. [87, 112]. In this scheme high-order harmonics are periodically generated with no assisting field over half a coherence length, then, just before destructive interference would occur a DC field shifts the phase of the selected harmonic by $A = \pi$, and constructive interference continues over the other half of the coherence length (see Figure II.21.b). Alternating zones with and without static electric field create the condition for QPM. This scheme produces the same efficiency as conventional QPM $(2/(m\pi))^2$ in case of second-harmonic generation, which has been discussed extensively by Fejer et al. [113]. This also means that higher order spatial QPM is possible, where the periodicity is $m\Lambda$, m being a positive integer number. For odd m orders the length of 0 and π phase-shift zones should be $mL_c/2$, however for even orders $(m-1)L_c/2$ and $(m+1)L_c/2$ long zones should alternate [113]. It also follows that higher order QPM in the amplitude of phase-modulation $(n\pi)$ is possible, however only for odd n orders, and these produce the same efficiency as first order QPM. In conclusion, using this scheme 40.5% efficiency can be obtained by $A = \pi\ rad$ phase-shift with $\Lambda = L_c$ periodicity.

Sinusoidal electric fields matching the coherence length

QPM is also achievable with sinusoidal phase-modulation as illustrated in Figure II.21.c. Such schemes were proposed where the phase-modulation is achieved by counterpropagating quasi-cw fields [89, 114], or perpendicularly propagating THz pulses [5] . In both cases the optimal phase-shift induced by the assisting field has to be $A = 1.85$ radian (the position of the first extremum of the first order Bessel function of the first kind $J_1(A)$) [89]. Higher order QPMs can be achieved when the spatial period or amplitude of the phase-modulation is higher than required for first order. QPM of mth order in space and nth order in amplitude occurs when the phase-modulation period is mL_c and the amplitude is at the position of the nth maximum of $(J_m(A))^2$. The efficiencies in these cases can be calculated by the values of $(J_m(A))^2$, the highest being 33.7% for first order QPM [89].

Counterpropagating pulse trains

Another method of QPM is to scramble the phase of the generated harmonics at zones of destructive interference by a counterpropagating pulse or pulse train, that suppresses emission in these regions (see Figure II.21.d, [115, 116, 65]), and this can induce QPM [88]. The intensity of counterpropagating pulse interfering with the forward-propagating driving pulse has to be only a small fraction of the driving intensity to eliminate emission [65]. With this method the coherence length should match the width of the counterpropagating pulse, not its wavelength, therefore it is easiest to implement when the coherence length is much larger than the wavelength of the assisting pulse ($\lambda_a \ll L_c$) [90].

Complete elimination of emission in destructive zones can achieve an efficiency of 10.1% ($1/\pi^2$) with flat-top pulses [90]. Such laser pulses can be generated experimentally for this purpose [117]. However, destructive zones can also be switched into partially constructive zones, increasing efficiency [111, 90, 88]. In case of square-shaped pulses the best efficiency of 20% is produced by a phase-shift of $A = 3.83$ rad, this being the global minimum of $J_0(A)$ [90].

The phase-shift induced by the counterpropagating light yielding the best efficiency for $sech^2$-shaped pulses is $A = 4.5$ rad (case shown in Figure II.21.d), increasing the overall efficiency to 14% [90]. In this case the optimal length of the counterpropagating pulse is 0.23 L_c (intensity FWHM) [90].

The obvious advantage of this scheme is, that any phase-modulation comparable or larger than π would produce partial extinction of harmonic yield, therefore this method is not very sensitive to the parameters of the assisting field [65].

Sawtooth-shaped fields

In theory, perfect elimination of the PMM can be obtained, if a sawtooth-shaped field is applied as proposed in [118], see Figure II.21.e. Therefore, this in not a traditional QPM method, it is mentioned due to the fact that it also uses an assisting field and, in theory, this can achieve 100% efficiency.

Determination of assisting field parameters

The implementation of all QPM schemes which employ a secondary, periodic or quasi-periodic electric field requires a precise determination of the assisting field's parameters to achieve significant enhancement of the macroscopic radiation. The assisting field can be described by its period and amplitude.

The periodicity of the field is determined by the coherence length of the high order harmonic generation process by the fundamental field. As seen in the previous section, the calculation of the coherence length is feasible in waveguides or in very loose focusing geometries, where the intensity dependence of the polarization phase is not crucial [84].

In focused beams the calculation of the coherence length is difficult because the chang-

ing intensity along the propagation axis produces different ionization rates, thus the refractive index is also changing through the interaction region. Moreover, at high intensities, effects like self-focusing and plasma defocusing can occur [63]. Nonetheless, the measurement of the Maker fringes for different harmonics has been experimentally demonstrated to be possible by varying the length of the generation cell [119]. Lytle et al. have also found that two counterpropagating pulses can be used to measure the coherence length even in cases when the intensity of the driving field changes during propagation through the medium [91]. The measurement of the coherence length in a waveguide was also demonstrated by using one [120, 88], or two counterpropagating pulses [91]. In these conditions efficient QPM has already been demonstrated experimentally by counterpropagating pulses and pulse trains [88, 121].

Efficient QPM also requires the knowledge of the electric field amplitude which shifts the phase of the polarization by the required value, and this is discussed later in the thesis.

II.4.6 Three-dimensional description

The propagation of an electromagnetic wave through a nonlinear medium in general can be described by the wave equation [30]

$$\nabla^2 \boldsymbol{E} - \frac{1}{c^2}\frac{\partial^2 \boldsymbol{E}}{\partial t^2} = \frac{1}{\epsilon_0 c^2}\frac{\partial^2 \boldsymbol{P}}{\partial t^2}. \tag{II.42}$$

As seen earlier, at the intensities used for HHG, free electrons are also generated, hence the response of the medium ($\boldsymbol{P}$) calculated in the perturbative description is not accurate any more. However, because the high-order components of the nonlinear polarization are orders of magnitude weaker than the low-order components (perturbative response), the propagation of the laser field can be described independently of HHG. Therefore, the nonlinear response affecting the laser field can be calculated using the standard perturbative description but including the effect of plasma dispersion, while the generation of high-order harmonics and their propagation is described separately.

As a result, the three-dimensional description of HHG can be broken down to three distinct phases: 1) propagation of the driving field through the ionized medium, 2) generation of the harmonic field by single-atom sources and (3) propagation of the harmonic field through the medium.

Macroscopic description of HHG is easiest if radial symmetry of the laser and harmonic beam is assumed: the necessary dimensions are r and z in cylindrical coordinates, the time-dependence of the description completing the third dimension. As in case of the 1D model, a coordinate frame moving with c is used ($z' = z$ and $t' = t - z/c$), because this introduces further simplifications. Once again, the prime symbol is dropped from the notation for simplicity. The model described here is based on the paper by Priori et al [122], and further developed by Takahashi et al. [123], and Tosa et al. [124, 125]. The detailed description of the numerical model can be found in [124, 125]; here just a brief

summary of the important steps is provided.

Laser pulse propagation in ionized gases

The real electric field in a Gaussian beam, transmitting linearly polarized laser light, in cylindrical coordinates and in the moving frame can be described by the following equation

$$E(r,z,t) = E_1 \frac{w_0}{w(z)} exp\left(\frac{-r^2}{w^2(z)}\right) cos\left(k_1 z - \omega t + \frac{\pi r^2}{\lambda_1 R(z)} + \varphi_G\right) exp\left(\frac{-2ln(2)t^2}{\Delta T^2}\right), \tag{II.43}$$

where $R(z)$ denotes the radius of curvature, and is defined as

$$R(z) = z\left[1 + \left(\frac{z_r}{z}\right)^2\right]. \tag{II.44}$$

This equation defines the electric field at the entrance of the interaction region. From there on, the electric field can no longer be described by an analytical expression, due to the distortion effects, so it is numerically propagated: an (r,z) grid is defined over the interaction region, and on every grid point the laser field is calculated. The pulse evolution in an ionized gas can be described by the wave equation in following form [122]

$$\nabla_\perp^2 E(r,z,t) - \frac{2}{c}\frac{\partial^2 E(r,z,t)}{\partial z \partial t} = \frac{\omega_1^2}{c^2}(1 - n_{eff}^2)E(r,z,t), \tag{II.45}$$

where $\nabla_\perp \equiv \partial/\partial r$ denotes the radial derivative. Paraxial approximation is used[18], and $\partial^2 E/\partial z^2$ is neglected [122].

In the above formula the temporal derivative can be eliminated by a Fourier transform, yielding the equation

$$\nabla_\perp^2 \widetilde{E}(r,z,\omega) - \frac{2\imath\omega}{c}\frac{\partial \widetilde{E}(r,z,\omega)}{\partial z} = \widetilde{G}(r,z,\omega). \tag{II.46}$$

The spectrum of the laser pulse is calculated as

$$\widetilde{E}(r,z,\omega) = \hat{F}[E(r,z,t)], \tag{II.47}$$

the operator $\hat{F}$ denoting the Fourier transform acting on the temporal coordinate. The time-dependent response of the medium is also Fourier transformed to describe the source term

$$\widetilde{G}(r,z,\omega) = \hat{F}\left[\frac{\omega_1^2}{c^2}(1 - n_{eff}^2)E(r,z,t)\right]. \tag{II.48}$$

Small parts of this section might overlap with the author's previous work: "Modeling Generation of Water Window X-rays", Master's Thesis, Babes-Bolyai University, Cluj-Napoca, 2010.

[18]The paraxial approximation is valid for beam sizes much larger than the wavelength [76], which is generally satisfied in HHG because the laser wavelength is usually around 1 µm and the beam waist is seldom narrower than 40 µm.

The effective refractive index contains both the linear and nonlinear polarizability of the medium. The third-order susceptibility can also be included here in form of the nonlinear refractive index n_2. Because the nonlinear refractive index and ionization rate are time-dependent, the effective refractive index of the medium also becomes time-dependent, and can be written as

$$n_{eff}(r,z,t) = n_1(r,z,t) + n_2 I(r,z,t) - \frac{\omega_p^2(r,z,t)}{2\omega_1^2}. \tag{II.49}$$

Here $n_1 = \delta + i\beta$ is the linear term which accounts for the neutral dispersion (δ) and absorption (β). The calculation of n_2 is discussed in Appendix B.

Using this propagation equation $E(r, z_i, \omega)$ is calculated for the grid points z_i along the propagation direction by the Crank Nicolson method [126, 127, 128], (here $z_i = z_0 + idz,\ i = 1, 2, ...N$ and z_0 is the entrance of the interaction region). Having the values of $E(r, z_i, \omega)$ at a set of r coordinates, to obtain the values at z_{i+1} it is required to have an initial approximation for $E(r, z_{i+1}, \omega)$, which we get from the unperturbed beam, as defined in II.43. An important fact to mention is that due to the nonlinear source term in the right-hand side of the wave equation, at every step in z one integrates the propagation equation by using an iterative method until convergence is achieved and $E(r, z_{i+1}, \omega)$ is obtained. This also requires the calculation of the refractive index in each iteration step. At the boundaries ($r = 0$ and $r = R_{max}$) the following conditions are used:

$$\left.\frac{\partial E(r,z,\omega)}{\partial r}\right|_{r=0} = 0, \qquad E(r,z,\omega)|_{r=R_{max}} = 0. \tag{II.50}$$

Propagation of harmonic field

After the calculation of the propagated laser field, the nonlinear dipole moment $x(r, z, t)$ can be obtained from the Lewenstein integral on every grid point (see subsubsection II.3.3). This quantity is then used as a source term in the propagation equation of the harmonic field.

In this case the equation needed to be solved is

$$\nabla_\perp^2 \widetilde{H}(r,z,t) - \frac{2n}{c}\frac{\partial \widetilde{H}^2(r,z,t)}{\partial z \partial t} = \mu_0 \frac{\partial^2 P(r,z,t)}{\partial t^2}, \tag{II.51}$$

where $P(r, z, t) = [N_a - N_e(r, z, t)]x(r, z, t)$ is the nonlinear polarization calculated from the dipole moment of a single atom, and $N_a(z)$ is the initial atomic density. In this equation n is the refractive index which contains the neutral dispersion and absorption. The temporal derivative can be eliminated by a Fourier transform as before:

$$\nabla_\perp^2 \widetilde{H}(r,z,\omega_q) - \frac{2in\omega_q}{c}\frac{\partial \widetilde{H}(r,z,\omega_q)}{\partial z} = -\mu_0 \omega_q^2 \widetilde{P}(r,z,\omega_q), \tag{II.52}$$

where $\widetilde{H}(r, z, \omega_q) = \hat{F}[H(r, z, t)]$ and $\widetilde{P}(r, z, \omega_q) = \hat{F}[P(r, z, t)]$. These equations are also

solved, for each value of ω_q using the Crank-Nicholson method.

Near- and far-field spectra

At the exit of the interaction region ($z = L$) the spectral power density is given by

$$I(\omega) = 2\pi \int_0^{R_{max}} \frac{c\epsilon_0}{2} |H(r, L, \omega)|^2 r dr. \tag{II.53}$$

From the near field spectrum (at the exit of interaction region) the far field ($H(r_f, z_f, \omega)$) at a given z_f distance from the exit (now taken to be $z_0 = 0$ for simplicity) can be calculated by Huygens' integral defined for arbitrary ABCD ray-transfer matrices [76], which reads as

$$\widetilde{H}(r_f, z_f, \omega) = \frac{\imath\omega}{cB} exp\left[\imath\frac{\omega}{c}\left(z_f + \frac{Dr_f^2}{2B}\right)\right] \int_0^{R_m} \widetilde{H}(r, 0, \omega) exp\left(\imath\frac{\omega}{c} \cdot \frac{Ar^2}{2B}\right) J_0\left[\frac{\omega r_f r}{cB}\right] r dr. \tag{II.54}$$

Here J_0 is the zero-order Bessel function of the first kind, and the spectral power density at the far field from $\widetilde{H}(r, z, \omega)$ is calculable in the same way as for the near field. If only free-space propagation has to be calculated ($A = 1$, $D = 1$ and $B = z$) this equation reduces to the Hankel transform [129].

Using this transformation the harmonic field can be propagated to the circular aperture which cuts the components above a specified r radius, then the far field after focusing can also be calculated. Usually after passing through the aperture, the harmonic beam is focused into a detector where it is characterized or it is used to study attosecond processes. Although in a $2f$–$2f$ focusing geometry, if no aperture is put in the way, the far field at the detector reproduces the near field at the exit of the cell.

II.5 Experimental characterization of attosecond pulses

As electronic devices have a response time around the nanosecond region, characterization of ultrashort pulses require techniques to be invented. For this purpose many non-interferometric and some interferometric methods were developed working in the pico- and femtosecond regime [11, 130]. As these methods evolved, it became clear that general requirements can be set for the device that is able to characterize ultrashort pulses. These requirements were described in detail by Walmsley et al. [130], and they state that for a complete characterization of an ultrashort pulse with a time-integrating detector, at least one time-stationary and one time-non-stationary filter is needed, and the latter one must rely on a phenomenon that is comparably fast (or in some cases much faster) than the pulse to be characterized.

In most methods an auto- or cross-correlation of the pulse is recorded using a non-

linear process as a basis for the time non-stationary filter, and an algorithm is used to reconstruct the pulse from the recorded signal. As broadband XUV radiation is hard to manipulate due to the fact that most materials absorb in this region, autocorrelation methods, although already demonstrated [131, 132], are still far from being widespread in this field. They require a nonlinear detector, and so far two-photon ionization of Helium atoms has been demonstrated which has a limited bandwidth of applicability. The other limiting factor is the intensity of the attosecond pulses, but because this is also very important for XUV-pump XUV-probe experiments, its optimisation is in the focus of research [133, 134], and significant progress is expected in the near future.

To date, most attosecond pulse characterization techniques rely on cross-correlation of attosecond pulses with a replica of the generating IR pulse, that were the first methods demonstrated experimentally proving the existence of attosecond pulse(train)s [135, 136]. These two methods are the reconstruction of attosecond beating by interferometric two-photon transition (RABITT) and attosecond streaking. They are common in a sense that in both methods photoelectrons generated by the attosecond pulse in the presence of an IR field are recorded; however they are fundamentally different in the physical phenomenon applied. In RABITT a weak IR field is used and this method is able to characterize attosecond pulse trains, while in attosecond streaking a strong IR field is used, and the method is suitable to characterize isolated attosecond pulses. In the next subsection a short description of the RABITT technique is given, which is used later in this thesis to study macroscopic processes in attosecond pulse generation.

II.5.1 Reconstruction of attosecond beating by interferometric two-photon transition

This method makes use of one of the main characteristic of the harmonic spectra, that it contains only odd harmonics of the fundamental frequency. When interacting with an atom, these harmonics can be absorbed releasing a photoelectron wavepacket into the continuum with energy of $q\omega_1 - I_p$ (q being an odd number). If this process happens in the presence of a weak IR field, two-photon transitions can take place generating photoelectrons with energies corresponding to even harmonic orders (sidebands). These transitions can occur in two ways: the absorption of an XUV photon is followed by the absorption or emission of an IR photon. Although a process starting with the absorption of the IR photon is also possible, for most cases when RABITT is used this can be neglected [137], because in the commonly used target atoms there are no resonances for the IR (the IR field has to be weak), and the polarizability is low (for ex. in noble gases).

An experimental setup is presented in Figure II.22. The generated harmonic beam is filtered from low-order harmonics and from the fundamental IR beam by a thin (few hundred nm) metallic filter. The metallic foil also compresses the attosecond pulse by partially compensating for its GDD [29]. The harmonic beam is then recombined with the IR probe beam, and a toroidal mirror focuses them into a low-pressure gas jet at the

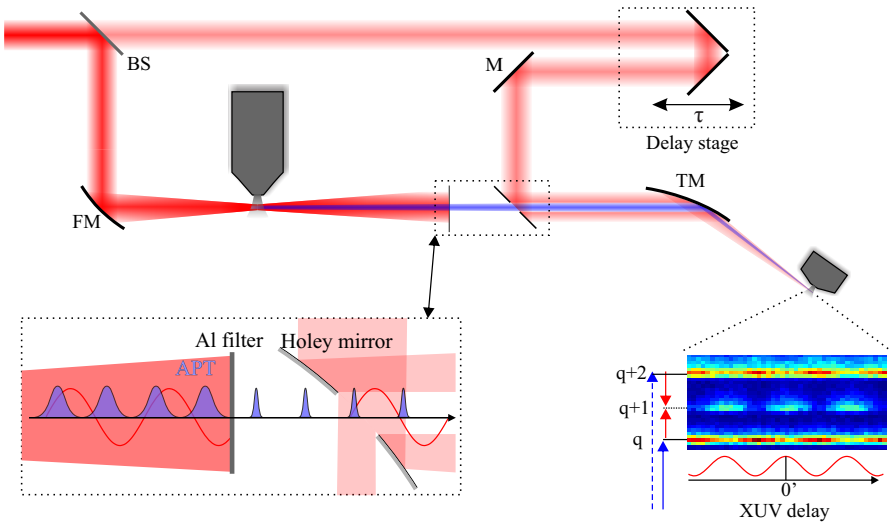

Figure II.22: *Scheme of an experimental RABITT measurement tool. The IR laser beam is split into a weak and a strong part by a beam splitter (BM). The strong beam is focused into a gas jet and generates high-order harmonics which pass through a metallic filter and a holey mirror before focused into a detector. The weak probe beam is combined with the harmonic beam at the curved holey mirror and is also focused into the detector. The time delay between the pump (XUV) and probe (IR) beams is controlled by the delay stage. The holey mirror serves as an aperture for the XUV and also matches phase-fronts of the IR probe and XUV beams.*

target area of an electron spectrometer. This spectrometer then measures photoelectrons released from the target atoms by ionization in this two-colour field. The electron spectrometer can distinguish electrons with different momenta by their time of flight from the target gas to the detector[19]. The time delay between the IR and XUV pulse is varied while continuously recording the photoelectron spectrum. The cross-correlation term appears in the oscillation of the sideband signal, which enables the reconstruction of the attosecond pulse.

To understand the principle mechanism of RABITT, two-photon transitions producing the sidebands are described below, following the approach used in [138]. The transitions produce a final state ($|f\rangle$) with energy $(q+1)\hbar\omega_1 - I_p$. The system starts in the ground state ($|g\rangle$ with energy $-I_p$, and $e^{\imath(I_p/\hbar)t}$ time-dependent phase), proceeds to a possible intermediate state ($|i\rangle$) by the absorption of an XUV photon ($q\omega_1$ or $(q+2)\omega_1$) and then to the final state ($|f\rangle$) by the absorption or emission of one IR photon. The two processes described above produce the same sideband and these can interfere, and the phases of different harmonics can be reconstructed from the cross-correlation measurement.

Following a textbook treatment of the process using second-order perturbation theory and single active electron approximation [139], the complex transition rates can be

[19]Many types of spectrometers can be used for detection. These include the simple time-of flight spectrometers (TOF), magnetic bottle electron spectrometers (MBES), velocity map imaging spectrometers (VMIS), reaction microscope (REMI, also measuring ions) and some other detectors with unique designs.

expressed as[20]:

$$A^{abs} = \sum_i \frac{\langle f| ex\widetilde{E}_1(t-\tau) |i\rangle \langle i| ex\widetilde{H}_q(t) |g\rangle e^{\imath(I_p/\hbar)t}}{\hbar(\epsilon_i - \epsilon_g - \hbar q\omega_1)},$$
$$A^{em} = \sum_i \frac{\langle f| ex\widetilde{E}_1^*(t-\tau) |i\rangle \langle i| ex\widetilde{H}_{q+2}(t) |g\rangle e^{\imath(I_p/\hbar)t}}{\hbar(\epsilon_i - \epsilon_g - \hbar(q+2)\omega_1)}, \tag{II.55}$$

where τ is the delay between the IR and XUV fields, ϵ_g, ϵ_i and ϵ_f denote the energies of the ground, intermediate and final states, and classical electric fields polarized in the x direction are assumed. These fields can be separated to a slowly varying envelope and an oscillating part:

$$\widetilde{E}_1(t) = Env_1(t)e^{-\imath(\omega_1 t+\phi_1)},$$
$$\widetilde{H}_q(t) = Env_q(t)e^{-\imath(q\omega_1 t+\phi_q)}. \tag{II.56}$$

In Equation II.55 it is reasonable to assume that the perturbing fields are uniform across the spatial extent of the electron wavepacket (do not depend on x), and the formulae can be simplified by separating the time-dependent parts affected by the electric fields and noting the rest as:

$$R_q^{abs}e^{-\imath\phi_q^{abs}} = \sum_i \frac{\langle f| ex |i\rangle \langle i| ex |g\rangle}{\hbar(\epsilon_i - \epsilon_g - \hbar q\omega_1)},$$
$$R_{q+2}^{em}e^{-\imath\phi_{q+2}^{em}} = \sum_i \frac{\langle f| ex |i\rangle \langle i| ex |g\rangle}{\hbar(\epsilon_i - \epsilon_g - \hbar(q+2)\omega_1)}. \tag{II.57}$$

Now choosing $\phi_1 = 0$ initial phase for the IR field the following stands

$$A^{abs} = R_q^{abs}e^{-\imath(\phi_q^{abs}+\phi_q-\omega_1\tau)}Env_1(t-\tau)Env_q(t)e^{-\imath[(q+1)\omega_1 - I_p/\hbar]t},$$
$$A^{em} = R_{q+2}^{em}e^{-\imath(\phi_{q+2}^{em}+\phi_{q+2}+\omega_1\tau)}Env_1(t-\tau)Env_{q+2}(t)e^{-\imath[(q+1)\omega_1 - I_p/\hbar]t}. \tag{II.58}$$

The signal recorded by the electron spectrometer can be calculated as:

$$S(\omega,\tau) \propto \left| \int_{-\infty}^{\infty} A^{abs} + A^{em} dt \right|^2. \tag{II.59}$$

The time-integration reduces the field envelopes and the $[(q+1)\omega_1 - I_p/\hbar]\,t$ oscillation to a spectral line, which – for simplicity – now is assumed to be the same for the two processes, and is noted by $f(\omega_{q+1})$. To get an easily interpretable result it is also assumed that the real numbers R_q^{abs} and R_{q+2}^{em} are equal. Doing the arithmetic for the rest of the

[20] In case of RABITT the possible intermediate states are in the continuum, therefore the summation over i turns into an integral over continuum states with different energies. This also means that the integrand always has a singularity, but methods to solve this problem have been described by Toma et al. [137].

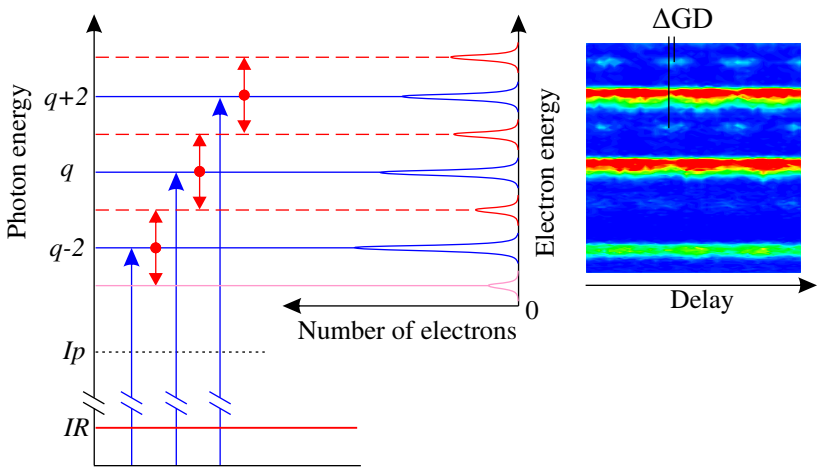

Figure II.23: *Electrons ionized by two-photon transitions yield sidebands which oscillate as a function of the delay between the IR and XUV field. Right-hand side of the figure shows an experimentally recorded photoelectron spectrum. The phase of sideband oscillations is directly related to the GD of pulses synthesized from the two neighbouring harmonics.*

equation the final result for the sideband signal is obtained

$$S(\omega,\tau) \propto 2f(\omega_{q+1})\left[1+cos(\phi^{em}_{q+2}-\phi^{abs}_{q}+\phi_{q+2}-\phi_q+2\omega_1\tau)\right]. \tag{II.60}$$

This shows that the sideband signal will oscillate as $2\omega_1\tau$ and the phase of the oscillation depends on the phase difference between neighbouring harmonics $\Delta\phi_{q+1}=\phi_{q+2}-\phi_q$ (see Figure II.23). This can also be understood as the GD of an XUV pulse synthesized only from these two harmonics ($\tau_{q+1}\equiv GD_{q+1}=\Delta\phi_{q+1}/(2\omega_1)$), therefore by recording different sideband signals simultaneously, one can measure the GD of neighbouring harmonic pairs. Their absolute value, however, would only be measurable if the absolute value of τ was known. This is usually not the case, therefore one cannot extract the exact GDs just their variation over the spectrum, which allows the determination of higher order phase derivatives (GDD, TOD and so on).

An example of a RABITT trace is shown in Figure II.24. The values of $\Delta\phi_{q+1}$ can be calculated by finding the phase of the oscillations using cosine fitting or the Fourier-transform method. The relative harmonic phase is an integral of the retrieved GD and can be calculated as the sum of these phase differences, assuming a zero value for the lowest order sideband for example. For the reconstruction of the attosecond pulse now only the spectral amplitudes of the harmonics are needed, which can be extracted from the recorded XUV-only photoelectron spectrum (i.e. spectrum recorded by blocking the probe beam), corrected with the transition probabilities.

Some of the assumptions made to derive the results are discussed below. First of all, the validity of the assumptions made about the spectral line ($f(\omega_{q+1})$) and transition rates (R^{abs}_q and R^{em}_{q+2}) being equal does not change the drawn conclusions as those only affect the contrast of the oscillation, but not its phase i.e. in Equation II.60 $1+cos(...)$ becomes $C_1+C_2cos(...)$. As apparent from Equation II.60 the sideband phase also depends on

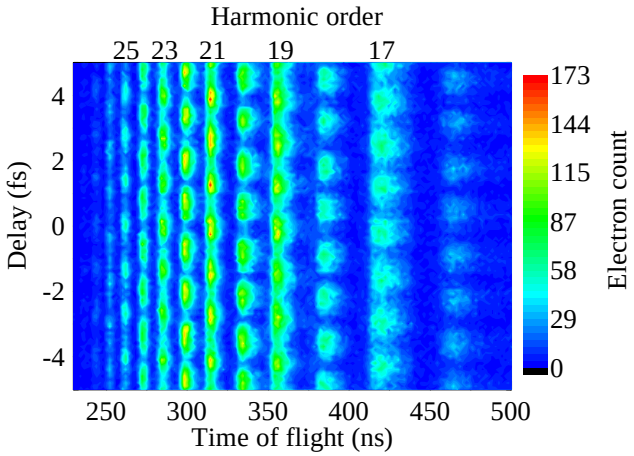

Figure II.24: *Experimentally recorded photoelectron spectrum. Harmonics were generated in argon by 800 nm, 35 fs laser pulses at 1 kHz repetition rate. The delay was varied in 100 as steps, and the spectrum was summed for 1000 shots in each delay step. Argon was also used for the detection in the magnetic bottle electron spectrometer which can distinguish electron energies by their time of flight from the target gas to the micro-channel plate.*

the phase difference arising from the electron transitions $\Delta\phi^{at}_{q+1} = \phi^{em}_{q+2} - \phi^{abs}_{q}$, which is also called atomic delay ($\tau^{at}_{q+1} = \Delta\phi^{at}_{q+1}/(2\omega_1)$). When the technique is used for pulse characterization noble gases are used as target where the atomic delays are small and do not affect the shape of the reconstructed pulse significantly, but still, for an accurate reconstruction they have to be taken into account [135].

RABITT is also used to study the photo-ionization of the target gas for examples by measuring the above-mentioned atomic delays. These have two components: one is caused by the energy dependence of the scattering phase [140], also called Wigner delay, and the other is the result of phase-shifts arising during continuum-continuum transitions [141]. It should be noted that the Wigner delay can be very high when resonant transitions are involved [140, 142], however, using noble gases as target, in most cases the harmonics are far away from any resonance, and it becomes very small. Although, almost negligible from the point of view of pulse reconstruction, these delays encompass interesting physics and their measurement is very much in the focus of attosecond science [143, 141, 144, 51, 9].

It should be also mentioned that the method described here allows the reconstruction of an "average" pulse in the pulse train, and its accuracy depends on how much the individual pulses vary in the train. The length of the generating pulse strongly influences this variation, and pulse trains generated by few-cycle laser pulses need more advanced methods for accurate characterization [145, 146]. The principles of RABITT were also used in trying to characterise pulse trains with both even and odd harmonics, relying on the fact that due to dipole selection rules, electrons produced by one- and two-photon transitions have different angular momenta, allowing their separation in the measurement using a velocity map imaging spectrometer [147, 148].

III Results

As XUV radiation and attosecond pulses are used to study electron dynamics with the highest possible spatial and/or temporal resolution, the main goals of research in this area are to produce even shorter light pulses [149, 150], to realize XUV pump XUV probe experiments [133], and to extend the applicability of these sources by increasing the maximum photon energy [41, 151], photon flux [80] and repetition rate [82, 152, 27] of the generated harmonics.

In this chapter my contribution to research in the field of HOH and attosecond pulse generation is reviewed. The results to be presented here focus on the possibilities to increase the HHG cutoff, isolate single attosecond pulses from a pulse train while also minimizing its duration, increase harmonic yield at high photon energies, and in general to understand macroscopic processes in HHG. These are based on our theoretical papers about THz assisted attosecond pulse generation [2, 3, 4], quasi-phase matching of HOH radiation and its study for the special case of perpendicularly propagating IR and THz fields [5, 6, 7], optimization of attosecond pulse generation in light-field synthesizers [10], and an experimental study of attosecond GD dependence on generation gas pressure [8].

III.1 High-order harmonic generation in the presence of long wavelength fields

The most widespread laser for HHG uses Titanium doped Sapphire crystal as gain material, which produces a central wavelength of ≈800 nm. As we have seen earlier the highest usable laser intensity in HHG is limited by ionization, and there exist laser sources which produce a lot more energy than what is usable for HHG. The excess laser pulse energy can be used to generated ultrashort pulses at different wavelengths using, for example parametric processes in nonlinear crystals. Mixing these pulses with the original 800 nm laser pulse and carefully tuning the parameters of the individual pulses can create an advantageous environment for generation of high photon energies and isolated attosecond pulses [153, 154]. Using difference frequency generation (DFG), very strong (up to 100 MV/cm) THz fields have been demonstrated [155]. The mixing of these fields with 800 nm laser pulses, therefore promised interesting features in HHG.

Many studies have been carried out on the effect of long wavelength (compared to the laser field generating HOH) or DC fields on high-order harmonic generation, and at single atom level this process has been analysed thoroughly using classical [156] and semi-classical models [157], using zero range potential calculations [158], strong-field approximation [159, 160] and by solving the time dependent Schrödinger equation for a

model atom [156, 161, 162, 163, 164].

It has been revealed that the addition of a DC or THz field to the generating laser pulse breaks the half-cycle symmetry of the HHG process, and leads to the appearance of both odd and even harmonics in the spectrum [158, 156, 161]. The presence of a relatively low-intensity, low frequency field can extend the cutoff [159, 160], while a double-plateau structure appears in the spectrum, and it can prevent the closing of some trajectories which favours the generation of a broad supercontinuum and the selection of a single attosecond pulse in cases when the generating laser pulse is short enough [162, 164]. As reported in [162], the origin of this supercontinuum is radiation from recombining electrons passing through short trajectories, the THz field suppressing the emission from the corresponding long ones. It is also observed that with a strong negative chirp of the laser pulse, the width of this supercontinuum may be further increased to obtain a flat spectrum as wide as 700 harmonic orders [162]. However, laser pulses and DC fields used by Xiang et al. [162] are not yet available, hence we focused our study on longer laser pulses without chirp and THz pulses instead of DC fields.

100 MV/cm peak electric field of THz pulses is already comparable with that of the laser pulse's used in gas HHG (usually between 300 and 1000 MV/cm), therefore it can considerably alter this highly nonlinear process. In our work we study the effects of these, experimentally demonstrated fields on the process of HHG using the easily interpretable saddle-point approximation and we verify the predictions in a macroscopic model as well.

III.1.1 Single-atom calculations

HHG by quasi-monochromatic laser field and a static electric field

To understand the process, first, we study electron trajectories in one optical cycle of the generating, quasi-monochromatic 800 nm laser field, in the presence of a DC field, and later we move to THz fields and few-cycle laser pulse.

The most obvious effect of the field is breaking the usual periodicity of the process, as consequent half-cycles now have different properties. In one half-cycle we observe trajectories corresponding to weaker dipole strengths and ending in a higher cutoff (1), in the other half-cycle the trajectories meet at a lower cutoff but the corresponding dipole strengths are stronger (2). In earlier studies the difference in dipole strengths has been attributed to diffusion effects [159, 160], which certainly play a role, as the trajectory sets with higher cutoff energy (1) spend a longer time in the continuum than they would in the absence of an assisting field (0.65 optical cycles in case of cutoff trajectories [165]). And the opposite is true for those trajectory sets which have a lower cutoff (2), as can be seen in Figure III.1.

However, our model also shows that the direct relationship between ionization probability and the instantaneous electric field strength at the time of ionization plays an important role too. In laser-only, quasi-monochromatic case, the ionization step of cutoff

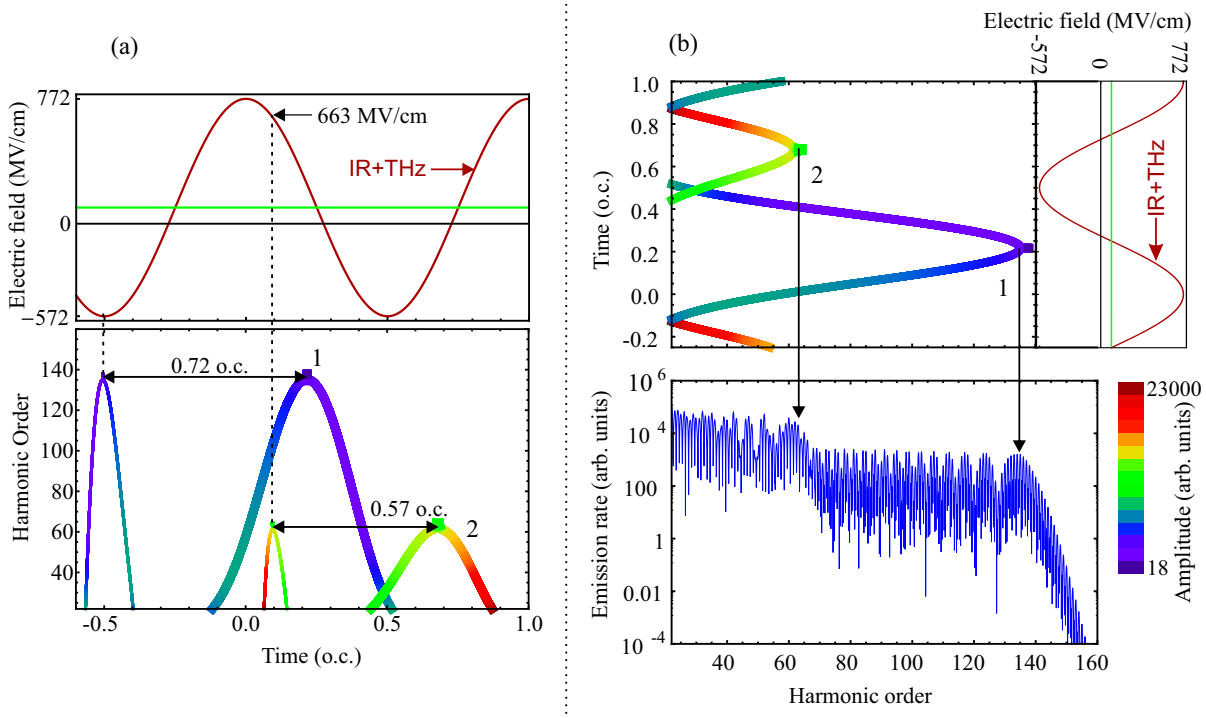

Figure III.1: *Electron trajectories and high harmonic spectrum generated in the presence of the THz field. THz field strength is 100 MV/cm indicated in green, the $6{\times}10^{14}$ W/cm^2 laser intensity corresponds to 672 MV/cm. In (a) ionization (thin lines) and recombination (thick lines) times of electron trajectories from a single optical cycle (o.c.) are presented to show the generation of the alternating properties of the produced radiation as a result of the broken symmetry in consequent half-cycles induced by the DC field. (b) The two cutoffs with different emission rates produce the double-plateau structure of the spectrum.*

trajectories takes place ≈0.05 T after the peak of the pulse [165, 166]. In the presence of the assisting field this step occurs earlier and electrons that leave before the peak return to the ion in half-cycle (1). At appropriate ratios of the laser and DC field, electrons performing a short trajectory are ionized around the peak of the field, while long trajectories are ionized earlier. As a result, in this half-cycle the dipole strength of short trajectories is stronger than that of the long ones. In cases with extremely high assisting field strengths the closing of long trajectories can even be prevented [164].

Figure III.1 shows that electron trajectories noted with (1) start at a weaker field strength (≈570 MV/cm) where the ionization probability is lower, hence the lower emission rate. However the strong field present in the next half-cycle allows them to gain more kinetic energy before recombination, producing a higher cutoff. Electrons released in the next half-cycle (2) start at much higher field strengths (≈660 MV/cm), but the cutoff is reduced as the THz field prevents them gaining kinetic energy. These field strengths are not necessarily higher than in laser-only case, however diffusion effects are less pronounced due to the shorter trajectories, resulting in slightly higher emission rates.

For a multicycle pulse this process is repeated in every optical cycle, therefore a time resolved spectrometer should see a half-cycle variation of the spectrum: strong with narrower and weak with broader bandwidth. Using a time-integrating spectrometer a double-

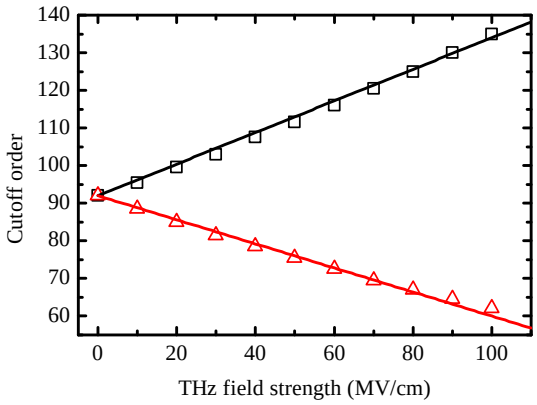

Figure III.2: *Variation of the higher (black squares) and lower (red triangles) cutoffs with THz field strength. Higher cutoffs are generated when the THz field, having the same sign as the IR, is increasing the kinetic energy of the recombining electrons.*

plateau spectrum is recorded, where the two cutoffs are almost symmetric of the THz-free cutoff (Figure III.2). The position of these varies almost linearly with the applied field strength, but the contrast between the dipole strengths also increases as reported by Wang et al. [159], limiting the applicability of very strong fields. In our case the higher cutoff is extended by ≈0.43 harmonic order (≈0.66 eV), and the lower one decreases with ≈0.32 harmonic order (≈0.5 eV) for each MV/cm of the assisting field, but these numbers vary with the wavelength and intensity of the laser field.

If attosecond pulses are synthesized from the lower plateau, a harmonic pulse is produced every half-cycle with alternating amplitude, whereas from the higher plateau only one pulse per cycle is obtained. A consequence of the full-cycle periodicity produced by this symmetry-breaking is the appearance of even harmonics in the spectrum [158].

Effect of a THz pulse on HOHs generated by few-cycle laser pulses

As each half-cycle where the cutoff is extended is surrounded by two half-cycles, where the cutoff is decreased, it is well funded to assume that the combination of THz fields with few-cycle laser pulses is able to significantly increase the available spectral width for SAP generation. To this end we use 10 µm wavelength fields (30 THz), as these high fields were experimentally demonstrated around this region [155].

For a 5.2 fs laser pulse the trajectories are modified such that the highest harmonics are produced only in a single half-cycle, and a very broad continuum appears in the spectrum (see Figure III.3). Wider spectral widths can support shorter pulses. In HHG, however, the shortest attosecond pulse is not necessarily generated from the widest available spectrum due to the inherent GDD of harmonics. Due to this intrinsic chirp (see Figure III.3), transform limited pulses are only achievable using post-compression methods, or when using only cutoff harmonics for synthesis [29, 167, 168].

As experimentally long trajectories are eliminated either by phase-matching or by irising the harmonic beam, we use only short and cutoff trajectory radiation when synthe-

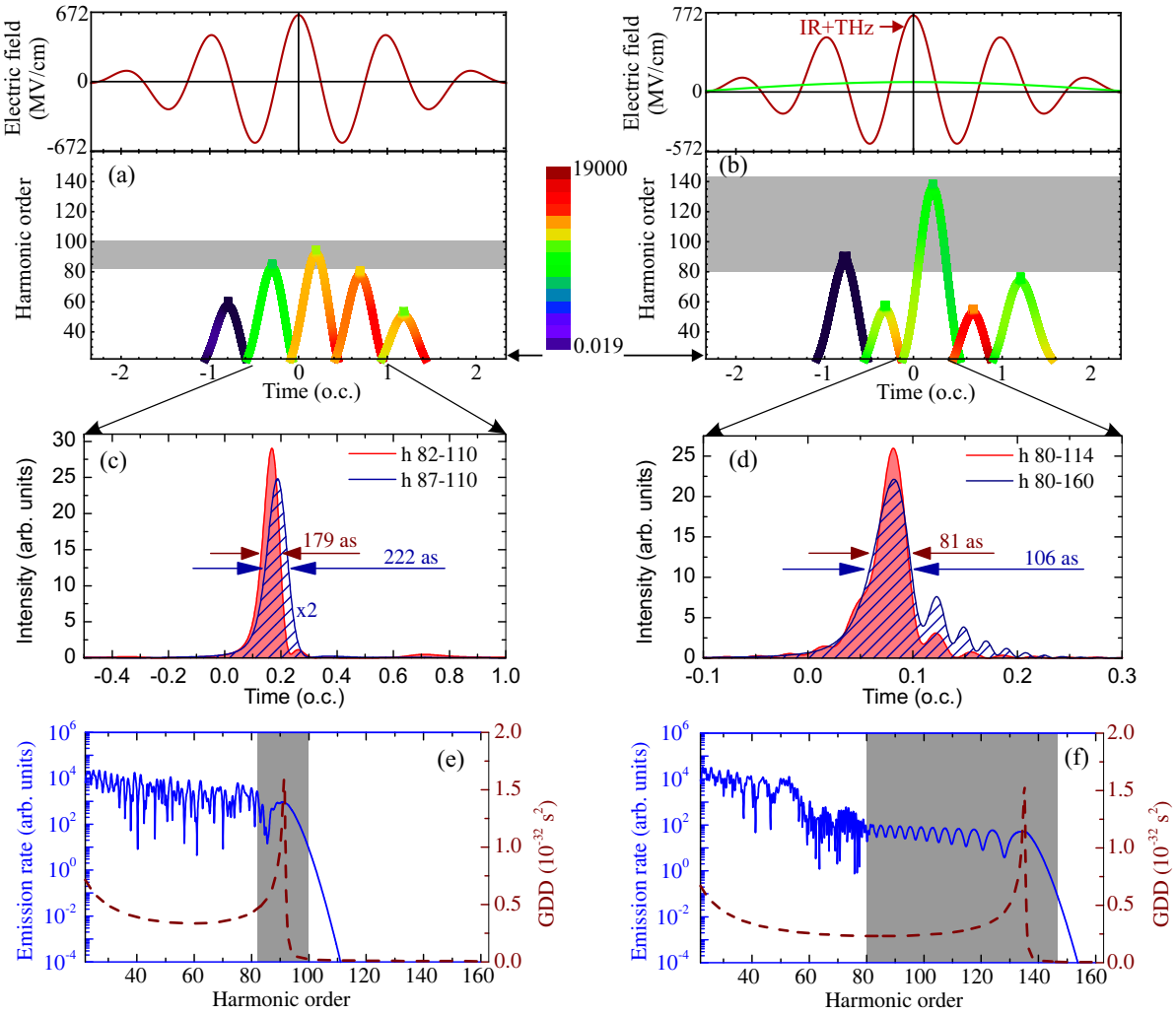

Figure III.3: *(a-b) Trajectories, (c-d) attosecond pulses, and (e-f) spectra produced by a few-cycle (5.2 fs, 6×10^{14} W/cm^2) laser pulse in the absence (left column) and presence (right column) of the THz pulse. The spectral range indicated by grey shading can be used for single attosecond pulse synthesis. Dark red, dashed lines on the bottom graphs show the group delay dispersion (GDD) of short trajectory components from the middle half-cycle of the laser pulse. Long trajectories have similar GDD values (not shown) but with opposite sign.*

sizing the attosecond pulses. In the laser-only case the shortest clean isolated attosecond pulses obtainable is 222 as (FTL 218 as) synthesized from harmonics 87 to cutoff (≈97). If we allow a SAP with a slightly worse contrast ratio of 1:50 (i.e. a small second pulse is also present), the SAP duration can be reduced to 179 as (FTL 159 as), synthesized from radiation above harmonic 82. In the THz assisted case the shortest SAP without compression is generated from harmonics 80 to 114, resulting in 81 as long SAP with a transform limited duration of 73 as. However, in this case a much wider spectrum can be used for SAP production if post-compression methods are available, reducing the shortest theoretically achievable SAP duration to 46 as.

As shown in Figure III.3 the extension of the cutoff also decreases the GDD of the plateau harmonics. Focusing on the middle half-cycle it can be seen that the GDD around the plateau is reduced from ≈4000 as^2 to ≈2400 as^2. The latter value is very similar to

what one would get from an IR pulse with 9.5×10^{14} W/cm^2 peak intensity that also produces a cutoff at harmonic 135 without an assisting field.

From single-atom calculations we can conclude that the effects of THz pulses on HHG are manifold: spectrally we observe an increase in amplitude in the lower plateau, and a large extension of the cutoff with reduced GDD. In the time domain the repetition of the attosecond bursts are modified. A comparison of the trajectories also shows that in the usual, laser-only case, the long trajectories carry the larger portion of radiation, whereas in the THz assisted case, there is a redistribution of electrons to the shorter trajectory class. When THz pulse is combined with few-cycle laser pulse the available bandwidth for SAP production can be significantly extended.

III.1.2 Macroscopic generation setup

In order to see if the predictions observed in single-atom calculations are robust against propagation, we further study the process using our macroscopic model. As described in Equation II.4.6, in this model the single-atom response is calculated from the full Lewenstein integral, which includes contribution from all trajectories. We keep the laser parameters used in the previous section, but reduce the THz wavelength to 8 µm which is more suitable to be used in the numerical model. In the two main cases to be discussed we use 0.3 mJ, 5.2 fs (or 0.47 mJ, 8 fs) pulses in a beam having 2 mm diameter, focused by a mirror of 0.6 m focal distance, resulting in a beam waist of 76 µm in the focus with a Rayleigh range of 22.9 mm. The peak amplitude of the THz field is the same 100 MV/cm as in the previous section (although here we do not restrict the THz pulse energy to experimentally demonstrated one).

Both the IR and THz pulses are treated as Gaussian beams, focused at the same spot. The 1 mm long gas cell containing neon gas with a pressure of 20 mbar is placed right after the focus. To have the best spatial overlap between the two pulses, the THz field is focused to have the same 76 µm beam waist, resulting in a Rayleigh range of 2.29 mm. Both pulses propagate in the same direction, having parallel linear polarization, and are synchronized so their peaks overlap at the focus. When the limits of the method or certain aspects of the process were tested, some of these parameters were changed, as specified later.

III.1.3 THz and laser field propagation

In case of these fields tunnelling is dominant over multiphoton ionization, a process strongly dependent on the electric field strength of the field, therefore it can be expected that the ionization rate is changed due to the presence of the THz field, even if that field is not capable of producing significant ionization alone. In Figure III.4(a) we can see that indeed the addition of THz field increases the peak ionization rate from 1.6 to 4.2%. At this rate and at such low pressure, however, the contribution to the refractive index is still

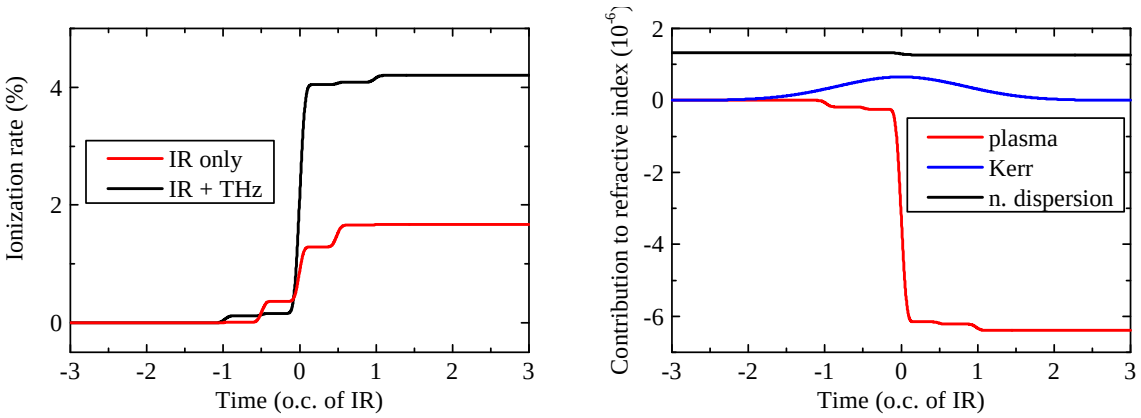

Figure III.4: *(a) Ionization rate caused by the IR (black line) and both the IR and THz fields (red line). (b) Different contributions to the refractive index at 800 nm. Plasma dispersion (red) being the most significant part, but still comparable with the Kerr nonlinearity (blue) and neutral dispersion (black).*

small enough for the IR field (see Figure III.4(a)) to pass through the whole cell without significant distortions. At the exit of the interaction region (after 1 mm propagation) the peak of the IR pulse on axis is ahead by ≈16 as, which is mostly caused by the Gouy phase shift that yields an 18.5 as change in the same direction.

In the case of low frequency fields like the THz field the effect of the plasma dispersion is particularly important because this scales with $(\omega_p/\omega)^2$ (ω_p and ω noting the angular plasma and electric field frequency). This means that for the 8 µm THz field, this effect is two orders of magnitude higher than in case of the IR, causing more significant distortions.

Figure III.5(a) shows that macroscopic effects are much more evident in the case of the THz field. Because of the 2.29 mm Rayleigh range, the Gouy phase shift is 0.4 radians at 1 mm from the focus, which yields a 1.74 fs shift of the pulse's peak, referenced to a plane wave propagating in vacuum. Since the plasma dispersion scales with λ^2 even a reasonably small ionization leads to a considerable distortion of the THz field. As the dominant part of the ionization happens when the IR field is present and especially around the peak of the IR pulse, the part of the THz pulse after this peak propagates through a medium with much higher electron density than the leading edge, therefore the effect of plasma dispersion is also considerably higher. This effect can be observed by comparing cases with weaker and stronger IR fields i.e. lower and higher ionization. When a 5.2 fs long IR pulse is used with 6×10^{14} W/cm^2 peak intensity (causing 4.2% ionization on axis) the main cause of the dephasing is the short Rayleigh range, however with a peak intensity of 10^{15} W/cm^2 the total ionization raises to 21.7% and the trailing edge of the THz pulse suffers from the effects of plasma dispersion. This can be seen in Figure III.5 where the initial field at the focus and the propagated fields at the exit of the interaction region (1 mm) are compared showing that the plasma dispersion introduces a significant blue-shift and loss of pulse energy during propagation. With longer, 8 fs pulses the ionization rate at 6×10^{14} W/cm^2 intensity is 5.8%, leaving the Gouy phase shift the main cause of dephasing.

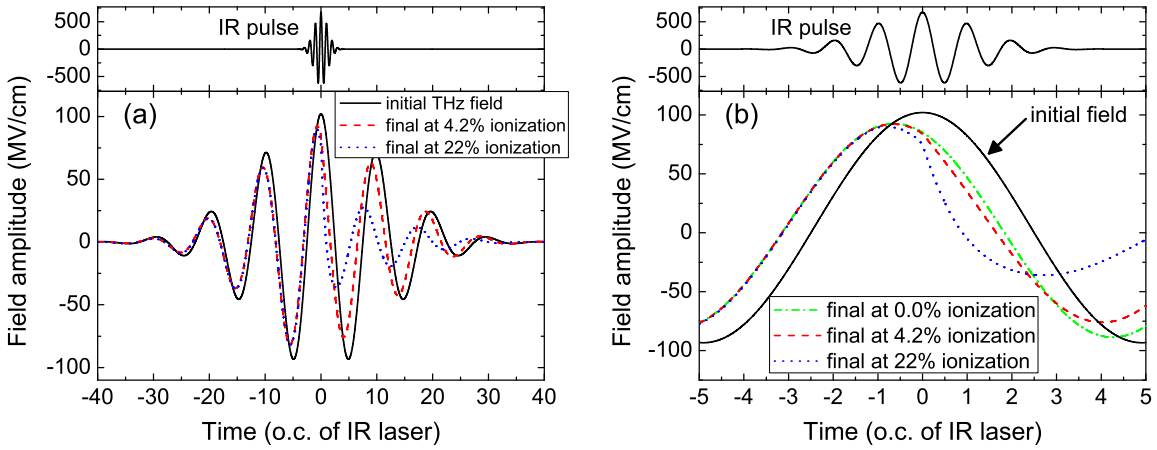

Figure III.5: *Electric field of the THz pulse at the focus (black solid lines) and after 1 mm propagation in the presence of a 5.2 fs laser pulse, with a peak intensity of* 6×10^{14} *W/cm*^{2} *(red dashed line) and* 10^{15} *W/cm*^{2} *(blue dotted line). The upper insets show the incident laser field for the* 6×10^{14} *W/cm*^{2} *case. (b) Central portion of the THz pulse's electric field in the focus (black solid line), and after 1 mm propagation in a medium with 0% (green dash-dotted line), 4.2% (red dashed line), and 22% (blue dotted line) ionization, indicating the strong distortion of the THz field due to ionization right after the peak of the IR pulse.*

III.1.4 Attosecond pulses in the near field

In this section we show the propagated, and radially integrated intensities of the harmonic bursts at the exit of the interaction region (i.e. in the near field), hence including all phase matching effects. SAPs can be obtained without the need of advanced gating techniques and control fields, "just" by using adequate spectral filtering, and sufficiently short laser pulses. For example, a 5.2 fs laser field with 6×10^{14} W/cm^2 peak intensity, generates a harmonic spectrum with a cutoff around the 90th order (see Figure III.6(a)). By selection of harmonics $\geq$81 an isolated attosecond pulse can be obtained at the single atom level (see Figure III.6(b)). For our conditions of cell length, pressure and ionization level, propagation does not distort the laser field. Additionally, the cell starts at the focus and we select cutoff harmonics, so the conditions for good phase matching are met [169, 64], thus a Gaussian-like pulse is observed in the near field. The duration of this pulse is 360 as produced at single atom level which becomes 225 as in the near field. Increasing the spectral window leads to the appearance of two additional attosecond pulses at half-cycle delay before and after the central one.

On addition of the 100 MV/cm THz field, the spectrum is reshaped to the familiar two-plateau structure, one ending at around order 81 and the other extending its cutoff to harmonic 135. As demonstrated by the trajectory analysis (Figure III.3), the second plateau of the spectrum contains only emissions from a pair of a short and a long trajectory, being emitted in a specific optical half-cycle. At the end of the interaction region the single atom cutoff is reduced to the 125th harmonic order as a result of the distortions (reducing amplitude, and phase shift) of the THz field during propagation.

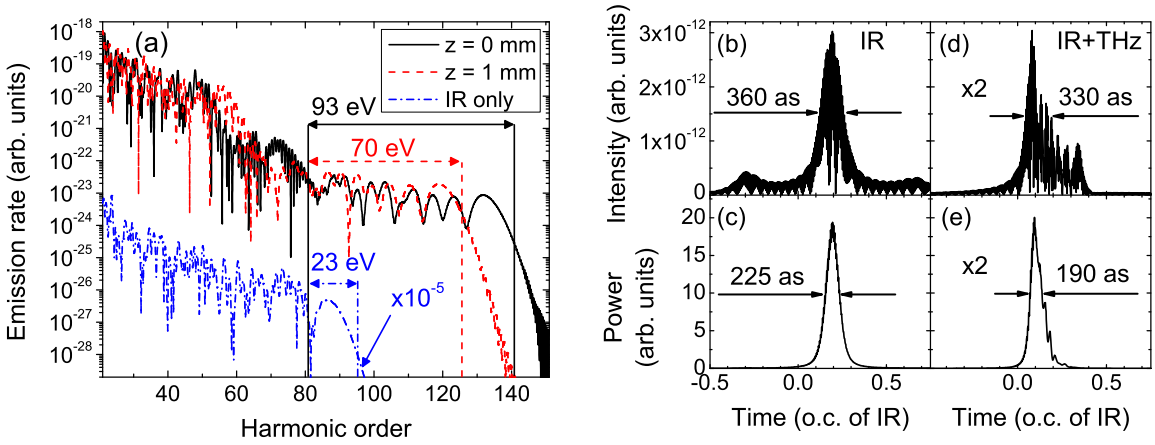

Figure III.6: *(a) Harmonic spectra from a single atom, generated at the beginning (black solid line) and at the end (red dashed line) of the cell obtained by using a 5.2 fs IR laser pulse combined with the 100 MV/cm THz pulse. The spectrum on the bottom (blue dash-dotted line) shifted 5 orders of magnitude downward shows the generated spectrum by the same IR pulse but without the THz field. (b) (d) The resulting attosecond pulse from the single atom response. (c) (e) the propagated and radially integrated harmonic field intensity (resulting power) at the exit of the interaction region. (b-c) IR-only case, (d-e) THz assisted generation. The attosecond bursts were synthesized by selecting harmonic orders ≥81 from the harmonic spectra.*

Using the same spectral filter as before (≥81st harmonic), a single burst is obtained with a duration of 330 as (FWHM). Although the spectrum is much wider than in the IR alone case, the presence of both trajectories and their phase modulation (chirp) produces a pulse duration comparable to that in the IR only case. At the exit of the interaction region macroscopic effects reduce the contribution from the long trajectory components, and hence the duration of the SAP to just 190 as.

When a longer laser pulse is used (8 fs, with the same 6×10^{14} W/cm^2 peak intensity, containing 0.45 mJ energy), the part of the spectra from orders 80 to 100 becomes more modulated, suggesting the interference of more trajectories. Using the same spectral filter as before (≥81), we obtain three distinct attosecond pulses generated at the single-atom level. However only the central one survives the propagation, and arrives to the exit of the interaction region with considerable intensity. The details of the macroscopic effects responsible for the cleaning and shortening of the attosecond bursts are discussed in the following subsection.

III.1.5 Phase matching effects

Due to the distortion of the THz field during propagation, the harmonic generation conditions vary substantially along the axial coordinate. The selection of the central burst seen in Figure III.7(b) in the 8 fs case also suggests that phase matching promotes only a distinct class of trajectories, and the others are eliminated because of destructive interference. To investigate phase matching of the single atom spectra during propagation, the propagated and radially integrated harmonic intensities (power density spectra) are

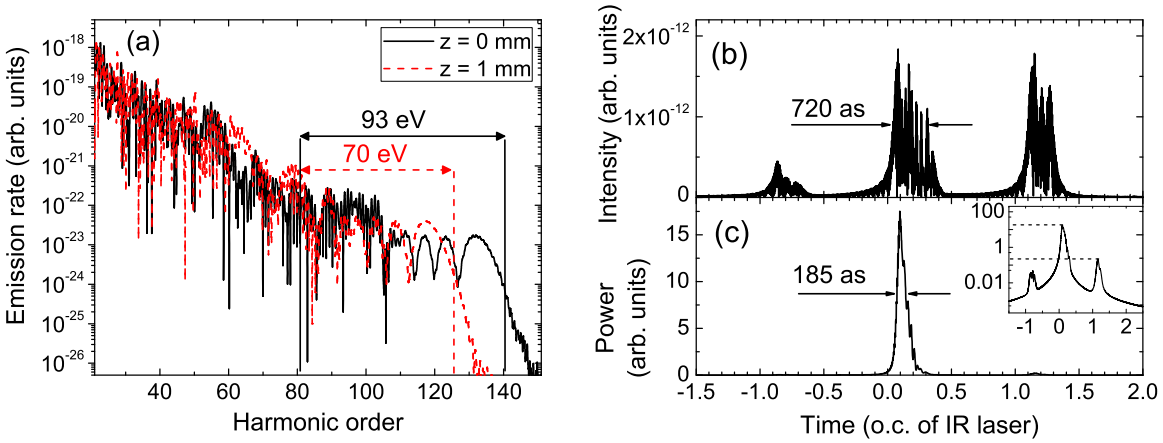

Figure III.7: *(a) Harmonic spectra from a single atom, generated at the beginning and at the end of the cell obtained by using an 8 fs IR laser pulse combined with the 100 MV/cm THz pulse. (b) The resulting attosecond pulse from single atom response obtained by selecting harmonics ≥81, and (c) the propagated and radially integrated harmonic field intensity at the exit of the interaction region showing a clean SAP. The inset in logarithmic scale shows a contrast of almost 10^2 between the main pulse and the second most powerful one.*

plotted at different axial (z) coordinates for the 6×10^{14} W/cm^2 case, see Figure III.8. For harmonics up to the order of 115 the spectral power increases with propagation distance, suggesting good phase matching for the whole length of the cell. On the other hand for the highest harmonics there is no increase for the second part of the cell.

Analysing the spatial structure of different harmonics along the r and z axes, one can see where good phase matching conditions are fulfilled for a specific harmonic (see Figure III.9). These maps show for example that the intensities of harmonics from order 81 to 101, which belong to the lower part of the plateau, undergo a constant increase along the propagation direction with the best rate slightly off axis. Harmonic 121 is phase matched close to the beam axis but only in the first part of the medium, while after ≈800 µm of propagation the field intensity decreases. The reason for this decrease is the phase mismatch of the specific harmonic and not the reabsorption of harmonic radiation by the medium. This claim is supported by the fact that the cutoff on axis is still slightly above harmonic 121 at the exit of the interaction region (see Figure III.7) and the absorption length is larger than 20 mm for this frequency and under these conditions.

We can conclude that the spectral power density in the lower and middle part of the plateau increases through the propagation, but this analysis is not conclusive on whether phase matching conditions promote certain sets of trajectories. This would have a strong effect on the shape, duration and chirp of the resulting pulses.

It is well documented that in HHG with only the IR laser pulse, mainly short trajectory components survive the propagation in a long interaction region, especially after focus, however, in gas cells only a few millimetres long, the contribution of long trajectories to the final pulse might still be significant in specific conditions [63]. As we have seen, the short- or long-trajectory origin of the resulting burst is important since it defines the

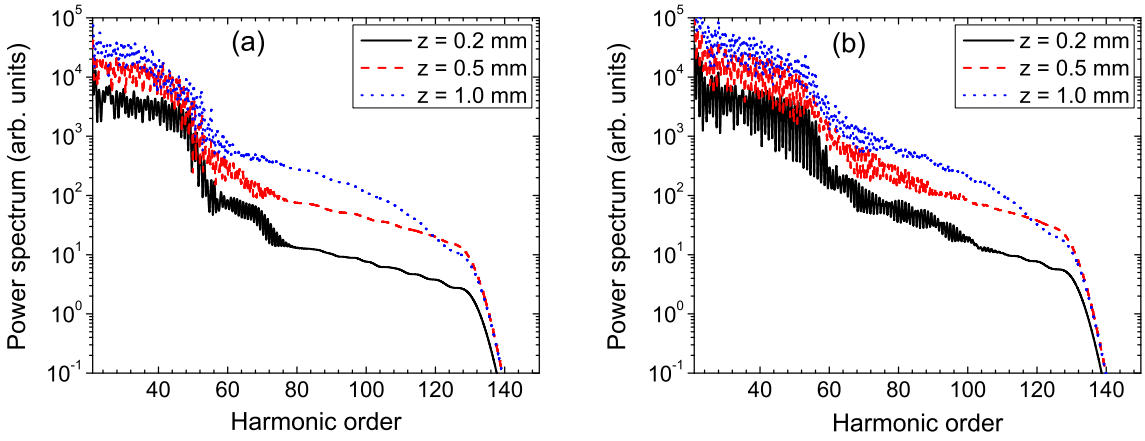

Figure III.8: *Radially integrated spectral intensity of the propagated field after different lengths of the gas cell for the (a) 5.2 fs, and the (b) 8 fs laser pulses combined with the 100 MV/cm THz pulse. The spectra shown for z=1 mm correspond to the temporal shapes shown previously in figures III.6 and III.7, respectively.*

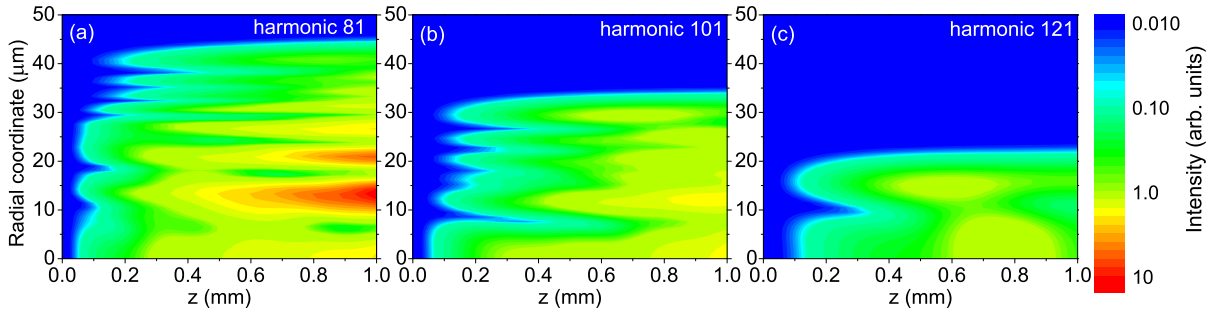

Figure III.9: *Spectral intensity of the propagated harmonic field as a function of radial and axial (z) coordinate for harmonic 81 (a), 101 (b) and 121 (c) calculated for generation with the 8 fs laser pulse.*

temporal, and may alter the spatial properties of the resulting attosecond pulses. Attosecond bursts from short/long trajectories have positive/negative chirp [15, 138]. Likewise, radiation generated from short/long trajectories usually has a lower/higher divergence [170, 67], making radiation from short trajectories more suitable for applications. Therefore it is important to investigate whether short or long trajectory components survive the propagation through a 1 mm long gas cell.

We mentioned in the previous subsection that the high frequency part of the single dipole spectrum ($\geq$81 harmonic order) consist of two sets of trajectories. This is visible in the temporal profile of the attosecond burst where the presence of short and long trajectories is observable as two separate peaks at a delay less than half IR optical cycle.

We present in the upper row of Figure III.10 the (t, r) map of the single dipole bursts produced by an 8 fs pulse at 6×10^{14} W/cm^2 at different propagation distances in the gas cell. We observe that the short and long trajectory components merge into the cutoff while the radial coordinate increases (corresponding to decreasing field strength). In Figure III.10(a) the short and long trajectory classes are indicated, as deduced from the trajectory analysis. As the laser and THz intensity decreases along the propagation

direction (due to beam divergence and plasma defocusing), there is no change in the generation of the central attosecond burst, whereas the post pulse strength decreases along the cell. This can be attributed to the accentuated decrease of the THz field amplitude and phase shift during propagation in the ionized medium, which decreases the cutoff at that specific half-cycle to near the lower limit of the spectral domain from which the harmonic burst is synthesized.

The same set of plots has been produced for the propagated harmonic fields (bottom row of Figure III.10) to study the effect of phase matching. Two bursts separated by an IR optical cycle are observed, similar to the single atom results above. While the main burst is building up during propagation, the strength of the post pulse is decreasing suggesting unfavoured phase matching. Most importantly, we would like to point out that, although long trajectory components are generated at any axial coordinate along the cell (top graphs in Figure III.10), they gradually disappear from the propagated field, suggesting phase mismatch for these emissions. We conclude that harmonic emissions from electrons travelling along short trajectories are well phase matched during propagation, while those from long trajectories are gradually eliminated by destructive interference.

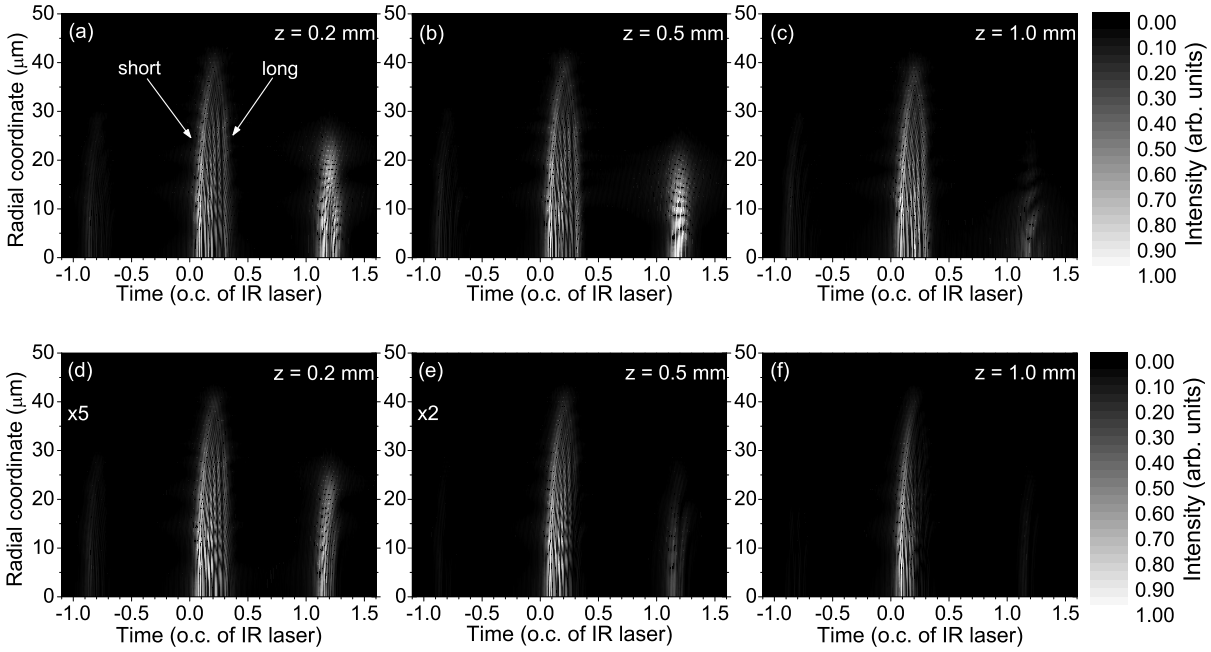

Figure III.10: *(a),(b),(c) Harmonic field intensity of the generated single atom emission at different axial (z) and radial (r) coordinates, and (d),(e),(f) the intensity of the propagated field at the same coordinates.*

III.1.6 Parameter sensitivity

Now we review the effect of several parameters on SAP production, the reference parameters being the ones described in subsection III.1.2 in particular we remind the reader that we used an 8 fs laser pulse with a peak intensity of 6×10^{14} W/cm^2, focused to a 76 μm beam waist into a 1 mm long gas cell with 20 mbar pressure. The peak amplitude of the

THz field was 100 MV/cm. By selecting harmonic orders ≥81 this configuration yielded a SAP with 185 as duration and a contrast ratio of 85:1. In each of the following subsections the effects of varying one parameter is discussed, except in subsubsection III.1.6 where the delay between the IR and THz pulses and the length of the interaction region are discussed together.

Laser pulse duration

For the duration of the IR pulse, we see that the shorter the pulse the better for the positive effects of the THz field, although we did not explore extreme cases like sub-cycle pulses. Using 5.2 fs laser pulses the continuum part in the near field spectrum starts at the 71st harmonic order and therefore a much wider spectral range can be used for SAP production. However, because of the chirp of the resulting harmonic pulse, the wider spectral range does not decrease the duration of the obtained SAP, this can be balanced by eliminating cutoff harmonics by spectral filtering. For example, for a 5.2 fs pulse and selecting harmonic orders 81-115 a 160 as pulse is predicted. To take advantage of the broad bandwidth an XUV pulse shaping method needs to be implemented to obtain transform limited pulses [171, 167]. With a suitable chirp compensation technique the IR only SAP duration of 225 as is reduced to 210 as, while the 185 as pulse generated in the presence of the THz field is reduced to just ≈50 as.

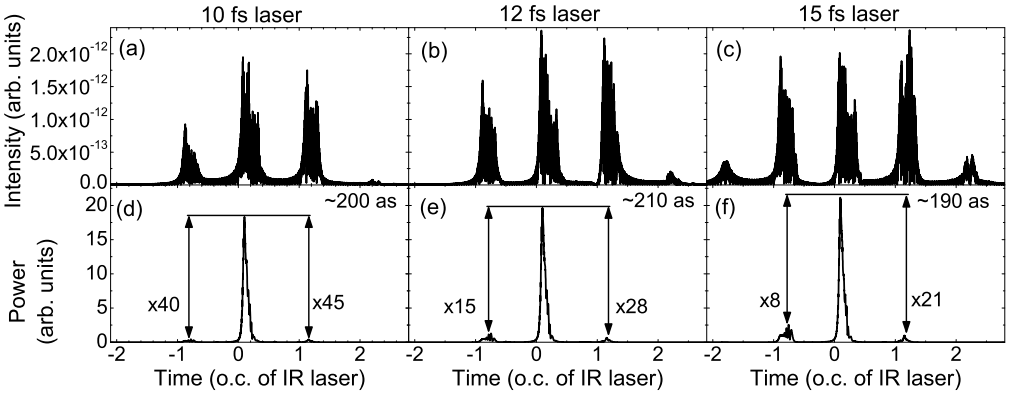

Figure III.11: *Generated harmonic bursts at the single atom level (top row) and the propagated and radially integrated harmonic field intensities at the exit of the interaction region (bottom row) for different generating laser pulses having 10 fs (a) and (d), 12 fs (b) and (e), and 15 fs duration (c) and (f), assisted by the THz field.*

Longer laser pulses may be used for SAP production, but this affects the contrast. Using the same spectral filtering (harmonics ≥81) and a 10 fs laser pulse the contrast is decreased to 40:1 and this ratio is further decreased to 15:1 with 12 fs, and to 8:1 with 15 fs pulses. By increasing the lower limit of the spectral filter the contrast can be slightly increased at the cost of reduced power of the main pulse.

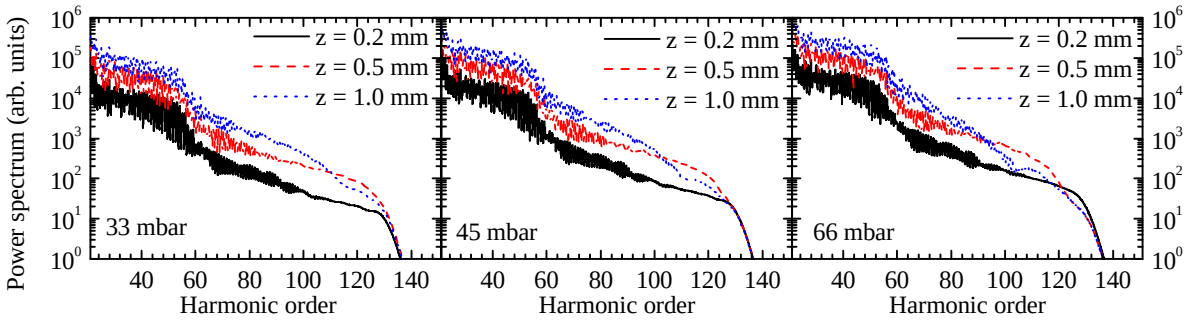

Figure III.12: *Radially integrated spectral intensity of the propagated field after different lengths of the gas cell for 33, 45 and 66 mbar gas pressure showing the detrimental effect of high gas pressure on the phase matching of cutoff harmonics.*

Gas pressure

The increase of the gas pressure has a detrimental effect for the phase matching in the high frequency range thus narrowing the spectral range available for SAP generation. However, due to the GDD of HOH, the elimination of the highest frequency radiation also makes the resulting SAP slightly shorter. We found that the optimum pressure in terms of contrast ratio is around 33 mbar. At this pressure the contrast is increased to 170:1, the peak power of the SAP is doubled and its duration is reduced to 165 as when the same spectral filtering as before is used. On further increase of the gas pressure the pulse duration is further decreased to 140 and 130 as with 45 and 66 mbar gas pressure respectively; however, this also results in a decrease in contrast to 130:1 and 35:1.

Optimal cell length and delay between THz and IR pulses

Another important parameter is the length of the interaction region, the optimal value of which is limited by phase matching conditions and reabsorption. With the base configuration where the Rayleigh range of the THz pulse is 2.29 mm the most powerful SAP can be obtained with a 1.3 mm long cell. In this case the near field SAP duration is reduced to 150 as and the contrast is increased to 130:1.

By scanning the delay from -2.0 fs (IR pulse behind) to 1.5 fs (IR pulse ahead) the near field cutoff is increased from harmonic 85 to 125. When the IR is 1.5 fs ahead, the near field spectral power density for harmonics in the cutoff region is increased 4.5 times compared to the case without delay (using a 1 mm cell in both cases). However, by putting the IR pulse ahead of the THz by 1.5 fs, the optimal cell length (in terms of harmonic pulse power) is also increased from 1.3 to 2 mm. In this case the harmonic pulse's peak power is doubled, the duration of the obtained SAP is 150 as, and the contrast is 75:1.

Laser pulse energy

By increasing the IR pulse energy we could still generate SAP and favourable phase matching for the short trajectories. Of course, due to the increased cutoff we also adjusted the spectral filtering for an optimum SAP generation. For 8×10^{14} W/cm^2 peak intensity

(8 fs pulse, 16.4% peak ionization) a 165 as SAP is produced with a contrast of 230:1 when harmonics ≥101 are selected. Further increasing peak intensity to 10^{15} W/cm^2 the resulting ionization is 32%, (compared to 21.7% in Figure III.5(b) with a 5.2 fs laser pulse having the same peak intensity) which affects very strongly the THz field propagation in its trailing edge. The gating effect of the THz pulse is still present, and a SAP with 150 as duration and a contrast of 100:1 is obtained in the near field (by selecting harmonics ≥111). In this case the single atom cutoff is at harmonic order 191, although by the end of the 1 mm gas cell it decreases to order 142 (without the THz field the cutoffs are at harmonic orders 136 and 121, respectively). Without the THz field, by use of the same spectral filtering two almost identical pulses are obtained (concerning their duration and peak power) with half the IR optical cycle delay between them, and a third one having much lower peak power is also observable.

III.1.7 Summary

- **T1.a I have analysed high-order harmonic generation in the presence of strong THz fields, and I have shown that: THz pulses can cause a large extension of the cutoff with reduced GDD, and they can redistribute the amplitude of electron trajectories, making the shorter trajectory class more dominant. Besides the different trajectory lengths, the increased field strength at the moment of ionization (due to the shifted ionization times) also contributes to the stronger yield from short trajectory radiation.**

- **T1.b I have studied how in a macroscopic environment the generation process differs significantly from the single-atom results, and shown that even in cases when longer laser pulses are used (8, 10 or 12 fs) and the single atom response would yield multiple attosecond pulses, propagation effects can eliminate the contribution from certain sets of trajectories, yielding an isolated attosecond pulse at the exit of the gas cell. The large bandwidth of these pulses greatly decreases their transform limit.**

  I have also shown that the long-trajectory components are also cleaned from the surviving pulse during propagation, resulting in an effective decrease of pulse duration, making the technique promising for obtaining a reliable source of short, isolated attosecond pulses with good contrast and low divergence. By careful adjustment of the parameters, such as gas pressure and peak intensity of the laser pulse, and by adequate spectral filtering short SAPs can be produced in a straightforward manner (without post-compression).

III.2 Optimization of focusing geometry in THz assisted HHG

In the previous sections we have shown that there are significant differences between micro- and macroscopic results, and the use of long wavelength assisting pulses favour the isolation of a single attosecond pulse even beyond the predictions of single-atom calculations. However, it has also been shown that phase-mismatch caused by dephasing and distortions of the pulses limits the use of longer gas cells or higher gas pressures, significantly limiting the achievable energy of the generated pulse. Now, after understanding the main aspects of THz assisted HHG, we carry on an analysis on what is the most advantageous configuration to be used experimentally, when we limit ourselves to the experimentally demonstrated THz pulse energies.

HHG being a coherent process, the photon number of harmonics increases quadratically with the number of interacting particles, therefore an increase in cell length can increase the attosecond pulses energy considerably under phase-matching conditions. So far we have seen that the THz and laser pulse go out of phase due to their different Gouy phase shift around the focus and also due to the strong plasma dispersion affecting the long wavelength THz pulse. This leads us to the use of pulses with smaller difference between their wavelength, in hope of better overlap through longer cells and smaller distortions leading to better phase-matching.

The method of DFG used by Sell et al. [155] to produce the intense THz pulse has the advantage of tunable central wavelength, and their measuring technique allowed the characterization of the generated pulses up to 72 THz central frequency. This frequency already corresponds to 4.17 µm wavelength, that is well in the region called MIR radiation, however, as the limits between these regions are not strictly defined, they kept the THz name for these pulses as well, and so will we during this chapter. Although, probably at this frequency the pulse energy achieved in the experiment is smaller than the peak 19 µJ, we do not have information about these parameters, therefore in our calculations we limit the THz energy to this value, and optimize the parameters under this limitation.

To optimize the generating conditions in this new configuration the effects of several parameters is studied. The focusing geometry is optimized, limited by the constraints of using maximum spatial overlap between the IR and THz pulses (i.e. same beam waist). Besides the focusing conditions the delay between the two pulses, the length and position

of the gas cell is optimized to generate short and powerful SAPs of high energy photons. In the previous section we have seen that the generated plasma – when using high IR intensities – distorts the THz pulse, therefore we optimize the focusing geometry while keeping the peak intensity of the IR pulse at 6×10^{14} W/cm^2 (this means that the IR pulse energy is adjusted for each configuration). On the other hand, in case of THz fields the pulse energy is limited in experiments, therefore we fix this energy to the demonstrated value (this means that in each focusing configuration the THz field strength is changed).

III.2.1 Disadvantages of tight focusing geometry

In the THz generation experiment to get the highest field strength of 100 MV/cm the pulses were focused to 31 µm beam waist. We assume beam diameters in our first configuration such that a focusing element with 0.6 m focal length produces this beam waist for both fields. In this case the cutoff of the harmonic radiation can be extended to harmonic 130 in the near field (see Figure III.13) when an 8 fs, 78 µJ IR pulse is focused in a 2 mm long target cell. However, the tight focusing used to obtain the extreme high electric field of the THz pulse results a Rayleigh range of just 0.7 mm (3.7 mm for the IR beam), which is not beneficial to phase match the generated harmonics as illustrated in Figure III.13.b showing decreasing signal after 2 mm propagation. By increasing the beam waist the peak intensity of the THz field drops, limiting the achievable cutoff, but helping to phase match the higher spectral components.

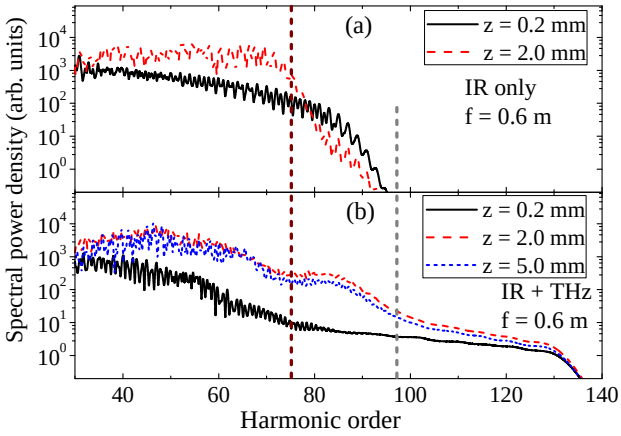

Figure III.13: *Spectral power density of the propagated harmonic field at the exit of a 0.2 mm (black solid lines) and 2.0 mm (red, dashed lines) gas cell for the cases when only the IR field (a) and when the combined fields (b) are focused by a $f = 0.6$ m mirror, producing a beam waist of 31 µm. The blue dotted line on graph (b) represents the same quantity for a 5 mm cell showing the decreased yield due to phase mismatch in the tight focusing conditions. The vertical lines at harmonic 75 and 97 show the lower limit of spectral filtering used to synthesize the attosecond pulses discussed later.*

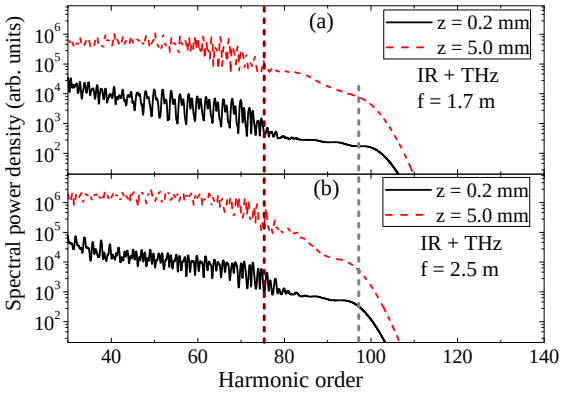

Figure III.14: *Spectral power density of the propagated harmonic field at the exit of a 0.2 mm (black solid lines) and 5.0 mm (red, dashed lines) gas cell when both the IR field and THz fields are focused by a f = 1.7 m (a), and by a f = 2.5 m mirror (b) producing beam waists of 85 and 125 µm respectively. The vertical lines at harmonic 75 and 97 show the lower limit of spectral filtering used to synthesize the attosecond pulses.*

III.2.2 High intensity single attosecond pulses

Using f=1.7 m focusing and 0.585 mJ IR pulse energy the corresponding beam waist is 85 µm; the addition of the THz field with 38 MV/cm peak amplitude and same 85 µm waist extends the cutoff by 20 harmonic order (see Figure III.14.a), reaching harmonic 100 compared to the cutoff at harmonic 80 obtained using only the IR pulse. The plateau region is phase matched during propagation through a 5 mm gas cell. This configuration supports the production of 145 as SAP obtained by selecting harmonics above harmonic 75 (see Figure III.15.e). The larger interaction volume resulting from the increased spot size and favourable phase matching conditions through a 5 mm cell result in an increase of more than two orders of magnitude in the peak power of the generated SAP (see Figure III.15 d,e,f), despite the lower cutoff (i.e. narrower bandwidth).

Further loosening the focusing geometry (f = 2.5 m, 125 µm beam waist, 1.25 mJ IR pulse energy) the amplitude of the THz field drops to 27 MV/cm and the cutoff is extended by only 13 harmonic orders (Figure III.14.b) compared to the IR only case with a cutoff at harmonic 80. Using the same spectral filtering ($\geq$75), satellite pulses appear around the main pulse, and the peak power of the main pulse does not increase significantly (see Figure III.15.f and Table III.1) despite the larger interaction volume.

Our analysis shows that the production of 97 as SAP (f=0.6 m) is mainly attributed to the elimination of long trajectory components by phase mismatch. These pulses reappear on Figure III.15.f due to the decreased THz field strength in looser focusing.

By increasing the lower limit of the spectral filtering SAP still can be obtained at the cost of reduced power. Selecting only harmonics 97, SAP can be obtained in all the focusing geometries used so far (see Figure III.16 and Table III.1). However, the loose focusing (f=2.5 m) also shifts the cutoff below harmonic 97, resulting a reduced pulse power compared to the case with f=1.7 m focusing. We note that the SAP obtained this

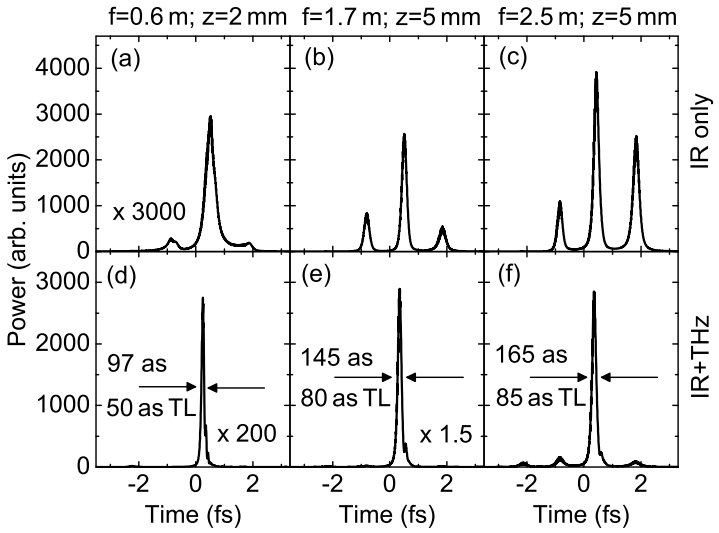

Figure III.15: *Attosecond pulses obtained by selecting harmonic radiation above harmonic 75 using different focusing geometries with the IR only (top row), and with the combined field (bottom row). The transform limit of the pulses is also shown in cases when SAP is obtained.*

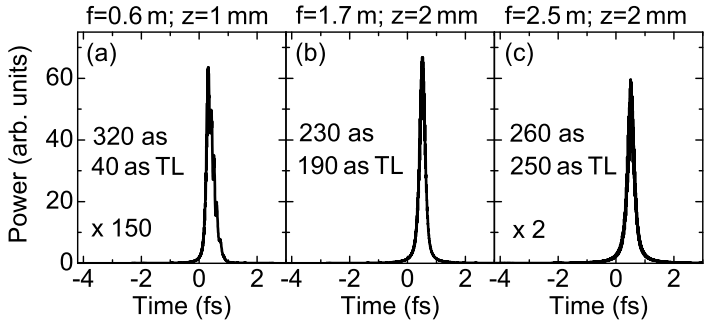

Figure III.16: *Attosecond pulses obtained by selecting harmonic radiation above harmonic 97 using different focusing geometries with the combined field. The transform limit of the pulses is also shown.*

way is nearly transform limited (Figure III.16.c), because cutoff harmonics possess no chirp [26], and the bandwidth is very narrow.

The 50 as transform limit of the SAP presented in Figure III.15.d corresponds to an effective bandwidth of 23 harmonics (with a time-bandwidth product of 0.44, characteristic of Gaussian pulses), which can be explained by the strong drop of the harmonic yield at ≈145 eV seen in Figure III.13.b. By selecting only harmonics above 97 the spectrum is flatter which explains the shorter transform limit of the synthesized SAP shown in Figure III.16.a.

As seen earlier, the differences in the degree of cutoff extension by the THz field at different focusing geometries can be attributed not only to the different amplitude of the THz field, but to macroscopic effects as well.

A summary of the results is presented in Table III.1. The values for SAP duration, peak power, and contrast presented in the table are calculated for the optimal cell lengths in the actual focusing geometry, whereas the values presented in figures Figure III.15 and

f	E_{THz}	$L_{optimal}$	cutoff	SAP duration	SAP peak power	contrast
-	-	h 75/97*	-	h 75/97	h 75/97	h 75/97
(m)	(MV/cm)	(mm)	(h.o.)	(as)	(arb. units)	(dB)
0.61	108	2.1 / 0.6	132	**97** / 136	14.2 / 0.62	22.3 / 34.4
1.1	60	5.1 / 1.6	105	110 / 184	384 / 24.1	22.1 / ∞
1.7	38	5.2 / 2.3	100	150 / 230	1947 / **68.2**	21.6 / ∞
2.45	27	4.3 / 2.1	95	174 / 260	**3085** / 29.8	12.2 / ∞

*h 75/97 stands for distinguishing the two spectral filters

Table III.1: *Summary of the THz field and SAP parameters obtained for different focusing geometries using two different spectral filters, and cell lengths optimized for SAP peak power. Contrast ratio labelled ∞ means that the contrast is higher than the precision of our calculations ($\approx 10^7$).*

Figure III.16 are calculated for cell lengths more commonly used in experiments. The contrast ratio is defined between the peak powers of the two most powerful attosecond pulses.

For the position of the gas cell we have found that the most reliable solution is to place its entrance at the focus. With the looser focusing geometries slightly better results were obtained by moving the cell 1 mm before the focus, however the increase is not significant. With the f=1.7 m case for example 10% increase can be obtained in the SAP peak power when an extended, 6 mm long cell is placed beginning 1 mm before the focus.

III.2.3 Quantum path control

So far the two pulses were assumed to be synchronized, i.e. to have a field maximum at t=0. In this case the short trajectory components are phase matched and the corresponding long ones are eliminated due to phase mismatch. To demonstrate the effect, the intensity of the propagated XUV pulse is plotted in (r,t) maps (see Figure III.17).

First we calculate the radiation produced in a very short cell (0.2 mm, see Figure III.17.a), where macroscopic effects do not start to play, and such illustrating the single atom results. As seen earlier both short and long trajectory radiation is generated in the cell, however the long ones gradually disappear from the propagated field due to phase mismatch (see Figure III.17.b). Short trajectories dominate the harmonic radiation already after 1 mm propagation (not shown), with the long ones completely eliminated after 2 mm.

Using the same f=1.1 m focusing mirror, (56 µm beam waist) and delaying the THz pulse by 1 fs compared to the IR, we observe an almost identical field intensity map at the beginning of the cell (see Figure III.17.c). However, during propagation only long trajectories are phase matched in the first mm of the gas cell, with the corresponding short ones eliminated (see Figure III.17 bottom row).

To understand this effect, we analyse phase-matching of short and long trajectories in these conditions. When both IR and THz fields are present the harmonics in question are

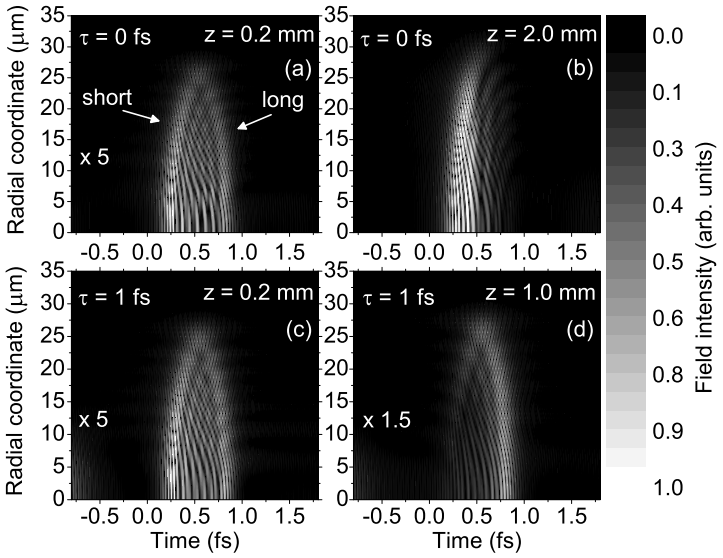

Figure III.17: *Intensity maps in (r,t) of the propagated harmonic field at different axial (z) coordinates. Top row shows the selection of short trajectories by phase matching after 2 mm propagation in case of 0 delay, while the bottom row shows the selection of long trajectories by phase matching after 1 mm propagation obtained by delaying the THz field by 1 fs compared to the IR. In this case f=1.1 m focusing is used producing 56 μm beam waist.*

well in the plateau region, therefore short and long trajectories have significantly different intensity-dependent phases. In Figure III.18 the total phase of a selected harmonic (of order 81) is shown along the propagation axis. In case of short trajectories the drop in

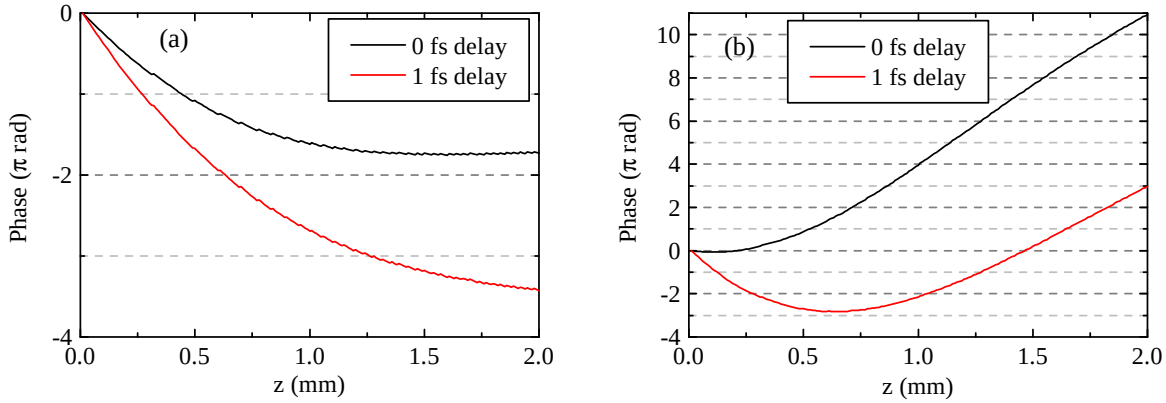

Figure III.18: *Phase of the generated harmonic (order 81) along the propagation axis for short (a) and long (b) trajectories.*

intensity caused by the divergence and phase shift of the THz field compensates for the phase mismatch.

When the THz field is initially delayed by 1 fs, at start its field strength is lower in the half cycle where this attosecond pulse is generated. After the focus the Gouy phase shift compensates for the initial delay, and causes the effective field to drop slower in the first part of the cell. As a result, in this configuration phase-mismatch is increased for short trajectories, but there is a region where the long trajectories have an almost constant

phase (between 0.3 and 1 mm in Figure III.18(b)).

These results also show that the variation of the assisting fields can compensate for phase-mismatch arising in the medium. We conclude that by using well chosen focusing and varying the delay between the THz and IR pulses, the selection of long trajectories can be achieved allowing one to select the sign of the chirp of the resulting SAP.

III.2.4 Summary

- **T2.a I have analysed the importance of focusing geometry on phase matching and harmonic yield in HHG when the IR pulse is assisted by a THz pulse, using experimentally verified parameters. I have shown that, despite the limited THz pulse energy, the most powerful SAP can be produced by relatively loose focusing. I attributed this to the deteriorated phase-matching conditions under strong focusing of the long-wavelength fields.**

- **T2.b I have shown that the assisting field can be used to compensate phase mismatch that arises during harmonic generation and the selection of the short or long trajectory components (defining the sign of the resulting SAP's chirp) can be achieved by varying the delay between the THz and IR pulses.**

Legal notes

III.3 Attosecond pulse generation by synthesized light transients

So far we have seen how the mixing of electromagnetic fields with different wavelengths can alter the electron trajectories producing isolated attosecond pulses, or increasing the efficiency of the HHG process in long interaction regions. In these processes the tunable parameters were the strength of the generating and assisting fields and their relative delay, which adds up to just 3 independent variables, and despite this, we have seen widely different results.

The ultimate tool in manipulating electron trajectories would be a field synthesizer that can produce arbitrary waveforms. Recent development in ultrashort laser pulse generation yielded a tool that gets close to this goal, these are the light field synthesizers [172, 173]. Such a device is based on the spectral separation of laser radiation

to 3 or more interferometer channels where amplitudes, CEP values and relative delays are independently adjustable. These instruments promise unique possibilities for highly-controlled attosecond pulse generation, however, from the practical point-of-view, one needs to consider the large number of degrees of freedom in such a tool. The two or three independently controllable parameters for each spectral channel, together with spectral filtering of the harmonic beam creates a parameter space with so many dimensions that is already infeasible to be scanned experimentally in order to study its capabilities in attosecond pulse production.

Numerical calculations allow us to test the theoretical limits of these tools, and also to predict their possible uses, although in the calculations we face the same challenge: the parameter space is too large, hence we need fast calculations and advanced numerical tools. As complete 3D calculations can take very long time, here we rely on single-atom predictions. We have seen that the dipole response of an atom to the laser field can be calculated using Equation II.7 and attosecond pulses are obtained by spectral filtering of the dipole radiation, from the point of view of numerical calculations we can treat this as a highly nonlinear, multivariable function. Widely used tools in optimization of such functions are genetic algorithms, which enable the search for a parameter set that would produce a predefined result, in our case, attosecond pulse(s) with specific features.

In fact, evolutionary algorithms have been used in numerical calculations of HHG to optimize harmonic yield [174, 175, 176] and phase matching [177], extend the cutoff [178, 179], and to generate single attosecond pulses SAPs [180, 157]. The optimization of several experimental HHG setups has also been carried out with self-learning algorithms [181, 182, 183, 184]. In order to study the possibilities offered by light field synthesizers in attosecond pulse generation, in our numerical optimization we set the goals to produce the shortest possible isolated attosecond pulses, and attosecond double-pulses with variable separation between them.

III.3.1 Model and approximations

We are modelling a light field synthesizer with four spectral channels. Three of the spectral channels emulate that of an experimental setup described in [172], and the fourth one is an UV channel added to have more freedom in light field synthesis, and also because technical development is heading in this direction.

As this area of laser technology is developing quickly, and also because the available field intensity from each spectral channel depends on the focusing geometry, in our calculations we did not restrict this parameter to the experimentally demonstrated one, but we assumed infinite freedom of the parameters. The only limitation we use in the optimization is related to the peak intensity of the synthesized pulse, set to 1.5×10^{15} W/cm^2. We fixed the peak intensity of the synthesized laser pulse to eliminate this effect from the interpretation. Because both the bandwidth and phase locking of the generated harmonics are improved by increasing the driver intensity [61], this strongly affects the characteris-

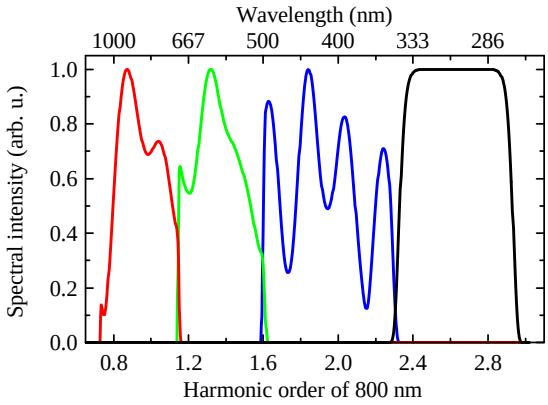

Figure III.19: *Spectral channels of the driving wave from 1040 nm to 272 nm. The boundary wavelengths correspond to 698 nm, 501 nm and 347 nm. We extended the three experimentally demonstrated channels with a fourth super-Gaussian in the UV range.*

tics of the attosecond pulse, and we set the goal to analyse the effect of the adjustable pulse shape. At this intensity the generating sub-cycle pulse produces an ionization rate of ∼15–22% (depending on the pulse shape) in neon, that is still feasible to be used experimentally. As a result we have as free parameters the relative intensities of each spectral channel (Figure III.19), their relative delay, their CEP, and also the lower and upper limits of the spectral filter applied to the harmonic radiation.

The genetic algorithm starts from a set of randomly chosen points in the parameter space, calculates the produced attosecond pulses for each, checks these against the predefined goal, and assigns a "fitness" value to each depending on how well they fit to the requirements. After this, the fittest individuals are kept and several mutations of these are created, i.e. a few of their parameters are altered, to create a new set of points in the parameter space, and the whole process starts again, until the results are close enough to the desired goal. After the optimisation is finished, we analyse the obtained results and test them against propagation to see if they keep their advantageous features.

Earlier we have seen that single atom predictions are closer to macroscopic results if the effect of long trajectories is eliminated, but even in these conditions, macroscopic processes may alter the final result significantly. Trajectory selection is straightforward when using the saddle-point method for sinusoidal generating fields, however here we use experimentally measured light fields, and these cannot be described by simple analytical formulae, we only know the numerical values of the electric field in different time steps. The main problem is that the saddle-point approximation requires the knowledge of the electric field and its vector potential for complex values of time, and these calculations have only been demonstrated either by approximating the complex part of the function using tailor expansion [185], or by approximating the function itself by a high-order polynomial [186]. Both of these methods get less accurate by increasing the complexity of the waveform and neither was tested for such unusual fields light-field synthesizers can produce. Therefore we rely on the calculation of the full Lewenstein integral in obtaining

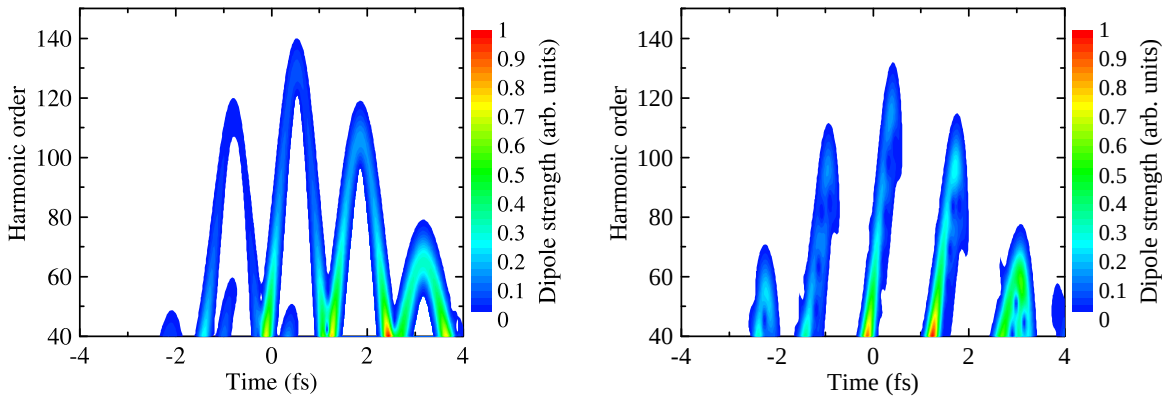

Figure III.20: *Gabor transform of the dipole acceleration generated by a 5 fs Gaussian laser pulse and calculated using the Lewenstein integral. In (a) the length of the integration region is 1.1 optical cycle, including both short and long trajectories, in (b) this is limited to 0.6 optical cycles, eliminating most contributions from long trajectory components.*

the single-atom response.

When calculating equation Equation II.7 the lower t' and upper t limits of the integral define the longest electron travel time that is accounted for in the model. By limiting the integration to a short time region, the emissions from recombining electrons that perform long trajectories can be minimized (see Figure III.20), and we chose this method to emulate the macroscopic elimination of long trajectories in the genetic algorithm.

In the field synthesizer the central frequency of the generated pulse may vary on a wide range, and its broad spectrum also enables the production of pulses possessing strong chirp, thus for each parameter set classical calculations are performed to find the travel time of electrons belonging to the cutoff trajectory. This value is then used to define the length of the integration time. This method should give a reasonable first approximation, as it has been demonstrated also experimentally that the classical calculations give a good approximation of the ionization and recombination times in the HHG process, especially in the case of harmonics well above the ionization potential [62].

To verify the approximations of long trajectory elimination by limiting the integral we perform macroscopic calculations. In the 3D model we assume Gaussian beams with 40 µm beam waist for all four fields, and a gas medium placed at their common focus. In these calculations single-atom response over the interaction region is calculated without restricting the integration time in equation Equation II.7. We assume linear polarizations in a common direction for all fields, thus the single-atom response is also linearly polarized in the same direction and enters the source term for the wave equation describing the propagation of the harmonic field. The final result of this step is the harmonic near field at the exit of the gas medium. The far field is calculated by propagating the harmonic field through an aperture and refocusing in a 2f-2f geometry. This procedure basically reproduces the near-field at the focus, but eliminates the components with high divergence (blocked by the aperture).

As we calculate the ionization using the ADK model [187], which loses accuracy when applied to few-cycle pulses [188], we tried to minimize the role of ionization in our interpretation of the macroscopic results. To this end, no optimization of the macroscopic parameters has been carried out, apart from selecting a gas pressure which favours the phase-matching of short trajectories (in our case this varies from 20 to 66 mbar), something that is usually the case in experiments as well. We mention that in the results to be presented here the effect of gas pressure is not significant when this is kept between the previously mentioned limits. The only exception from this is the case of double-pulse generation with 300 as separation, where the role of long trajectories is significant, and single-atom results could only be reproduced by using the lower gas pressure of 20 mbar. The length of the gas cell is also limited to just 0.6 mm in all cases.

III.3.2 Isolated attosecond pulses

Today the shortest SAP demonstrated experimentally is 67 as long, produced with double optical gating and compressed through a zirconium filter. That setup uses polarization gating to isolate a SAP from a pulse train, and advantageous macroscopic effects to eliminate high group delay dispersion harmonics close to the cutoff that would make the generated pulse longer [150]. Without the use of the polarization gating technique, the shortest SAP demonstrated is 80 as long, measured after passing through a zirconium foil used for post-compression [149].

If we take a driver pulse that can be derived from the light field synthesizer spectrum (Figure III.19) with constant spectral phase (i.e. no optimization performed) and normalize to the peak intensity we are using, we can generate a SAP with 73 as FWHM pulse length with only the single atom response considered. Therefore, we set out to see first whether a genetic optimization process of the driving field can deliver a shorter pulse, restricting the intensity contrast ratio of the possible side-pulses to at least 1:10.

The GA converged to a solution, where the optimized single-atom calculations predicts the possibility to generate 55 as long SAP (see Figure III.21). We observe a broad emission between -1.0 and 0.2 fs, and there is also a narrower emission around 0.5 fs emitted in the next half-cycle, however this is eliminated from the temporal picture by spectral filtering. The optimization procedure indicated 118 eV to 195 eV bandwidth for the shortest single pulse production and an average GDD of 1460 as^2. The spectrally filtered radiation transformed to the time domain (part c) indicates 51 as pulses when the Lewenstein integral is limited to include short trajectories only. The unlimited integral affects slightly the duration of the pulse (55 as) and produces a second peak corresponding to long trajectories cf. time-frequency map. Macroscopic calculations predicts slightly longer 72 as pulse duration with the same generating field, when radiation with >1 mrad divergence is filtered out from the harmonic beam (Figure III.21(d)). We add here, that the 73 as pulses generated by the constant spectral phase driving field (cosine shape) would stretch to a 106 as length by propagation, and is narrowed to 95 as by spatial

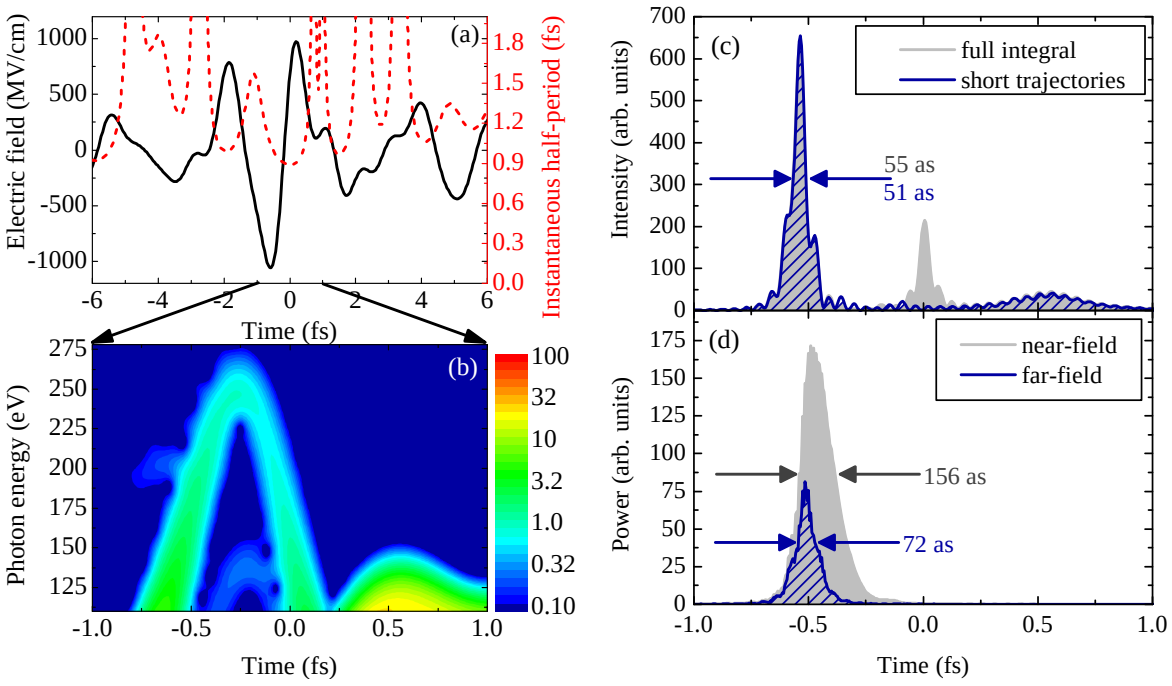

Figure III.21: *Generation of short, isolated attosecond pulses. (a) Driver electric field and instantaneous half-period. (b) Time-frequency map of the generated dipole radiation from the full Lewenstein integral shows the presence of the two trajectory components, which results in the two pulses in the (c) single-atom calculations. (d) Macroscopic effects however eliminate the second pulse, and spatial filtering also makes the remaining one shorter. Harmonics between 118 and 195 eV are used here for the generation of the attosecond pulse.*

filtering.

The other criterion used in this optimization, to have a SAP with a minimum contrast ratio of 1:10 (that is, suppressing the side pulses), is also fulfilled and improved in the macroscopic results. We see that the contribution of long trajectories and the second side-pulse is already eliminated by the end of the gas cell, but the spatial filtering is required to shorten the pulse in the far-field. We find that the improved phase-locking – achieved by filtering out harmonics generated off-axis [189] – is responsible for the shortening of the pulse from the 156 as in the near-field to the 72 as measurable in the far-field. The pulse durations quoted in this section are as-generated values, i.e. not using any postcompression method. Alternatively, a different optimization procedure can be carried out when postcompression is also available and the inherent chirp is not limiting the achievable pulse duration.

III.3.3 Double attosecond pulses with variable separation

The generation of double attosecond pulses (DAP) with variable separation on the multi-femtosecond scale has been predicted to be realizable using multi-cycle driver pulses and polarization gating technique [190]. Normally the natural separation of pulses in an attosecond pulse train is rooted in the half-cycle periodicity of the process: 1.3 fs pulse

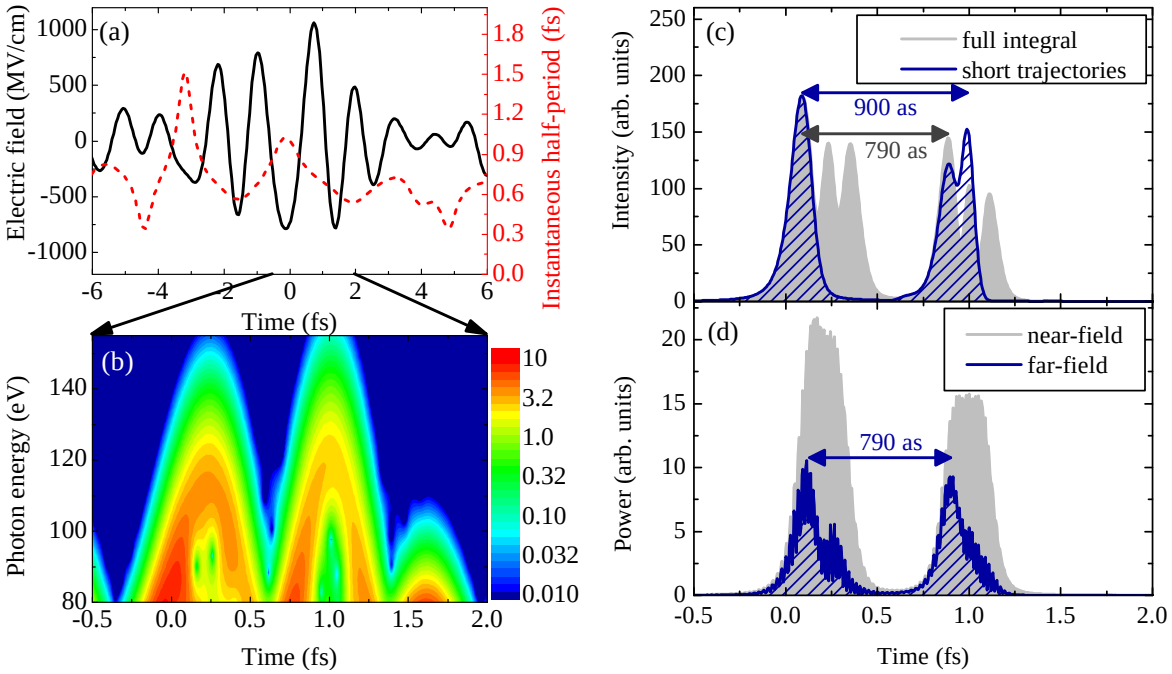

Figure III.22: *Double pulse, with 900 as separation. (a) The electric field and instantaneous half-period calculated from the phase derivative shows the complex structure of the driving field. (b) Time-frequency analysis showing the two pulses created in different half-cycles. Suppressing harmonics below 81 eV produces the two pulses which are present both in (c) single atom and (d) macroscopic results.*

separation for the 800 nm fundamental. Here we focus on producing DAPs with sub-femtosecond separation: aiming at equally intense pulses with different separation between them. The results of the optimization process are illustrated in figures III.22–III.24 in the same manner as Figure III.21.

For 900 and 700 as separations (Figure III.22 and Figure III.23) single atom calculations yielded the required pulse structure, and the results were also confirmed by macroscopic calculations, although the separation of the pulses is slightly smaller and their amplitudes are slightly different in the macroscopic response for both cases. Our analysis shows that for both cases the two pulses are produced by short trajectory components in different half-cycles of the generating driver field. We also see, that the instantaneous half period of the generating fields (calculated as $\pi/|d\varphi_1/dt|$) varies between 900 as and 600 as in the interval where the production (ionization – free travel – recombination of the electrons) of the attosecond pulses takes place. Since the electron travel responsible for the generation takes up about half a laser cycle, we cannot directly link the instantaneous period to the separation of the pulses.

In case of DAP with 700 as separation, the generating field's spectral centre of mass is at 416 nm, meaning that the half-cycles of the driver field follow each-other by ≈700 as. From this case we could think that by simply tuning the spectral centre of mass of the driver field generates attosecond pulse with the required separation. However in case of DAP with 900 as separation central wavelength of the generating pulse is at 423 nm

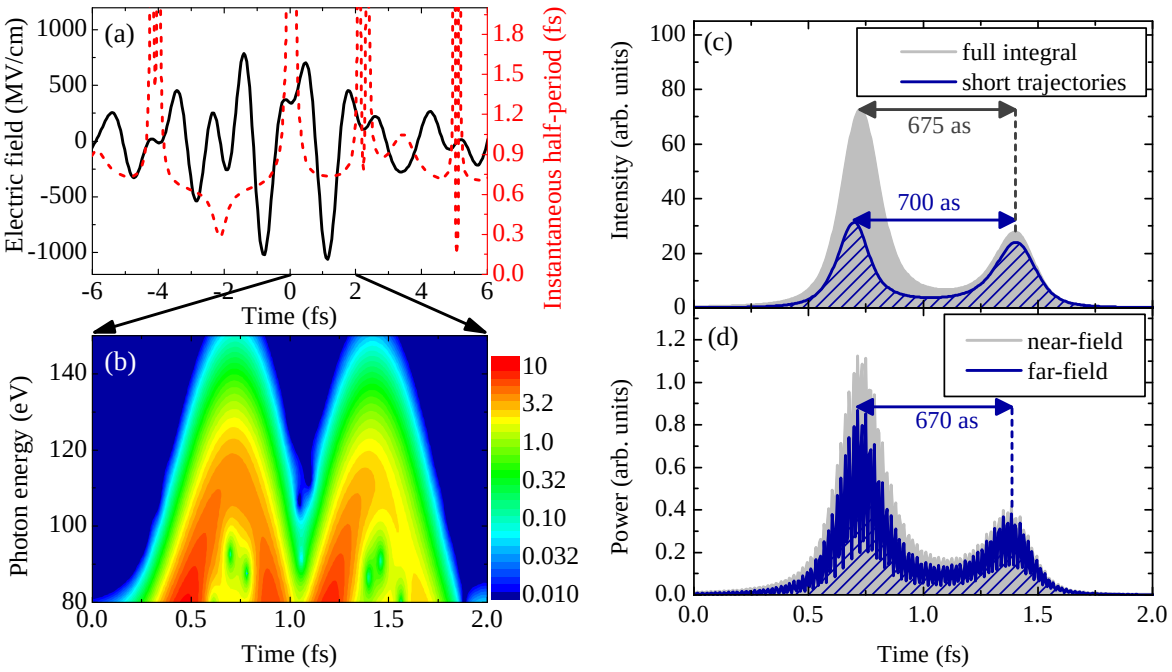

Figure III.23: *Double pulse, with 700 as separation. (a) Generating electric field and instantaneous half-period. (b) Time-frequency analysis showing the two pulses created in different half-cycles. Spectral selection from 108 to 170 eV produces the two pulses which are present both in (c) single atom and (d) macroscopic results.*

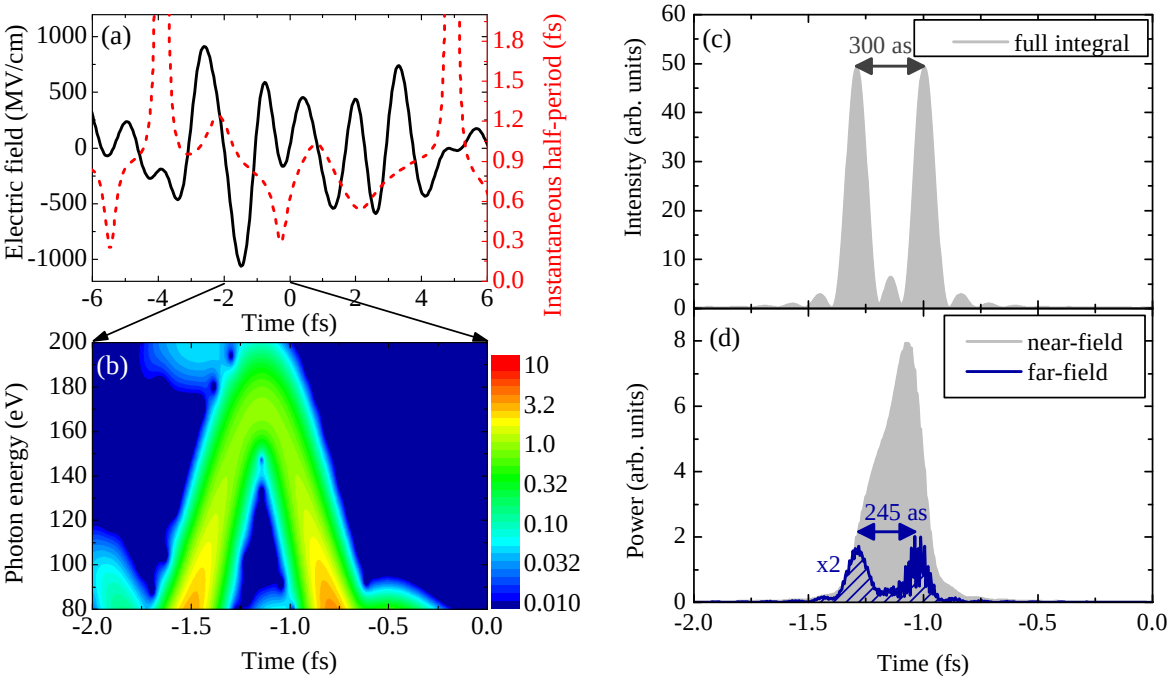

Figure III.24: *Double pulse, with 300 as separation. (a) Generating electric field and instantaneous half-period. (b) Time-frequency analysis showing the two pulses created in the same half-cycle by short and long trajectories. Spectral selection (from 130 to 166 eV) produces the two pulses in (c) the single-atom calculations, which merge in (d) the near-field, but are again separated in the far field by spatial filtering of the harmonic beam.*

(corresponding to 705 as half-cycle periodicity). In both cases it can be seen that the half-cycle periodicity of the laser pulse is changing in a sub-cycle level. This illustrates us that the desired results are produced by nontrivial field shapes, and these subcycle variations of the driving pulse are important.

On the other hand, we found that the generation of attosecond double pulses with less separation can be performed in a fundamentally different manner. When optimizing the driver wave for attosecond pulse production with 300 as distance, we ended up with two trajectory sets emitting harmonics in the same half-cycle (Figure III.24). Thus the separation between pulses is defined by the time-delay between returning electrons from short and long trajectories, and the main role of field-shaping is to ensure that only a single half-cycle contributes to the selected part of the spectrum.

In this case the two pulses merge in the near-field, and spatial filtering is essential to separate them. This also means that a large part (90%) of the pulse energy is filtered out. In this configuration, the fact that a lower pressure has been used – in this configuration favouring phase-matching of long trajectory components – also helps to keep both pulses in the far field with comparable peak power.

It is seen that short (300 as) and long (700 and 900 as) separation of the attosecond pulses was feasible via different schemes. With the spectral components for the driver laser field shown in Figure III.19, the algorithm produces double attosecond pulses with larger than 670 as separation from two different half-cycles of the driver laser pulse. We find that shorter separations are possible only from short and long trajectory components of harmonic radiation generated in the same half-cycle.

III.3.4 Summary

A genetic algorithm was used to optimize gas HHG in a modelled multivariable light field synthesizer device.

- **T3.a I have worked out a model suitable for further optimization, which is based on the single atom response calculation with limited temporal integration. I have shown with macroscopic HHG modelling that the Lewenstein integral is able to partially predict a good approximation of the macroscopic behaviour of the attosecond pulse generation process. I have interpreted the two distinct ways (consecutive half-cycle or short and long trajectory radiation in a single half-cycle generation) of the double attosecond pulse generation.**

- **T3.b I have modelled attosecond pulse generation by the selected driver waveforms with a 3D macroscopic model and shown that the pulse shortening achieved by the optimization remains robust in a macroscopic environment. I have also shown that in case of Gaussian generating beams,**

tight spatial filtering of the harmonic beam is required for the pulse duration to come close to the ones obtained in the optimization. Moreover, I predict that double attosecond pulses generated from short and long trajectories are only reproducible macroscopically in very inefficient generating conditions.

III.4 Quasi-phase matching by low-intensity assisting fields

So far we have analysed possibilities of generating attosecond pulses by combining field with different wavelengths. These combinations were used to control electron trajectories, and in subsection III.2.3 we have seen that – due to the sensitive nature of the harmonic phase to the shape of the generating field – they are also able to control macroscopic processes when a phase-slip between the two fields arises during propagation. In subsection II.4.5 we have seen that this can be exploited to induce QPM of generated harmonic radiation by weak assisting fields for example by a counterpropagating quasi-monochromatic field. We have seen that such an assisting field causes a modulation of the harmonic phase. This phase-modulation resembles the shape of the assisting field in the moving frame of the generating laser field. Some of the details of the process are still not clarified, and in this section we analyse this mechanism in detail. In particular we discuss the relationship between the amplitude of the assisting field (E_a) and that of the phase-modulation (A), the bandwidth of the QPM processes, and optimal profile of the assisting field.

III.4.1 Phase-modulation caused by weak assisting fields

We analyse the situation of a generating driver and a weak assisting field propagating in another direction. As seen earlier the phase-modulation of the generated harmonics can be expressed as $A = \zeta E_a$, where ζ is a scaling factor that relates the assisting field amplitude to the phase modulation amplitude. Using assisting fields of the same wavelength as the driver ($\lambda_a = \lambda_1$) the induced phase-modulation can be expressed analytically. Two separate contributions of the interference to the harmonic phase can be identified: a *direct* one caused by the phase-modulation of the driver field, and an *indirect* contribution, caused by the intensity modulation [115, 65], see Appendix C for more details. In the limit of $E_a \ll E_1$ the amplitude of the direct phase-modulation for harmonic q, caused by the driver field's phase-modulation can be expressed as [65]:

$$\Delta\varphi_p \approx q\frac{E_a}{E_1}. \tag{III.1}$$

The indirect phase-modulation can be linked to the intensity-dependence of the harmonic's phase, quantified by the α coefficient. Thus the harmonic's indirect phase modulation caused by the modulated driver intensity can be approximated as

$$\Delta\varphi_I \approx \frac{-\alpha e^2 E_1 E_a}{2m_e \hbar \omega_1^3} = \frac{-\alpha 2U_p}{\hbar\omega_1}\frac{E_a}{E_1}. \tag{III.2}$$

The maxima of the two – direct and indirect – components of the phase-shift occurs shifted by $\pi/2$ in phase difference between the two interfering fields, as illustrated in Figure III.25. For the analytic derivation see Appendix C. Due to this delay, the total

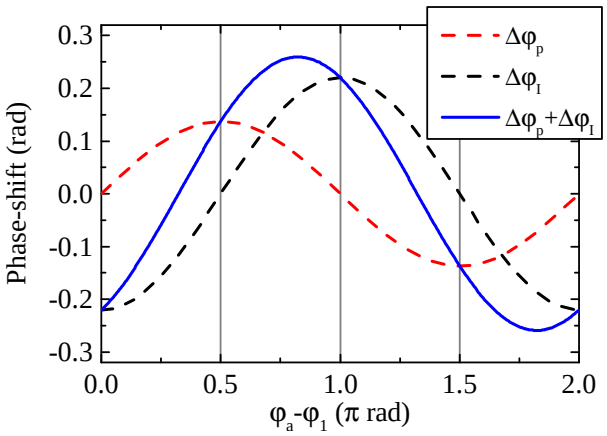

Figure III.25: *Direct and indirect harmonic phase-modulation caused by interfering driver and assisting waves, shown as a function of the phase difference between the two fields. More details in [115, 65] and Appendix C.*

phase-modulation can be calculated simply as

$$A_1 = \sqrt{\Delta\varphi_I^2 + \Delta\varphi_p^2}. \tag{III.3}$$

From the above equation, the scaling factor ζ between the assisting field strength and the phase-shifting effect (of Equation II.41) for cases when the assisting and driver fields have the same wavelength can be expressed as

$$\zeta_1 = \sqrt{\left(\frac{q}{E_1}\right)^2 + \left(\frac{\alpha 2U_p}{\hbar\omega_1 E_1}\right)^2}. \tag{III.4}$$

For cutoff harmonics it is known that $q = (1.32I_p + 3.2U_p)/\hbar\omega_1$ and $\alpha \approx \pi$, therefore, in cases when $I_p \ll U_p$, the scaling factor becomes

$$\zeta_1^{cutoff} \approx \frac{7U_p}{\hbar\omega_1 E_1} \propto E_1\lambda_1^3. \tag{III.5}$$

We observe that for cutoff harmonics where QPM methods are found to be most effective the required field strength scales inversely with the driving field strength and the third

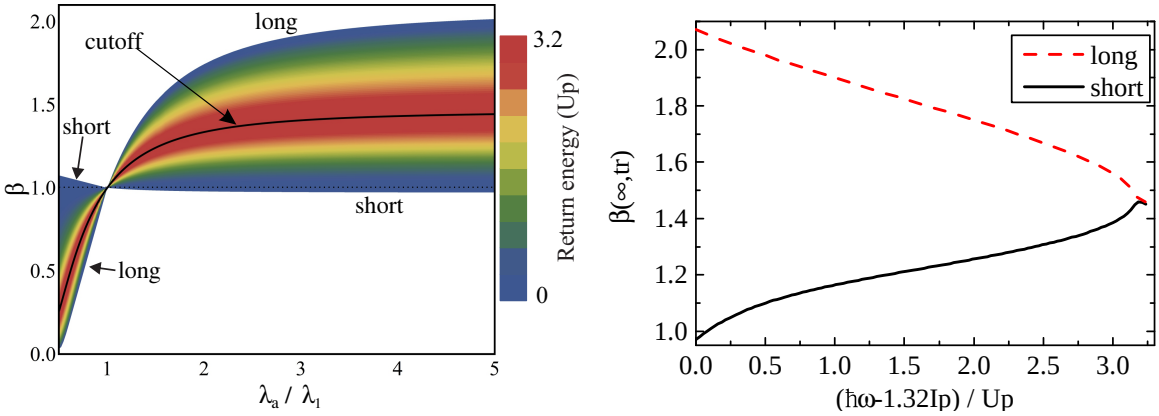

Figure III.26: *Phase-modulation coefficients for arbitrary wavelength assisting fields. (a) shows the coefficients up to assisting wavelengths* $5\lambda_1$*, while (b) is accurate for longer wavelengths and DC fields. In (a) trajectory lengths are shown in colour scale represented by their final kinetic energy in units of* U_p*.*

power of its wavelength

$$E_a^{cutoff} = \frac{A}{\zeta} \propto E_1^{-1}\lambda_1^{-3}. \tag{III.6}$$

As the cutoff energy in HHG scales as $E^2 \cdot \lambda^2$, the same energy photons still require weaker assisting fields when generated by weaker, but longer wavelength driver fields.

With an assisting field of arbitrary wavelength we rely on numerical calculations to obtain the same information. In this case the direct and indirect modulation cannot be separated so easily, so we compare the amplitude of the total phase-modulation caused by an arbitrary wavelength assisting field to the case when the two wavelengths are the same (ζ_1). We calculate the harmonic phase-modulation amplitude (using the saddle-point approximation for the combined driver and assisting field), by varying the phase-difference between the two fields in small steps in a 2π interval. We do this procedure for assisting fields with different wavelengths and compare the results to the case when the two wavelengths are the same. Thus, we relate the phase-shifting effect of arbitrary wavelength assisting fields (ζ) to the same-wavelength case (ζ_1) by a correction factor

$$\zeta = \zeta_1 \beta(\lambda_a/\lambda_1, tr), \tag{III.7}$$

where tr distinguishes trajectories with different return time, and λ_a/λ_1 is the ratio of the two wavelengths. The value of $\beta(\lambda_a/\lambda_1, tr)$ is shown in Figure III.26.a.

By definition of the parameters, at $\lambda_a = \lambda_1$ all the trajectory dependence of the phase shift is included in ζ_1. It is interesting to see how the correction factor for short and long trajectory components cross at this point. For all values of $\lambda_a > \lambda_1$ we observe that the value of the correction factor is almost constantly 1 for the shortest trajectories, and for the longest trajectories the deviation from 1 has the largest magnitude. This finding is consistent with the simple view, that the longer the electron stays in the continuum, the more sensitive it becomes of the effect of the assisting field [89]. In the limit when

$\lambda_a \gg \lambda_1$ (i.e. when the assisting field can be considered static during the electron's travel in the continuum), the value of the β correction factor goes to 1.45 for cutoff harmonics. For other trajectories this factor varies as shown in Figure III.26.b, being very close to one in case of the shortest trajectories and going slightly higher than two for trajectories with a return time of one optical cycle. The values of β calculated for DC fields (in Figure III.26.b) are accurate for assisting fields with $\lambda_a > 5\lambda_1$.

The figure also indicates, that for $\lambda_a < \lambda_1$ the dependence of the correction factor on trajectory length is reversed; the longer the trajectory, the less the effect – which can be understood as the perturbation caused by the assisting field can average out through the longer travelling time of the electron. This means that in this regime the relative effect of the assisting field on shorter trajectories becomes more and more pronounced. We would like to point out the practicality of this limit: since the assisting field's wavelength is determined by the coherence length, and L_c scales inversely with harmonic order [93], it might reach very small values when increasing driver wavelengths are applied to generate very high harmonics in the x-ray region [191, 151]. In this scenario under very unfavourable PM conditions short wavelength assisting fields might be useful in achieving QPM.

We performed calculations with different laser field and ionization potential parameters, all yielding very similar results to what is shown in Figure III.26, only finding small deviations from it. The results are found to be more accurate in the high-intensity regime, where $U_p > I_p$.

Finally, combining equations II.40, III.4 and III.7, the formula for the strength of the assisting field causing the required A phase-modulation for harmonic order q can be expressed as

$$E_a = \frac{AE_1}{\beta\sqrt{q^2 + \left(\frac{2\alpha U_p}{\hbar\omega_1}\right)^2}}, \tag{III.8}$$

the value of β depending on the ratio of the driver and assisting fields wavelength, and shown in Figure III.26.

We note here, that the wavelength of the assisting field, λ_a is not a free choice, it is determined by the coherence length. This implies, that the correction factor β has only an indirect dependence on the generating laser pulse parameters through the coherence length, and depends directly only on the chosen trajectory, thus the scaling law expressed in Equation III.6 holds generally. We note that our model is obviously not applicable to the cases when the assisting field alone causes photo-ionization, replacing the role of tunnelling ionization in the three-step model of HHG.

III.4.2 Quasi-phase-matching bandwidth

There are two main contributions limiting the bandwidth of effective QPM with assisting periodic fields: one concerns the chosen period, the other the amplitude of the assisting

field. The phase-shift induced by the assisting field is different for different harmonics due to the indirect phase-modulation: thus the amplitude of the required assisting field, as presented in the previous section, depends on the harmonic order through α and also β when the assisting wavelength is different from the driver. The period, set by the coherence length shows an even stronger dependence on harmonic order. By applying a single period, the bandwidth over which QPM can be achieved depends on the variation of the coherence length, and it decreases with the length of the gas cell. In the present section we only discuss in detail the bandwidth of QPM achieved with an assisting DC or sinusoidal fields to simplify calculations. Since in most cases we expect the bandwidth to be limited by the spectral variation of the wavevector mismatch, these results can be considered to be relevant for all cases.

It is known from nonlinear optics that the efficiency of a QPM method strongly depends on the difference between the coherence length and the spatial periodicity of the phase-modulation. To describe this dependence, we denote a wavenumber-like quantity defining the value of PMM by $k_{PMM} = 2\pi/L_c$, and the wavenumber of the phase-modulation caused by the assisting field by $k_{mod} = 2\pi/\Lambda$. Then a wavenumber mismatch between the two quantities can be defined as $\Delta k_{QPM} = k_{PMM} - k_{mod}$. In a similar way to QPM in second-harmonic generation, we find that Δk_{QPM} in HHG has the same role as the wavenumber mismatch in standard nonlinear optics [30], and the harmonic intensity at the end of a cell with length L (when $L \gg L_c$) is given by

$$I_{prop}(L) \propto L^2 sinc^2\left(\frac{\Delta k_{QPM} L}{2}\right), \tag{III.9}$$

showing that the efficiency drops to half of the maximum value at $\Delta k_{QPM} = \pm 2.78/L$. Using the equation above, the overall efficiency of the QPM processes as a function of the wavenumber mismatch (Δk_{QPM}) and amplitude of the phase-modulation (A), for the cases when the applied electric field is static or sinusoidal, are given by:

$$\eta_{DC} = \sum_{m=1,3,5...} \left[\frac{2}{m\pi} sin\left(\frac{A}{2}\right) sinc\left(\frac{L}{2}\left(m\Delta k_{QPM} - (m-1)k_{PMM}\right)\right)\right]^2, \tag{III.10}$$

$$\eta_{sin} = \sum_{m=1,2,3...} \left[J_m(A) sinc\left(\frac{L}{2}\left(m\Delta k_{QPM} - (m-1)k_{PMM}\right)\right)\right]^2, \tag{III.11}$$

where $J_m(A)$ is the mth order Bessel function of the first kind, and by summation over m we considered the contribution of higher-order spatial QPM. In most cases higher orders can be neglected, eliminating the summation and also the second part of the *sinc* function, simplifying the formulae. Also in the case of the DC assisting field even order QPM is only achievable with different field distributions than odd order QPM [113], hence they do not appear simultaneously.

For a case study we use the 1D model presented earlier and calculate the values of the emission rate $h_q(z)$ and phase $\varphi_q(z)$ using the saddle-point approximation. For

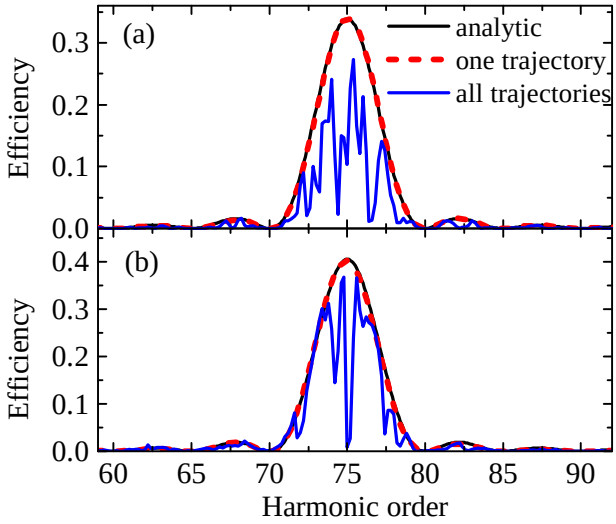

Figure III.27: *Efficiency of QPM in a 2mm long cell with sinusoidal (a) and DC (b) assisting fields optimized to the short trajectories at harmonic* 75*.*

these calculations we took an 8 fs long, 800 nm cos^2-shaped laser pulse with constant 8×10^{14} W/cm^2 intensity along z, that propagates with the same phase and group velocities (to eliminate the effect of carrier-to-envelope phase-shift). We chose a phase velocity higher than that of the harmonic q that causes a phase slip of $q2\pi/0.01$. This produces a coherence length of $L_c = 133$ µm for harmonic 75, which is in the plateau region of the spectrum, the cutoff being at harmonic 115. Then, we added a sinusoidal assisting field matching this coherence length and having an amplitude of 12.8 MV/cm calculated from Equation III.8 to produce optimal phase-shift for short trajectories at this harmonic order. Then, we calculated the efficiency of the QPM method at $L = 2$ mm by Equation II.41 for the whole spectrum. The efficiency was calculated considering only a single set of short trajectories from the middle of the pulse (red dashed line in Figure III.27), and all the trajectories throughout the pulse which are shorter than one optical cycle (thick blue continuous line in Figure III.27), and we compared with the analytical formula (thin black continuous line in Figure III.27).

We observe that trajectory interferences can be significant in QPM methods, especially for sinusoidal modulation, but the general shape is well described by the analytical formulae. We note that the phase-shift imposed by the assisting field for harmonics generated in opposite half-cycles of the driving field has opposite sign. With multi-cycle driving pulses this can lead to the elimination of odd harmonics and the coherent addition of even ones when a periodic static field is used producing a phase-shift of $A = \pm\pi/2$. This is discussed in detail by Diskin and Cohen [192].

As apparent from equations III.10 and III.11 the drop in efficiency with changing harmonic order can have two sources:

First, the field optimized for harmonic 75 causes different phase shifts (A) for different trajectories resulting in a drop in efficiency due to the $sin^2(A/2)$ and $J_1^2(A)$ dependencies seen in equations III.10 and III.11 respectively. The contribution to efficiency arising

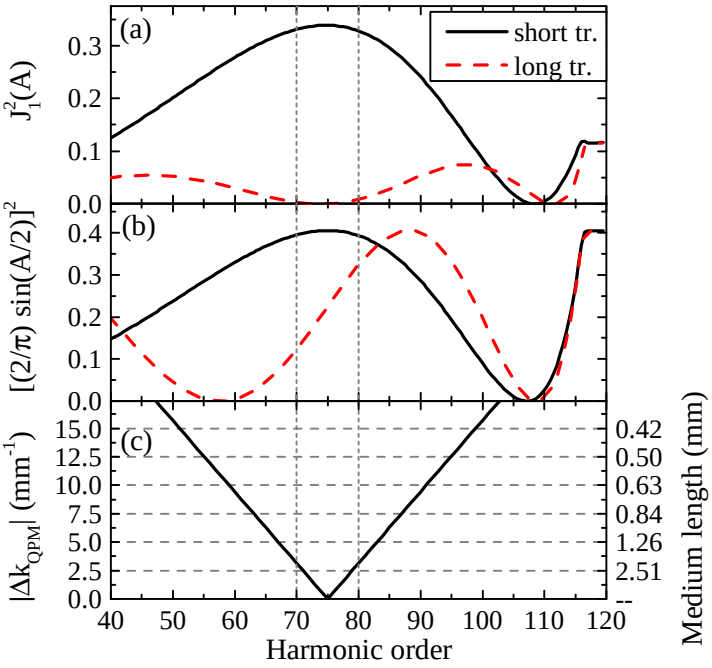

Figure III.28: *(a) and (b) illustrate the efficiency of QPM methods for different harmonics arising from the phase-shift caused by the assisting field optimized for harmonic 75 of the short trajectory. Efficiency calculated for (a) sinusoidal assisting field with 12.8 MV/cm strength causing 1.85 rad phase-shift and (b) periodic static electric field with a 21.4 MV/cm strength causing π rad phase-shift for the selected trajectory. (c) illustrates the wavevector mismatch at different harmonic orders, the right scale showing the corresponding medium length where* $sinc^2(\Delta k_{QPM}L/2)$ *reaches its first minimum. The two grey vertical lines show this minimum for a 2 mm long cell.*

from the phase-modulation's shape and amplitude is plotted in Figure III.28(a) and (b), showing similar behaviour for sinusoidal and periodic static assisting fields around the selected trajectories. As is apparent, this contribution allows a much wider bandwidth than what is observed in Figure III.27 (note the different horizontal scales on Figure III.27 and Figure III.28). Therefore, we conclude that the bandwidth is limited by a different source.

The wavevector mismatch is also trajectory dependent, giving the second source of bandwidth limitation. In our case, when a constant intensity is assumed along the propagation axis, k_{PMM} scales linearly with the harmonic order. This results in a linearly increasing wavevector mismatch (Δk_{QPM}) away from the selected harmonic order, limiting the efficiency as $sinc^2(\Delta k_{QPM}L/2)$. The value of $|\Delta k_{QPM}|$ is common for both QPM methods analysed by us, and is illustrated in Figure III.28(c). As the bandwidth is inversely proportional to the length of the medium, the contribution from $|\Delta k_{QPM}|$ is the significant limiting factor in most cases except when QPM is applied over a medium just a few L_c long. In the particular case discussed here, after $3L_c$ (L=0.4 mm) the bandwidth arising from the wavevector mismatch is already slightly smaller than the one arising from the phase-shift dependence (efficiency dropping to 0 at harmonic 100), and it is quickly becoming the main limiting factor when increasing the length of the medium. As a con-

sequence, for the 2 mm long medium ($L = 15L_c$) used to calculate Figure III.27, the envelope of the efficiency curve resembles the bandwidth limited only by the wavevector mismatch, without significant differences due to the different shape of the assisting field.

Figure III.28(a) and (b) also illustrate that the assisting field optimized for short trajectories is usually not optimal for long ones at the same harmonic order. Although in special cases, higher order (in amplitude) QPM of long trajectories can be obtained, possibly increasing the efficiency for both trajectory classes. This, however, is only achievable if both the phase-shift and Δk_{QPM} is optimal at the same time.

If one considers a more realistic case where the phase-velocity and/or driver intensity is also changing along the propagation axis, then the coherence length also becomes dependent on z and chirped assisting fields should be used for optimal QPM [117, 5].

III.4.3 Assisting beam profile

In order to induce QPM in a macroscopic media the phase-shifting effect of the assisting field for a given harmonic has to be the same at different spatial coordinates across the beam. However, due to the intensity profile across the beam the same harmonic order falls at different parts of the plateau and thus has an α and β value varying with the radial coordinate. Both of these affect the phase-shifting effect of the assisting field. To compensate this, the assisting field must have an appropriate spatial profile. For the short trajectories lower IR intensity (off-axis) means that the same harmonic is closer to the cutoff, has both higher α and higher β values, therefore the required assisting field strength is lower. The opposite stands for long trajectories, where α and β decreases with intensity. This issue is not raised for cutoff harmonics which are only generated close to the axis.

Assuming that the generating laser beam has a Gaussian spatial profile, the intensity profile of the assisting field can be determined. In Figure III.29 the calculated intensity profile is shown for different harmonics generated by 800 nm driving field for the case when A=π radian, and $\lambda_a \gg \lambda_1$.

The intensity profile required by QPM (Figure III.29) for short trajectories closely resembles a Gaussian suggesting that counterpropagating fields may be used to induce QPM in the whole cross section of the gas cell. As for long trajectories the required field intensity is higher off-axis, which could be an explanation why the most efficient QPM was found for harmonics close to the cutoff [87, 5]. Another important aspect of Figure III.29 is that for long trajectories the required field strength is two orders of magnitude lower and almost constant for different harmonics (close to the axis), while for short trajectories it shows high variation with harmonic order (a result consistent with the findings of Zhang et al. [88]). Thus spectral selection might be easier to achieve for short trajectories by varying the strength of the assisting field.

However, in case of counterpropagating pulse trains, the only constraint for (partial) elimination of harmonic emission from destructive zones is that the phase-shift should be

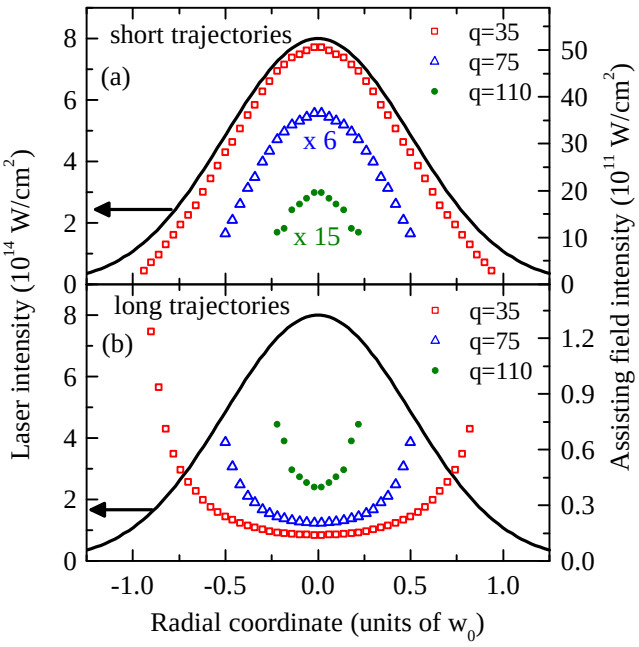

Figure III.29: *Numerically calculated radial intensity profiles needed to induce π phase-shift for different plateau harmonics, when generated by a Gaussian beam having a beam radius of w_0. Calculations done for $\lambda_1 = 800$ nm driving field, and long wavelength assisting fields $\lambda_a \gg \lambda_1$.*

larger than π. In this respect short trajectories dominate the selection of the field strength, since those always require higher intensity assisting field for the same phase-shift. This is also consistent with the findings of O'Keeffe et al. [65].

III.4.4 Summary

- **T4.a I have described a method to calculate the phase-modulation of harmonics by a weak assisting field in terms of the generating laser pulse's parameters, depending on the two fields' relative wavelength and the length of the electron trajectory in question. I have discussed the relationship between the simplest case of a counter-propagating, same wavelength assisting field (analytical treatment), to the case when a different wavelength assisting field is used, and showed that the two can be related through a wavelength-dependent correction factor.**

- **T4.b I have analysed the bandwidth of QPM methods and formulated an approximate expression to calculate it. I have shown that the dependence of phase-modulation amplitude on the harmonic order is not limiting the QPM bandwidth significantly when the method is applied to a large number of coherence periods. Therefore, in these cases the bandwidth does not depend on the shape of the applied assisting field. On the other hand, I have shown that trajectory interferences can significantly change the fine-structure of the QPM efficiency. I have also discussed**

the optimal field profile of assisting fields for short and long trajectory components for efficient QPM, and I have found that short trajectories have the advantage of requiring the same profile for driver and assisting beams.

III.5 Quasi-phase matching by perpendicularly propagating THz fields

So far we have seen that the presence of a spatially modulated electric field along the propagation axis of the generating laser field is able to modulate the phase of the generated harmonics and create suitable conditions for QPM. In this section we present numerical calculations where we apply this idea and show that THz pulses can be used to realize conditions of efficient HHG at photon energies above the phase matching limit. We test the use of perpendicularly propagating IR and THz pulses to produce the required modulation Figure III.30.

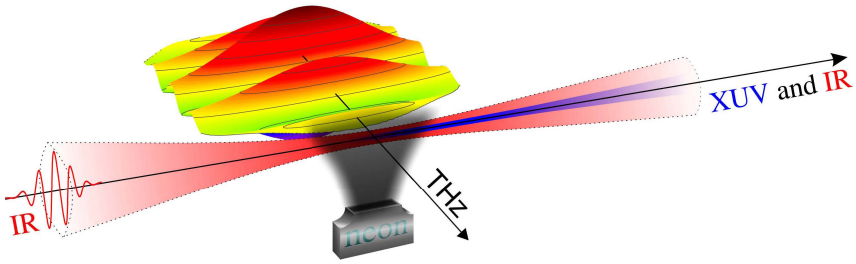

Figure III.30: *Schematic representation of HHG by perpendicularly propagating IR and THz fields.*

III.5.1 Possible configurations

We aim at creating a spatially periodic electric field along the propagation axis while the IR field passes through the cell. In the configuration sketched in Figure III.30 as the IR pulse propagates, at different position it meets different phases of the THz pulse therefore "feeling" different field strengths. To illustrate the effect, we plot the THz field in the moving frame of the IR pulse at t=0 i.e. at the peak of the IR pulse (Figure III.31). In cases when the cell is illuminated by one THz pulse from the side, the IR feels a periodic electric field, however the phase front is tilted (Figure III.31.a).

One-dimensional analytical and numerical calculations shows that the efficiency of QPM is not affected by a phase shift of the assisting field as long as the number of coherence lengths covered is large enough. On the other hand, under QPM conditions the propagated harmonic field's phase converges to a value that is dependent on the initial phase of the assisting field. This, together with the apparently tilted phase-front of the

THz field might alter the propagation direction of the harmonic beam, although we have not analysed the importance of this effect using three-dimensional calculations.

To eliminate this possible issue, two counter-propagating THz pulses (both hitting the gas cell from the side) can be used to create a standing wave, which produces a periodic electric field (Figure III.31.b). This configuration has the advantage of requiring half the energy in the THz beams to reach the same amplitude. The fact that the nodes of the standing wave are at $\lambda/4$ distance from the middle of the cell limits the width of the region where QPM is achieved.

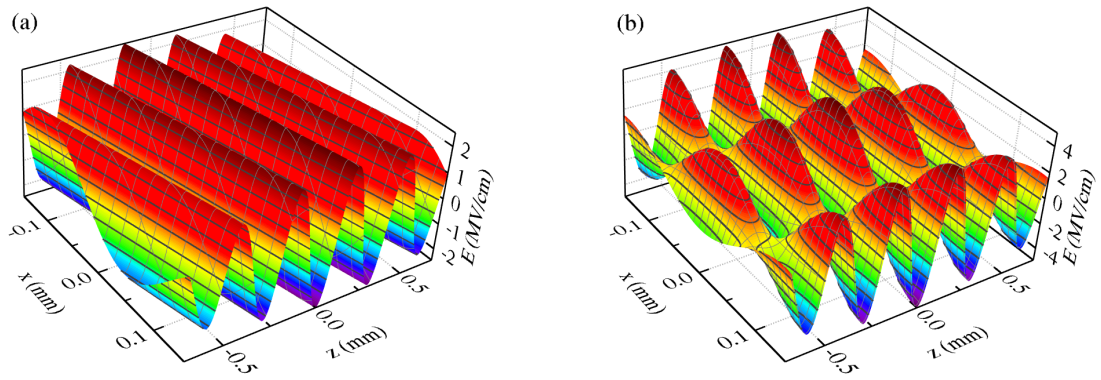

Figure III.31: *THz fields hitting the side of the gas cell as viewed from a coordinate frame moving with an IR pulse which is propagating in the direction of increasing z. The amplitudes are plotted in the plane of the two propagation axes. In (a) one THz pulse is focused into the cell, whereas in (b) two pulses hit the cell from opposite direction creating a standing wave along the width of the cell (in x direction).*

In these configurations the width of the THz beam has to cover the whole length of the cell and the pulse also has to be long enough to be present while the IR passes through. In theory the energy requirement due to the large beam diameter can be reduced by cylindrical focusing, and the necessary duration of the pulse can also be reduced by tilting the pulse front.

The width of the THz beam in both directions might be reduced in a configuration where the THz field is counter-propagating to the IR. This configuration also eliminates the possible issue of the tilted phase fronts or that of the reduced area between nodes of standing waves. In this case the wavelength has to be doubled to create the same periodicity felt by the IR pulse. The length of the gas cell in this configuration is limited by the Rayleigh length of the THz beam and by the length of the pulse, which also has to be doubled.

In our numerical 3D model we use cylindrical symmetry and a moving frame of reference, hence we cannot properly account for all the focusing and propagation effects of the assisting field. Due to this, we set the goal to test the proof of principle that a periodic, sinusoidal field in the THz range can induce QPM in a macroscopic medium. In our model we use the perpendicularly propagating scheme (Figure III.30) to calculate the value of the field strength on-axis, however, we assume this field strength to be uniform along the

radial direction. As we will see, this is a good approximation in the region the model is tested, as the harmonics to be quasi-phase matched are only generated very close to the axis, in a region significantly narrower than the wavelength of the assisting field.

III.5.2 Finding THz pulse parameters

To test the idea we chose a tight focusing geometry and high-intensity IR pulses producing a relatively high ionization rate and generating harmonics above the phase matching limit. In particular we use 20 fs long, 0.2 mJ laser pulse with a central wavelength of 800 nm, which is focused into a gas cell containing neon at 33 mbar pressure. The beam has 25 µm waist radius, and it could, theoretically, reach a peak intensity of 9×10^{14} W/cm^2. The gas cell is 2 mm long and it is centred in the geometrical focus of the IR beam.

Due to nonlinear effects the peak intensity of the beam reaches only 8×10^{14} W/cm^2 and it decreases slowly after the focus. At this intensity the single-atom cutoff is around harmonic 111, which corresponds to 172 eV, well above the ≈120 eV phase matching limit available in waveguides [40, 41]. In the current free-focusing geometry phase-mismatch decreases the cutoff to harmonic 85 (130 eV) by the end of the 2 mm gas cell while harmonics above 70 are only phase-matched off axis. Our goal is to use the THz field to restore the single-atom cutoff in the near field by QPM.

First of all, we estimate the wavelength of the field to be used, that should correspond to the coherence length of the harmonic to be enhanced. As in free focusing there is no general description of phase matching, we cannot estimate the coherence length just from the intensity and gas pressure, and we rely on other methods in finding it. By plotting the intensity of the harmonic along the propagation axis, a good estimate can be given: the coherence length is twice the modulation period of the harmonic intensity. In Figure III.32.a we can also see that harmonic 111 is generated only close to the axis ($r < 7$ µm) and the periodicity of its intensity modulation stays constant over the radial coordinate.

For the THz field to cover the whole cell while the IR is passing through, we assume a beam with 4 mm waist size focused to the beginning of the cell (z = -1mm). The duration of the pulse is 8 ps, and is synchronised with the IR to reach its maximum when the IR is entering the cell.

Finally, we used the saddle-point approximation to find the optimal amplitude of the assisting field, but the approximations described in the previous section would have worked equally well. For our case the optimal value was found to be around 4 MV/cm, but due to temporal and spatial variations of amplitude in the focused pulse, we chose a peak amplitude of 5 MV/cm to be used in our model.

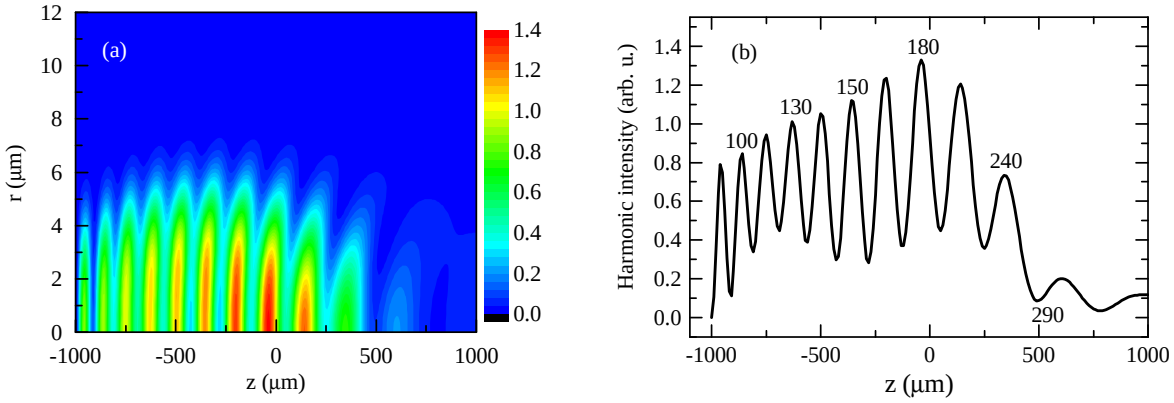

Figure III.32: *(a) Intensity map of harmonic 111 showing that the harmonic emission is confined to a small region around the axis, and the periodicity stays the same along the radial coordinate. Plotting the harmonic intensity along the propagation axis (b) the coherence length (indicated in μm) can be estimated.*

III.5.3 Enhancement of generation efficiency

In Figure III.32 it is obvious that the coherence length varies along propagation, and tuning the central wavelength of the pulse to match one region is not going to enhance the emission in the whole cell.

Nonetheless, illuminating the cell with a THz pulse having 120 μm wavelength still a significant increase in harmonic yield can be obtained (blue dotted line in Figure III.33). In this case the intensities at the end of the cell is 670 times higher than in the IR only case. Considering the peak harmonic intensity along the propagation axis, we get a 100 fold enhancement. Not surprisingly the region where the highest enhancement is produced corresponds to the region where the wavelength of the field best matches the intensity modulation of the harmonic in the IR-only case.

To match the spatially varying coherence length chirped pulses could be used. Using a pulse with 110 μm central wavelength and -9×10^{-7} fs^{-2} chirp rate to better match the varying coherence length a further increase in efficiency can be obtained, reaching 300 fold gain in the peak intensity of the radiation over the IR-only case (Figure III.33).

To show that the increased cutoff is indeed the result of QPM caused mainly by modulating the phase and not the emission rate, we use trajectory calculation to analyse the phases and intensity of the harmonic in question. The phase and intensity of the propagated IR field is used as input in a 1D model that uses the saddle-point approximation to calculate HOH emission along the propagation axis. Then the emissions are coherently summed to get the propagated harmonic intensity and phase at each point along the axis. The results are shown in Figure III.34. Despite using only one set of short-to-cutoff trajectories the main features of harmonic intensity increase are well reproduced by the 1D model. It can be seen that the phase difference stays in the constructive zone over longer regions, the main requirement for QPM by phase modulation.

In Figure III.35 we compare harmonic spectra on a logarithmic scale, obtained in

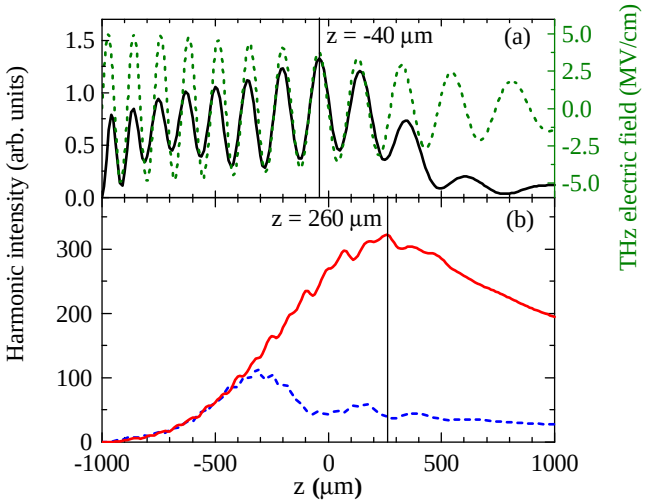

Figure III.33: *(a) Black solid line: THz-free variation of H111 intensity. Green dotted line: THz field showing the correspondence with the coherence length. (b) Red solid line: On-axis variation of the harmonic intensity along the propagation direction when a chirped THz pulse is applied. Blue dashed line: same when the THz pulse has constant 120 µm wavelength. Vertical lines indicate the positions of maximum harmonic yield.*

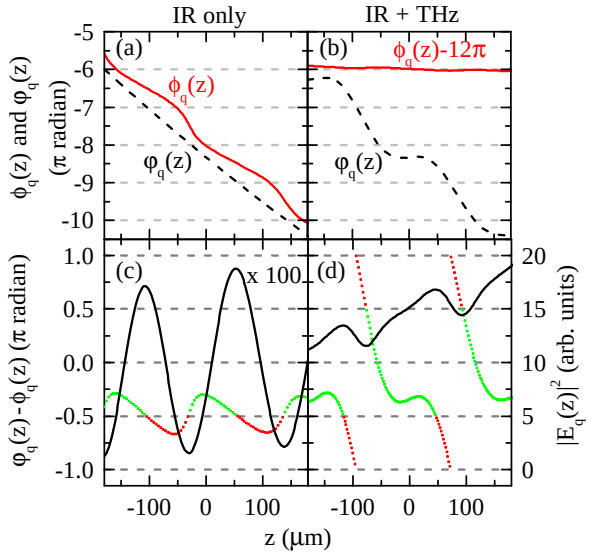

Figure III.34: *Variation of the H111 dipole phase and total harmonic phase without (a) and with THz field present (b). In (c) and (d) red/green dots show the phase difference between propagated and generated harmonics with scale on the left. Black line: harmonic intensity, scale on the right. (c) IR-only case; (d) THz-assisted case. Notations as used in section II.4.*

different conditions. The black line indicates the spectrum produced in a very thin (20 µm) target with the IR pulse alone, which gives us practically the single-atom spectrum, with the expected cutoff located at harmonic 111. The conversion efficiency is very low due to the short cell. The red line indicates the spectrum produced by the IR pulse recorded at the position in cell where we obtained the highest harmonic intensity, i.e., $z = -40$ µm [cf. Figure III.33]. We observe that harmonics in the lower plateau (below harmonic 70) experience an increase ($\approx 10^2$ times) with cell length, as more atoms contribute to the

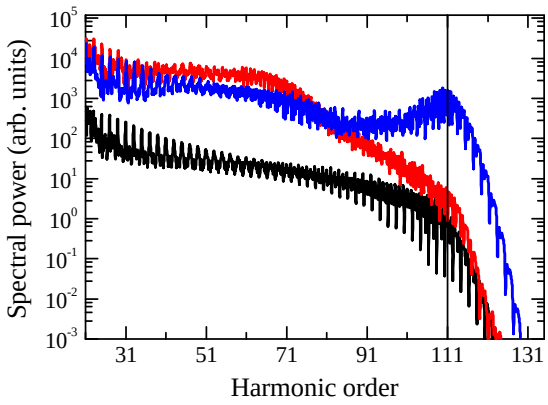

Figure III.35: *Logarithmic plot of HH spectra. Black (1): harmonic spectrum generated with IR-only after 20 μm propagation. Red (2): IR-only spectrum at the position of maximum harmonic intensity (z = -40 μm). Blue (3): spectrum obtained with THz-assisted HHG at the position of maximum harmonic intensity (z = +260 μm). THz pulse was linearly chirped such to best match the on-axis periodicity of harmonic 111. Vertical line: position of harmonic 111.*

HHG process, and apparently phase matching is favourable. For the higher plateau and cutoff harmonics we observe no significant yield enhancement with increasing cell length, which is explained by the phase-mismatch discussed in detail for harmonic 111.

The blue line depicts the spectrum obtained with the chirped THz pulse assisting the HHG process at the position in the cell where the harmonic intensity reaches its maximum (z = 260 μm). Since the THz parameters were chosen to optimize QPM for harmonic 111, the spectrum is enhanced in that range. For this harmonic we obtain ≈1060 times increase in the maximum harmonic yield after ≈1200 μm propagation compared to the yield after 20 μm. With perfect phase matching and constant emission rate the harmonic yield should have increased quadratically with propagation distance, resulting in a ≈3600 times enhancement. Our QPM method reaches almost 30% of this value while the emission rate is decreasing.

Finally we note that in the geometry sketched in Figure III.30 for the used THz field strength, duration and spot size, we would need 70 mJ THz pulse energy which is more than 2 orders of magnitude larger than available now in one-cycle THz pulses [193, 194]. However this can be significantly reduced by using other geometries, as described previously. Moreover, as shown in section III.4, for a specific photon energy the needed assisting field intensity scales with the wavelength of the generating field as λ^{-2}, reducing the needed assisting pulse energy when using MIR fields for harmonic generation.

III.5.4 Summary

We analysed the possibilities of using THz pulses to enhance harmonic generation efficiency in a phase-mismatched environment.

- **T4.c Using a 1D model I have predicted that HHG can be enhanced by perpendicularly propagating long-wavelength fields at photon energies**

above the phase-matching limit. I calculated the amplitude of the optimal THz field that was used in 3D numerical calculations which verified that these fields are able to induce QPM. In a case study, I have found an increase in efficiency of more than two orders of magnitude around the region of the single-atom cutoff. A chirped THz field, matching the coherence length of the generated harmonics was found to further increase the generation efficiency.

Legal notes

Parts of the text in this section and some of the figures have been taken over from "K. Kovacs et al., Phys. Rev. Lett. **108**, 193903, Copyright (2012) by the American Physical Society".

III.6 Pressure dependence of XUV group delay

So far we have presented results of numerical calculations proposing new ways to generate SAPs or enhance the efficiency of HHG and tried to explore the applicability of advanced laser tools in attosecond pulse generation. In this section we present an experimental study of macroscopic processes in attosecond pulse generation, by measuring the effect of generating gas pressure on the delay of attosecond pulse trains.

As described in section II.5 in RABITT the recorded signal of sideband $q+1$ can be expressed as

$$S(\tau, \omega_{q+1}) = C_1 + C_2 cos[2\omega_1(\tau + \tau^{at}_{q+1} + \tau_{q+1})], \tag{III.12}$$

where τ is the delay between the XUV and IR fields, τ_{q+1} is the attosecond group delay and τ^{at}_{q+1} is the atomic delay. Because the absolute value of τ is not known, the absolute value of τ_{q+1} cannot be extracted from a simple RABITT measurement, only its variation over the harmonic spectrum. However, if one manages to reproducibly stabilize τ between different RABITT measurements, then any variation of τ^{at}_{q+1} or τ_{q+1} can be measured with attosecond accuracy. To obtain the results presented here we used a stabilized interferometer for RABITT to measure the variation of XUV group delays τ_{q+1} as a function of gas pressure in the generation cell.

III.6.1 Experimental setup

These measurements were done at the Atomic Physics department of Lund Universitet. For harmonic generation we used 800 nm 30 fs long, 3 mJ laser pulses at 1 kHz repetition rate from a Titan:Sapphire laser with a two-stage amplifier system.

In the RABITT measurement the 800 nm pump beam is focused by a parabolic mirror (f=45 cm) into a 6 mm long cell, synchronously pumped with Argon gas at 1 kHz. The generated harmonic beam passes through a 200 nm thick aluminium filter to eliminate

the IR and low-order harmonics. Then it passes through a hole in the curved mirror which is used to recombine the XUV and probe IR beams. Both beams are refocused with a grazing incidence toroidal mirror (f=30 cm) into the target area of a magnetic bottle electron spectrometer, which redirects photoelectrons to micro-channel plate amplifying the signal. The detector of the MBES is also synchronized with the laser pulse, and the photoelectrons' time of flight from the target area to the detector (which fall into the several hundred ns time scale) can be used to separate electrons with different kinetic momentum. This allows the determination of the corresponding harmonic photon energies, as we have seen in subsection II.5.1. The delay between the pump and probe pulses can be varied using a piezoelectric translation stage.

To achieve attosecond stability of τ between consequent RABITT scans, we used an actively stabilized Mach–Zehnder interferometer as a basis for the RABITT setup as depicted in Figure III.36. In the pump arm of the interferometer, after the IR pulse

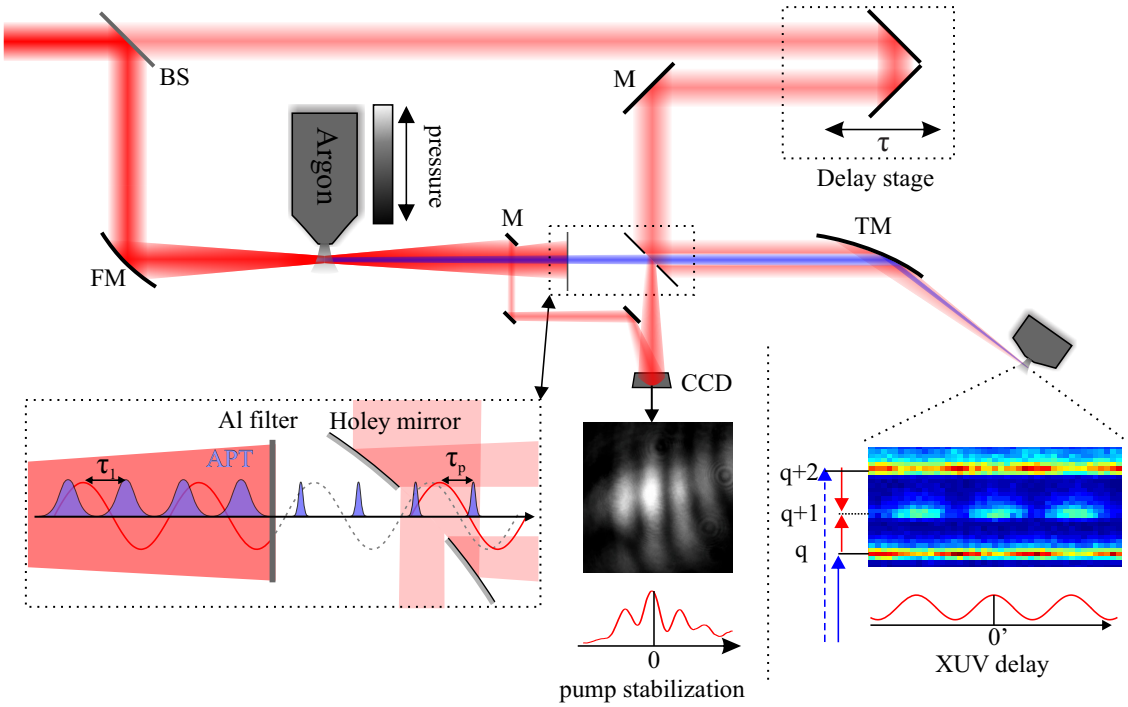

Figure III.36: *Scheme of the experimental setup. Details in the text.*

passes through the generation cell, a D-type mirror is used to redirect a small portion of the beam. In the probe arm we made use of the leak through the holey recombination mirror: the part of the probe beam that passes through this mirror is recombined with the redirected pump beam. With a slight angle between the two beams these produce spatial interference fringes along their cross-section, which move depending on the phase-delay between the fields. These fringes are recorded with a CCD camera for further analysis.

Selecting a part of the recorded image with clear interference structure and determining the phase by Fourier-transforming the modulation we were able to trace the slight fluctuations in the length of the interferometer. With active feedback these fluctuations could be compensated for in the delay stage of the probe arm. Tracing the movement of

the fringes during the RABITT scans, the delay between the two fields can be readjusted before a new RABITT scan, allowing the consequent recording of RABITT traces with the same τ, and the measurement of any variation of the other delays (τ_{at}^{q+1} or τ_{q+1}).

Using this method we assumed that the stabilization part of the interferometer, after the D-shaped and recombination mirror, is not a source of instability. To test this we did consequent RABITT scans with the same generating pressure and detection gas (i.e. keeping both τ^{at} and τ_{q+1} the same) and compared the measured sideband phases. We found that the sideband phases were slowly moving for about 1.5 hour after aligning the system, however good stability is achieved after this. The slow shifts in delay between the two arms were traced back to the heating of the recombination mirror by the laser beam, which stopped after the thermalisation of the system.

After stability has been achieved we did alternate scans with different gas pressures in the generation cell. We had no direct access to the gas pressure present in the generation cell, just to the background pressure in the vacuum chamber, therefore we could only estimate the real pressure in the cell, and we shall refer to the measured background values in the following. These values are of the order of a few µbar, while in the cell we estimate pressures around several tens of mbar.

It should be noted that the active stabilization locked the phase of the probe to the pump beam, after the latter passed through the gas cell, therefore compensating for any phase delay appearing in the generating chamber due to the changing propagation conditions. As a result the group delays we are measuring are relative to the generating IR pulse after the gas cell.

III.6.2 Measurement results

We have optimized the gas pressure for the highest XUV intensity (achieved at 2.5×10^{-3} mbar) and used RABITT scans taken at this pressure for reference. We have taken RABITT scans alternating the pressure between the reference value and other *target* values to analyse the effect of macroscopic processes on the group delay of attosecond pulses. As apparent in Figure III.37, a slow drift between pump and probe beams was still observable in the measurements, however it is much smaller than the targeted effect, and it is close to linear. To increase the accuracy we averaged the delays calculated from the two reference measurements, done before and after the measurement at the target pressure.

Since the absolute value of the delay between the XUV pump and IR probe beams in the measurement is still not known, we have chosen an arbitrary sideband delay as 0, and we present averaged group delay variations in Figure III.38. It is apparent that higher-order harmonics are delayed compared to lower orders, as expected from short-trajectory radiation (although these delays already incorporate the effect of the metallic foil and atomic delays). As seen in Figure III.38, when increasing the pressure in the generation cell, two things become apparent: 1) we reduce the GDD of the generated pulse (which

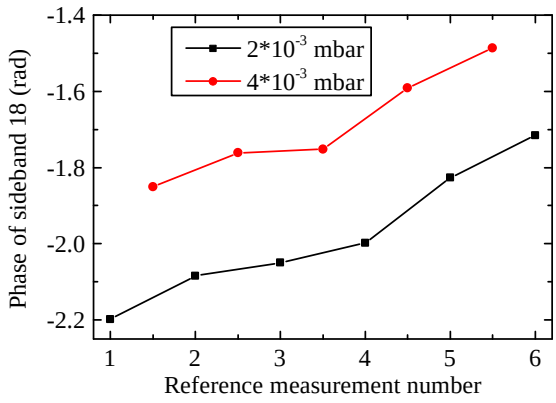

Figure III.37: *Phase of sidebands 18 in consecutive measurements done with alternating pressure.*

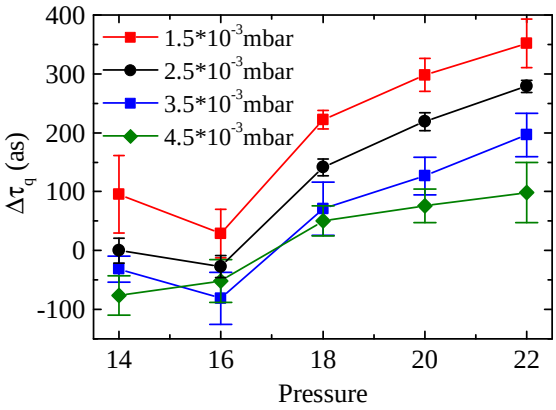

Figure III.38: *Measured sideband delays at different generating pressures.*

has already been discussed in [69] for example) and 2) we introduce a negative GD for the harmonic pairs.

Apart from constant factors, we can write the oscillations in the RABITT measurement as

$$S(\tau, \omega_{q+1}) = C_1 + C_2 cos\left[\tau_p - \tau_{q+1}\right], \tag{III.13}$$

where $\tau_{q+1} = (\phi_{q+2} - \phi_q)/(2\omega_1)$ is related to the group delay of harmonic pairs and τ_p is the delay of the probe pulse.

Since in our stabilized interferometer the phase of the probe field is locked to the phase of the generating driver field which passed through the cell, τ_p can be related to the phase delay of this generating field. As a result, apart from a constant factor we can write that: $\tau_p = \phi_1/\omega$, where ϕ_1 is the phase of the fundamental field at the end of the cell. The GD of attosecond pulses can be related to the phases of the generated harmonics at the end of the cell. Again, apart from a constant factor we can write that $\tau_{q+1} = (\phi_{q+2} - \phi_q)/(2\omega)$. Thus the variations of the measured group delays represent the temporal walk-off of the generated attosecond pulse with respect to the generating driver field.

The cause of this walk-off can be interpreted using the one-dimensional model presented earlier. As shown in section II.4 and in particular in Equation II.26, the phase of a harmonic at the end of the cell depends on the wavevector mismatch. This results

in a phase mismatch between the generated and propagated fields $\phi_q - \varphi_q$. At the end of the cell – if the atomic phase is negligible – this can be written as: $\Delta\phi_q = \phi_q - q\phi_1$. Introducing this quantity into Equation III.13, the variations of the measured sideband delays with pressure can be written as:

$$\Delta\tau_{q+1} = \frac{\Delta\phi_{q+2} - \Delta\phi_q}{2\omega}. \tag{III.14}$$

In a similar manner as in case of Equation II.26, in an absorbing medium the phase mismatch can be written in terms of wavevector mismatch Δk_q, medium length L and absorption coefficient $k_\beta = \beta \cdot 2\pi/\lambda$. In a compact form this reads [69, 8]:

$$\Delta\phi_q = \Delta k_q \frac{L}{2} - arctan\left[\frac{tan\left(\Delta k_q L/2\right)}{tanh\left(k_\beta L/2\right)}\right] + arctan\left[\frac{\Delta k_q}{k_\beta}\right]. \tag{III.15}$$

This shows that the temporal walk-off appears simultaneously with phase mismatch, that – in most cases – is not the same for different harmonics. Absorption also ameliorates this temporal walk-off, as it effectively limits the length of the useful generating medium. Because the absolute pressure in the gas cell is not known, the calibration of a theoretical model that would reproduce the results, is not straightforward. From the dependence of harmonic intensities on the background pressure, the generation pressure can be approximated using for example Equation II.38, (assuming a linear relation between the two pressure values). And, in fact, a similar method has been used in the theoretical model presented in [8] to interpret the results.

The most important consequence of the results presented here is the fact that the delay between attosecond pulses and probe fields is changing with pressure. This emphasises the importance of a stable generation pressure during attosecond pump-probe experiments.

III.6.3 Summary

- **T5 I participated in an experimental campaign measuring the variation of attosecond group delays with the pressure present inside the generation cell. We found that by increasing the pressure the group delay of the attosecond pulse train decreases, in agreement with a one-dimensional propagation model. Due to this, for the stability of attosecond pump-probe measurements to be maintained, not just the optical path lengths, but the generation gas pressure also has to be kept constant.**

IV Final summary

In this thesis an introduction was given to the theory of attosecond pulse synthesis by high-order harmonic generation in gases. The advantages of the HHG technique in attosecond pulse generation was discussed. The basic physics of HHG was presented by an intuitive, classical model, and a few ways to calculate the atomic response to the strong generating laser field were summarized.

The basic physics of macroscopic processes behind HHG were discussed in more detail, like phase-matching, quasi-phase-matching. Both one and three-dimensional models were introduced that can be used to study these important macroscopic effects.

Using these models:

T1.a I have analysed high-order harmonic generation in the presence of strong THz fields, and I have shown that: THz pulses can cause a large extension of the cutoff with reduced GDD, and they can redistribute the amplitude of electron trajectories, making the shorter trajectory class more dominant. Besides the different trajectory lengths, the increased field strength at the moment of ionization (due to the shifted ionization times) also contributes to the stronger yield from short trajectory radiation.

T1.b I have studied how in a macroscopic environment the generation process differs significantly from the single-atom results, and shown that, even in cases when longer laser pulses are used (8, 10 or 12 fs) and the single atom response would yield multiple attosecond pulses, propagation effects can eliminate the contribution from certain sets of trajectories, yielding an isolated attosecond pulse at the exit of the gas cell. The large bandwidth of these pulses greatly decreases their transform limit. I have also shown that the long-trajectory components are also cleaned from the surviving pulse during propagation, resulting in an effective decrease of pulse duration, making the technique promising for obtaining a reliable source of short, isolated attosecond pulses with good contrast and low divergence. By careful adjustment of the parameters, such as gas pressure and peak intensity of the laser pulse, and by adequate spectral filtering short SAPs can be produced in a straightforward manner (without post-compression).

T2.a I have analysed the importance of focusing geometry on phase matching and harmonic yield in HHG when the IR pulse is assisted by a THz pulse, using experimentally verified parameters. I have shown that, despite the limited THz pulse energy, the most powerful SAP can be produced by relatively loose focusing. I attributed this to the deteriorated phase-matching conditions under strong focusing of the long-wavelength fields.

T2.b I have shown that the assisting field can be used to compensate phase mismatch that arises during harmonic generation and the selection of the short or long trajectory components (defining the sign of the resulting SAP's chirp) can be achieved by varying

the delay between the THz and IR pulses.

T3.a I have worked out a model suitable for further optimization, which is based on the single atom response calculation with limited temporal integration. I have shown with macroscopic HHG modelling that the Lewenstein integral is able to partially predict a good approximation of the macroscopic behaviour of the attosecond pulse generation process. I have interpreted the two distinct ways (consecutive half-cycle or short and long trajectory radiation in a single half-cycle generation) of the double attosecond pulse generation.

T3.b I have modelled attosecond pulse generation by the selected driver waveforms with a 3D macroscopic model and shown that the pulse shortening achieved by the optimization remains robust in a macroscopic environment. I have also shown that in case of Gaussian generating beams, tight spatial filtering of the harmonic beam is required for the pulse duration to come close to the ones obtained in the optimization. Moreover, I predict that double attosecond pulses generated from short and long trajectories are only reproducible macroscopically in very inefficient generating conditions.

T4.a I have described a method to calculate the phase-modulation of harmonics by a weak assisting field in terms of the generating laser pulse's parameters, depending on the two fields' relative wavelength and the length of the electron trajectory in question. I have discussed the relationship between the simplest case of a counter-propagating, same wavelength assisting field (analytical treatment), to the case when a different wavelength assisting field is used, and showed that the two can be related through a wavelength-dependent correction factor.

T4.b I have analysed the bandwidth of QPM methods and formulated an approximate expression to calculate it. I have shown that the dependence of phase-modulation amplitude on the harmonic order is not limiting the QPM bandwidth significantly when the method is applied to a large number of coherence periods. Therefore, in these cases the bandwidth does not depend on the shape of the applied assisting field. On the other hand, I have shown that trajectory interferences can significantly change the fine-structure of the QPM efficiency. I have also discussed the optimal field profile of assisting fields for short and long trajectory components for efficient QPM, and I have found that short trajectories have the advantage of requiring the same profile for driver and assisting beams.

T4.c Using a 1D model I have predicted that HHG can be enhanced by perpendicularly propagating long-wavelength fields at photon energies above the phase-matching limit. I calculated the amplitude of the optimal THz field that was used in 3D numerical calculations which verified that these fields are able to induce QPM. In a case study, I have found an increase in efficiency of more than two orders of magnitude around the region of the single-atom cutoff. A chirped THz field, matching the coherence length of the generated harmonics was found to further increase the generation efficiency.

T5 I participated in an experimental campaign measuring the variation of attosecond group delays with the pressure present inside the generation cell. We found that by in-

creasing the pressure the group delay of the attosecond pulse train decreases, in agreement with a one-dimensional propagation model. Due to this, for the stability of attosecond pump-probe measurements to be maintained, not just the optical path lengths, but the generation gas pressure also has to be kept constant.

V Magyar nyelvű összefoglaló

V.1 Bevezető

A tudomány fejlődésében kiemelkedő szerepet játszik a természet alaptörvényeinek feltárása és minél pontosabb megismerése. A legelső törvények, amelyeket az ember felismert olyan jelenségeket magyaráztak, melyeket érzékszerveinkkel közvetlenül észlelni tudunk. A közvetlen érzékeléshez többek között az szükséges, hogy a folyamatra jellemző időskála az érzékszerveink sebességénél lassabb legyen: másodpercek, percek vagy akár évek alatt játszódjon le. A tudomány egyik legfőbb hajtóeleme az emberi kíváncsiság, ami oda vezetett, hogy megpróbáljunk olyan jelenségeket is megmagyarázni, melyek az emberi szem által közvetlenül nem észlelhető időtartamok alatt mennek végbe.

A gyors folyamatok tanulmányozásához olyan érzékelő berendezéseket kell gyártanunk, amelyek egyrészt képesek érzékelni és időben felbontani ezeket a folyamatokat, valamint képesek információt (pl. fényképet) rögzíteni a folyamat időbeli lefolyásának különböző fázisairól. A fényképezés alapjait képező tudás már a 19-edik század végén az ember rendelkezésére állt, és hamar kifejlesztették azokat az eszközöket, amelyek segítségével az emberi szem számára túl gyors jelenségekről pillanatképeket lehet készíteni. Gyors, egymás utáni pillanatképeket készítve és ezeket lejátszva végül elemezni lehet ezen jelenségek időbeli lefolyását. A pillanatkép készítésekor nagyon fontos, hogy a fényképet rögzítő érzékelőt csak nagyon rövid ideig érje fény, különben a gyors folyamat részletei elmosódnak.

Minél gyorsabb a vizsgálandó folyamat, annál gyorsabb pillanatképet készítő berendezésre van szükség. A mechanikus készülékek időbeli feloldását a mozgó alkatrészek tehetetlensége néhány mikroszekundumra korlátozza (1 µs = 10^{-6} s). Az elektronikus készülékek akár nanoszekundumos vagy nagyon különleges berendezések pikoszekundumos időskálán játszódó folyamatokat is fel tudnak oldani.

Az ennél is gyorsabb folyamatok feloldását viszont csak optikai eszközökkel lehet megvalósítani, ahol a detektor sokáig készíti a képet, viszont a céltárgyat csak nagyon rövid ideig éri fény, így csak az a pillanat kerül rögzítésre, amikor a céltárgy meg van világítva. Az ilyen eszközök tehát nem gyors detektorokon, hanem nagyon rövid fényimpulzusokon alapulnak. Ezek időbeli feloldását a módusszinkronizált lézerek által keltett ultrarövid impulzusok jelentősen megnövelték, így már az ezredforduló előtt lehetővé vált a femtoszekundumos skálán lejátszódó folyamatok vizsgálata (1 fs = 10^{-15} s). Mivel 1 fs alatt a fény is mindössze 0,3 µm távolságot tesz meg, nyilvánvaló, hogy az ilyen eszközök ennél apróbb részecskék vizsgálatára alkalmasak. Ebben az idő- és mérettartományban az atomok molekulán belüli mozgása figyelhető meg, például

disszociáció, izomerizáció vagy más kémiai folyamatok során, így az ezzel foglalkozó tudományág a femtokémia nevet kapta.

Ezen tudományág megalkotóját, Ahmed Zewailt 1999-ben Nobel-díjjal tüntették ki, és a díjátadó ünnepségén kifejtette, hogy szerinte minden alkalommal, mikor az elérhető időfelbontást megnöveljük legalább két vagy három nagyságrenddel, várhatóan olyan jelenségeket fogunk felfedezni, amire előre nem is gondoltunk.

Tovább növelve az időfelbontást eljutunk az attoszekundumos tartományig ($1\ \text{as} = 10^{-18}\ \text{s}$) és azokig a részecskékig, amelyek ezen a tartományon mozognak: az elektronokig. Az attoszekundumos skálán lejátszódó folyamatok tehát az elektron mozgásával kapcsolatosak, melyeket elsősorban a fény anyaggal való kölcsönhatása indít útnak. Ilyenek pl a fotoionizáció, Auger bomlás, stb. Az ilyen folyamatok közvetlen, időbontott vizsgálatához attoszekundumos impulzusokra van szükség.

A Fourier tételt alkalmazva kimutatható, hogy egy 100 as hosszú impulzus előállításához majdnem 20 eV sávszélességű sugárzás szükséges. Mivel a hagyományos, látható vagy infravörös sugárzást kibocsátó lézerek központi hullámhossza 1-2 eV fotonenergiának felel meg, egyértelmű, hogy ezek nem alkalmasak attoszekundumos impulzusok keltésére. Az attoszekundumos tartomány eléréséhez legalább ultraibolya (UV), de lehetőleg extrém ultraibolya (XUV) vagy röntgensugárzás szükséges. Viszont a nagy sávszélesség önmagában nem elegendő rövid impulzusok előállításához. Ahogy a lézereknél is, a különböző frekvenciájú komponensek fázisának szinkronizálásával érhető el, hogy az impulzus a lehető legrövidebbre, a spektrum szélessége által korlátozottra csökkenjen. Ezek alapján nyilvánvaló, hogy az attoszekundumos impulzusok előállításához szélessávú, koherens XUV vagy röntgen forrásra van szükség.

V.2 Tudományos előzmények

Az XUV és röntgen tartományban koherens, szélessávú és fázisszinkronizált sugárzás forrása a lézerek által, szilárd felületen vagy gázokban keltett magasrendű felharmonikus sugárzás. Mindkét esetben erős, femtoszekundumos, infravörös impulzus kelti a sugárzást, a szilárd felületről visszaverődve, vagy a gázon áthaladva.

A szilárd felületen történő keltésnek az a legfontosabb előnye, hogy a használt lézertér intenzitásának nincsenek jelenleg ismert elvi korlátai, ezért a keltett sugárzás nagyon intenzív lehet. A hátránya viszont az, hogy eleve csak igen nagy kontrasztú és nagy intenzitású lézerimpulzussal működik, ami tönkreteszi a felületet, ezért minden keltő impulzust „friss" felületre kell irányítani. Ezt általában a felület mozgatásával valósítják meg, ami instabillá teszi a visszavert nyalábot és korlátozza az ismétlési frekvenciát.

A gázokban keltett harmonikusok előnye az alacsony divergencia, jól kontrollálható fázis és jó térbeli koherencia. Ezek az előnyök, a keltő tér korlátolt intenzitása és a folyamat viszonylag alacsony hatásfoka ellenére, előtérbe helyezik ezt a módszert az attoszekundumos impulzusok keltésében és főként az alkalmazásában, így manapság az attoszekundumos impulzusok keltésének ez a legelterjedtebb módja. Ennek a disszertációnak a témája a magasrendű felharmonikusok (HOH) és attoszekundumos impulzusok keltésének vizsgálata gázokban, elsősorban numerikus módszerekkel. Az dolgozat első részében a folyamat tudományos hátterét mutatom be különös figyelmet fordítva azokra a módszerekre, amelyeket a későbbiek folyamán használni fogok. A második rész az általam elért új tudományos eredményeket foglalja össze.

V.2.1 Magasrendű felharmonikusok keltése gázokban

A magasrendű felharmonikus keltés (HHG) gázokban a következőképpen játszódik le: egy intenzív ($\approx 10^{14}$ W/cm^2 csúcsintenzitású) ultrarövid impulzust egy, vákuumba helyezett gázcellába vagy gáznyalábba fókuszálunk. A lézerimpulzus általában néhány(tíz)femtoszekundum hosszúságú és infravörös tartományba eső központi hullámhosszal rendelkezik, a gáz pedig rendszerint nemesgáz.

A nemesgáz használatának elsősorban azért van jelentősége, mert ezeknek nagy az ionizációs energiájuk és alacsony a nemlinearitásuk, így az erős lézertér is képes áthaladni rajta elkerülve az önfókuszálást és azt is, hogy a gázatomok teljesen ionizálttá váljanak. A lézertér és a gázatomok kölcsönhatása során páratlan rendű harmonikusok keletkeznek (az atomi rendszerek inverziós szimmetriával rendelkeznek, így páros rendű folyamatok általában nem jelennek meg). Az alacsonyrendű harmonikusok (3, 5, 7, stb.) intenzitása perturbatív törvény szerint csökken így a keltett spektrumot a harmadik harmonikus dominálja. Emiatt a keltett tér femtoszekundum hosszúságú impulzussorozatból áll.

A HOH-k intenzitása azonban közel azonos, ezért az alacsony harmonikusok kiszűrésével az effektív sávszélesség jelentősen növelhető. Ezt a szűrést általában egy vékony (100-200 nm) fémszűrővel (Al, Zr, stb.) lehet elvégezni. Az így keletkezett XUV

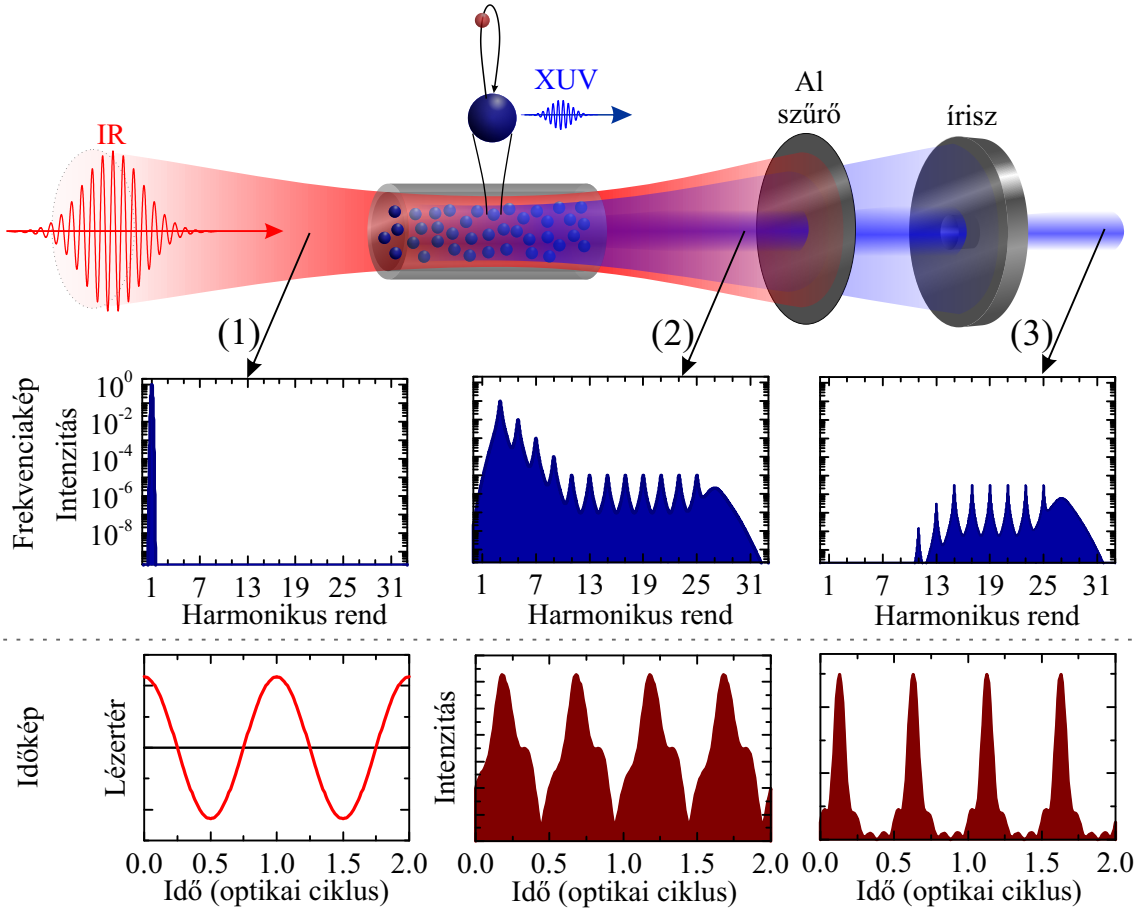

V.1. ábra: *A magasrendű felharmonikusok keltésének sematikus ábrázolása. A (1) lézer és (2) keltett tér spektrális- és időképbeli struktúrája a fémszűrő előtt. (3) Harmonikus spektrum és attoszekundumos impulzusok a spektrális és térbeli szűrés után. Az időképbeli intenzitások nem összemérhetők.*

nyalábot attoszekundumos hosszúságú (60-300 as) impulzusok sorozata alkotja.

V.2.2 Egy-atom modell

A HHG folyamatának alapja egyetlen atom szinten könnyen szemléltethető egy félklasszikus modellel. A lézertér a kezdetben alapállapotban lévő elektront optikai ionizáció során a kontinuumba kényszeríti, ahol ez, a lézer elektromos terében gyorsulva eltávolodik az atomtörzstől. Mikor a tér előjelet vált, az elektron visszajuthat az iontörzs közelébe és rekombinálódva az energiája kisugárzódik egyetlen nagyenergiájú foton formájában.

Az elektron pályáját klasszikus Newtoni mechanika törvényei alapján kiszámolva is egyértelművé válik, hogy minden optikai félciklusban két elektrontrajektória-csoport különböztethető meg, melyeket rövid illetve hosszú trajektóriáknak neveznek. A legmagasabb elérhető fotonenergia pedig a keltő tér intenzitásától és hullámhosszától függ és az $I_p + 3,17U_p$ képlet alapján számolható ki (I_p az ionizációs energiát, míg U_p a ponderomotoros energiát jelöli, lásd a II.6 egyenletet). Mivel a keletkezett fotonok az elektrontól öröklik tulajdonságaikat, az elektronok visszatérési ideje meghatározza a keltett sugárzás

csoportkésleltetését. A visszatérési időket elemezve kiderül, hogy a rövid trajektóriák pozitív, míg a hosszúak negatív csörppel rendelkeznek (a vivőfrekvencia időben nő, illetve csökken).

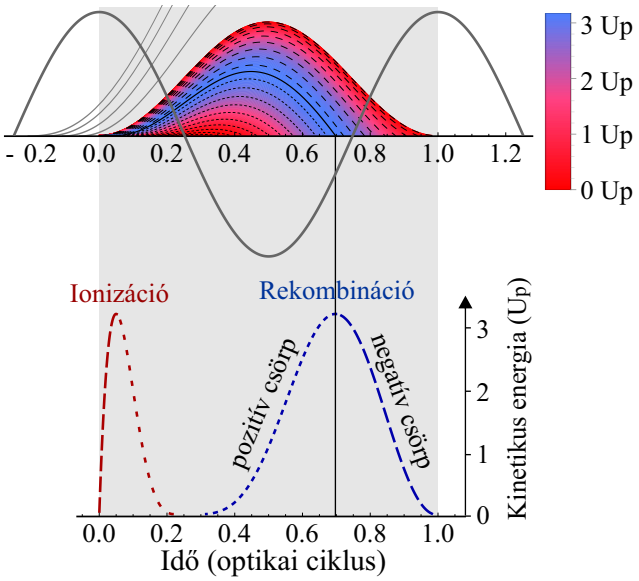

V.2. ábra: *A klasszikus modell alapján számolt elektron trajektóriák (fent). A színskála az elektronok kinetikus energiáját illusztrálja, az atomtörzshöz való visszatérés pillanatában. Az ábra alsó részén a rövid és hosszú trajektóriák ionizációs (piros vonal) és visszatérési időpillanatai (kék vonal) vannak illusztrálva. A rövid szaggatott vonal a rövid, a hosszú szaggatott vonal pedig a hosszú trajektóriákhoz tartozó időpillanatokat mutatja.*

Minél hosszabb az elektron trajektóriája, a keltett sugárzás tulajdonságai annál érzékenyebben változnak a keltő tér alakjától függően. Ez az érzékenység a harmonikusok fázisára is kihat, és az egyik jelentős következménye, hogy a hosszú trajektóriák által keltett sugárzás divergensebb, ezért egy írisszel nagyrészt kiszűrhető.

Egy-atom szinten a keltett HOH sugárzást a Lewenstein integrál segítségével lehet kiszámolni. Ez a Schrödinger egyenlet analitikus egyszerűsítése olyan esetekre, amikor a keltő tér erőssége összemérhető az egyetlen alapállapotú elektronra ható Coulomb tér erősségével, így az ionizáció és rekombináció között (mikor az elektron az iontörzstől távol van) az elektronra ható Coulomb tér elhanyagolható. Az integrál segítségével kiszámolhatjuk az atom lézertér által keltett dipól momentumát bármely pillanatban. Az időfüggő dipólmomentumból ezután megbecsülhetjük a dipólgyorsulást, ami egyben a keltett tér forrása is. Ennek a Fourier transzformáltjából megkapjuk a keltett harmonikus spektrumot, ami spektrálisan szűrés és inverz Fourier transzformálás után megadja a keltett attoszekundumos impulzusokat.

V.2.3 A fázisillesztés feltételei

Mivel a HOH keltés folyamata kevesebb mint egy optikai ciklus alatt lejátszódik, és az atomok közötti távolság jelentősen nagyobb mint az elektron maximális kitérése, az elektron

fázisát nem befolyásolják külső hatások (pl. ütközések) csak az iontörzs és a keltő elektromos tér tulajdonságai. Ennek eredménye, hogy a HHG egy koherens folyamat és a keltett sugárzás örökli a keltő lézertért tulajdonságait. A koherens folyamatokra jellemzően a keltett fotonok száma a kölcsönható részecskék számának négyzetével arányosan nőhet, amennyiben sikerül biztosítani, hogy a mérési ponton a részecskék által keltett sugárzások erősítsék egymást, vagy más szavakkal, hogyha a fázisillesztés feltételei biztosítottak.

A fázisillesztést befolyásolja a lézertér és a harmonikus tér fázissebességei közti különbség, és a lézertér intenzitásának térbeli eloszlása. Mivel a keltett harmonikusok a keltésre használt gázatomok ionizációs energiájánál nagyobb fotonenergiával rendelkeznek, a fázissebességük ebben a közegben nagyobb mint c. A keltő IR sugárzás frekvenciája viszont a legerősebb abszorpciós vonalak alatt helyezkedik el, így a fázissebessége mindig alacsonyabb mint c. Ennek következtében a fázisillesztés feltétele alapesetben nem teljesül.

A HHG során azonban mindenképp keletkeznek szabad elektronok is. A szabad elektronok alaptulajdonsága ez erős, negatív polarizálhatóság, így ezek jelentősen növelik az elektromágneses sugárzás fázissebességét. A szabad elektronok okozta törésmutatóváltozás (plazma-törésmutató) arányos a szabadelektron-sűrűséggel és négyzetesen nő a sugárzás hullámhosszával. Ennek következtében az IR tér fázissebességét jelentősen befolyásolja a gáz nyomása és az ionizációs fok, viszont az utóbbi az XUV fázissebességére alig gyakorol hatást.

Csupán az eddig említett hatásokat figyelembe véve az IR és XUV sugárzás fázissebessége összehangolható az ionizációs fok szabályozásával, amit a lézerimpulzus hossza és intenzitása határoz meg. Mivel úgy a plazma, mint a semleges atomok okozta törésmutatóváltozás egyenesen arányos a részecskesűrűséggel, a megfelelő ionizáció mellett a fázissebességek megegyeznek, függetlenül a gáz nyomásától.

A fókuszált lézernyalábokná a tér fázissebességét azonban befolyásolja a fókusz közelében fellépő fázisugrás is (Gouy fázis). Ez egy nyomástól független tagot hoz be a fázisillesztés egyenletébe, így a fázisillesztés egy adott fókuszálás és ionizációs fok mellett csak jól meghatározott nyomáson teljesülhet. A helyzetet tovább bonyolítja a trajektória hosszától függő atomi fázis is, ami miatt a keltett harmonikus fázisa függővé válik a lézertér intenzitásától. Ez a tag növeli a keltett nemlineáris polarizáció effektív fázissebességét a fókusz előtt és csökkenti a fókusz után. Ennek a hatása viszonylag kicsi a rövid trajektóriák esetén, ezért sok fázisillesztési modellben elhanyagolják. Ez azzal indokolható, hogy adott fókuszálás mellett általában a Gouy fázisugrás sokkal nagyobb mértékű fázissebesség-változást okoz, így az dominálja a fázisillesztés feltételeit.

A különböző komponensek jellemezhetők a hozzájuk tartozó effektív hullámvektorokkal, és a hatásuk az V.3 ábrán van összesítve. A fentiek alapján elmondhatjuk, hogy adott fókuszálás mellett a keltő tér Gouy fázisa okozta fázissebességnövekedés csak akkor kompenzálható, hogyha a keltő gázban a törésmutatóból adódó fázissebesség az IR térre alacsonyabb, mint az XUV-ra. Ez csak

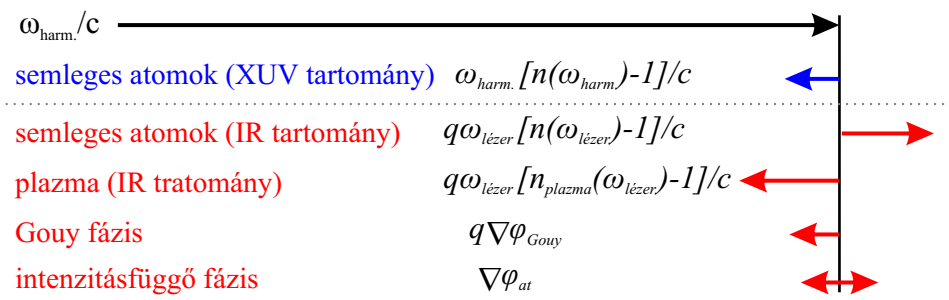

V.3. ábra: *A fázisillesztés különböző komponenseit összefoglaló ábra. A fázisillesztés teljesüléséhez, közegben terjedő XUV tér hullámvektora (kék) meg kell egyezzen a keltett XUV tér hullámvektor-komponenseinek az összegével (piros). A vektorok egy c-vel mozgó koordinátarendszerben vannak ábrázolva és hosszuk nem méretarányos.*

egy adott ionizációs fok alatt valósítható meg, ami határt szab a keltésre használt impulzus intenzitásának. Ez a határ az impulzus hosszától, központi frekvenciájától és az adott gáz tulajdonságaitól függ. Összességében elmondható, hogy a leggyakrabban használt 800 nm-es hullámhosszú, néhányciklusú impulzusokkal, argonban a legnagyobb megengedett IR intenzitás hozzávetőlegesen 70 eV energiájú fotonok keltésére elegendő, míg neonban ez a határ 120 eV környékén húzódik. Ezek az értékek azonban csak gyenge fókuszálás mellett közelíthetők meg a gyakorlatban használt gáznyomások mellett, az erősebb fókuszálás alacsonyabbra viszi a határokat.

V.2.4 Kvázi-fázisillesztés

A fázisillesztési határ feletti harmonikusok hatékonyan kelthetők kvázifázisillesztés (QPM) segítségével. HOH-k esetén a QPM megvalósítható például a keltett harmonikusok fázisának modulálásával, amit egy gyenge, a lézertől független, külső tér hoz létre. Ez a következőképpen képzelhető el: a keltett harmonikusok a fázissebességkülönbségek miatt csak egy korlátolt távolságon belül interferálnak konstruktívan. Ezután a hossz után a külső tér megváltoztatja a keltett harmonikusok trajektóriáját úgy, hogy π fázisugrást idézzen elő, így a következő térrészben ismét konstruktív interferencia jön létre. A következő cellarész végén a tér megszűnik, ismételt π fázisugrást okozva a keltett harmonikusoknál és a folyamat periodikusan ismétlődik, lehetővé téve, a részleges konstruktív interferenciát hosszú gázcellák esetén is.

Az ilyen típusú QPM azon a megfigyelésen alapszik, hogy egy gyenge külső tér a térerősséggel egyenesen arányosan modulálja a HOH-k fázisát így a fázismoduláció alakja követi az asszisztáló tér alakját. A fentebb leírt QPM megvalósítható például periodikus sztatikus elektromos tér jelenlétében, amely négyszögjelszerűen modulálja a keltett HOH-k fázisát. Hasonló módon szinuszos tér is képes QPM-et létrehozni. Ez megvalósítható például egy, a keltő lézertérrel szemben, vagy arra merőlegesen haladó, aránylag gyenge elektromágneses hullámmal.

V.2.5 Háromdimenziós, numerikus modell

A HHG folyamán fellépő makroszkopikus hatások tanulmányozását az eddig összegzett, egydimenziós modellek jelentősen megkönnyítik, viszont a pontos leíráshoz háromdimenziós, numerikus modellek szükségesek. Az általunk használt modell, a hullámegyenlet megoldásán alapszik, paraxiális közelítésben.

A korábban említett Lewenstein integrál jól leírja a HOH keltés folyamatát, azonban a levezetésénél alkalmazott közelítések miatt nem alkalmas a gázatomok nemlineáris polarizációjának számolására alacsony frekvenciákon. A HOH keltés erőssége viszont nagyságrendekkel alacsonyabb a perturbatív folyamatok erősségénél, ezért a lézertér közegben való terjedése és a HOH keltés szétválasztható.

Ezek alapján a lézertér terjedése perturbatív szinten kezelhető, amennyiben figyelembe vesszük a keletkező plazma hatását. Ez megoldható az időfüggő ionizáció és az ehhez kapcsolódó időfüggő törésmutató kiszámolásával. Mivel ezek a mennyiségek nemlineárisan függenek a keltő tér erősségétől, a hullámegyenletet iteratív módon kell megoldani minden lépésben. A gázcella bemeneténél a teret egy Gaussz nyalábbal közelítve írjuk le, innen pedig a hullámegyenlet megoldásával propagáltatjuk tovább.

Az így kapott lézertérből a cella minden pontjában kiszámoljuk az egy-atom választ a Lewenstein integrált használva, majd megoldjuk a hullámegyenletet a harmonikus térre, az így kapott egy-atom választ tekintve a sugárzás forrásának, valamint az abszorpciót figyelembe véve. A dolgozat további részében kapott eredmények eléréséhez, a fentebb összefoglalt modelleket és módszereket alkalmaztam.

V.3 Eredmények

A fentebb említett modelleket használva a következőkben felsorolt, tézispontokba szedett eredményeket értem el.

T1.a A THz tér jelenlétében keltett magasrendű felharmonikus tulajdonságainak vizsgálatával kimutattam, hogy a THz impulzus jelenléte jelentősen megnöveli az elérhető levágási energiát, csökkenti az impulzusok GDD-jét, valamint felerősíti a rövid trajektóriákból származó sugárzást a hosszúakhoz képest. A trajektóriák hosszának változása mellett az ionizáció pillanatában jelen levő - az eltolódott ionizációs idők miatt - erősebb elektromos tér is hozzájárul a rövid trajektóriák felerősödéséhez.

T1.b Megvizsgáltam a folyamat során jelentkező makroszkopikus hatásokat és kimutattam, hogy ezek lehetővé teszik a hosszabb infravörös impulzusokkal (8, 10 vagy akár 12 fs) való izolált attoszekundumos impulzusok keltését. Ezekben az esetekben az egy-atom modellek impulzussorozatot jósolnak, viszont a makroszkopikus – fázisillesztési – hatások meggátolják az impulzusok felerősödését a lézertér egyes félciklusaiban.

Kimutattam továbbá, hogy a keltés során a sugárzás megtisztul a hosszú trajektóriákból származó komponensektől, aminek hatására a keltett attoszekundumos impulzus hossza is lerövidül. Ez ígéretessé teszi a vizsgált módszert izolált attoszekundumos impulzusok hatékony keltéséhez. Igazoltam, hogy a paraméterek (mint pl. gáznyomás, lézer intenzitás) megfelelő megválasztásával és a spektrális szűrés hangolásával rövid izolált attoszekundumos impulzusok kelthetőek utólagos impulzuskompresszió nélkül is.

T2.a Vizsgáltam a fókuszálási hatások szerepét a THz tér jelenlétében keltett HOH-k fázisillesztésére, valós, kísérletileg igazolt THz impulzusok paramétereit használva. Kimutattam, hogy a limitált THz impulzusenergia ellenére, a legintenzívebb izolált attoszekundumos impulzus relatív gyenge fókuszálás mellett hozható létre. Ezt a hatást elsősorban a hosszú hullámhosszú tér erős fókuszálása által okozott fázisillesztés-romlásnak tulajdonítottam.

T2.b Kimutattam, hogy az asszisztáló tér alkalmas arra, hogy a fázisillesztést szelektíven javítsa rövid vagy hosszú trajektóriák esetén. A szelekciót a lézer és asszisztáló tér közötti időkésleltetés változtatásával lehet elérni és ezzel a keltett impulzus GDD-jének előjele is változtatható.

T3.a Előterjesztettem egy – további optimalizálásban alkalmazható – modellt, amely a Lewenstein integrál korlátolt időtartományon való alkalmazásán alapul. Makroszkopikus számolásokat alkalmazva kimutattam, hogy ez a modell részben alkalmas az attoszekundumos impulzusok keltésénél jelentkező makroszkopikus hatások előrejelzésére. Értelmeztem a duplaimpulzus-keltés két különböző mechanizmusát (egymás utáni félciklusokból, valamint rövid-hosszú trajektóriapárokból keletkezhetnek duplaimpulzusok).

T3.b Makroszkopikus számolásokkal modelleztem az optimalizált lézerterek által keltett attoszekundumos impulzusok tulajdonságait és kimutattam, hogy az egy-atom

szinten elért impulzusrövidülés makroszkopikus környezetben is megmarad. Kimutattam továbbá, hogy Gausszos keltő nyaláb használatakor a harmonikus nyaláb térbeli szűrése elengedhetetlen a rövid attoszekundumos impulzusok előállításához. Ezen felül, a számolásaim azt mutatják, hogy a rövid és hosszú trajektóriapárokból keltett duplaimpulzusok megvalósítása, a hatékonyság szempontjából előnytelen makroszkopikus paraméterek megválasztása mellett lehetséges.

T4.a Kidolgoztam egy módszert, amely segítségével a gyenge asszisztáló tér által okozott fázismoduláció amplitúdója meghatározható a keltő és asszisztáló tér valamint az elektron-trajektóriák paramétereinek függvényében. Tárgyaltam az összefüggéseket azon esetek között, mikor az asszisztáló és keltő tér hullámhossza megegyezik, és mikor ezek különbözőek és kimutattam, hogy a fázismoduláció amplitúdója a két esetben hasonló módszerrel számolható ki, mindössze egy korrekciós faktor bevezetése szükséges, mely a két tér relatív hullámhosszával jellemezhető.

T4.b Elemeztem a kvázi-fázisillesztési módszerek hatékonyságának sávszélességét, és kidolgoztam egy közelítő, analitikus képletet ennek a meghatározására. Kimutattam, hogy fázismoduláció trajektóriafüggése nem korlátozza jelentősen a sávszélességet, olyan esetekben, mikor a QPM módszer nagyszámú periódusra alkalmazott. Ezekben az esetekben a sávszélesség független az asszisztáló tér alakjától. Kimutattam , hogy a trajektóriák közti interferencia jelentősen befolyásolja a kvázi-fázisillesztés hatékonyságának finomszerkezetét. Tárgyaltam az asszisztáló tér optimális nyalábkeresztmetszetét és rámutattam, hogy ez különbözik rövid és hosszú trajektóriák esetén. A rövid trajektóriák kvázi-fázisillesztésénél előny, hogy a keltés abban az esetben optimális, mikor az asszisztáló és keltő tér nyalábkeresztmetszete közel azonos.

T4.c Egy-dimenziós modellt használva kiszámoltam, hogy a lézertérre merőlegesen terjedő tér alkalmas a harmonikuskeltés hatékonyságának növelésére, a fázisillesztési határnál magasabb fotonenergiájú harmonikusokra is. Kiszámoltam a használandó THz tér optimális amplitúdóját, mely alapján 3D modellszámolások igazolták a THz terek kvázi-fázisillesztésének hatékonyságát. Egy esettanulmányban több mint két nagyságrendnyi hatékonyságnövekedést mutattunk ki a levágási fotonenergia környéki harmonikusokra. Csörpölt THz-es impulzusok használatával további növekedést lehet elérni.

T5 Részt vettem egy kísérletsorozatban mely során attoszekundumos csoportkésleltetés változását mértük a keltő gázcellában uralkodó nyomás függvényében. Azt találtuk, hogy a nyomás növekedésével az attoszekundumos impulzussorozat csoportkésleltetése csökken, melyet egy egy-dimenziós modellszámolás is alátámaszt. Ez alapján kimutattuk, hogy az attoszekundumos pumpa-próba kísérletekben, a késleltetés stabilitásának megőrzése érdekében, az optikai úthossz mellett, a keltő cellában a gáznyomást is állandóan kell tartani.

Abbreviations/Rövidítések

ADK	–	Ammosov-Delone-Krainov; a model for tunneling ionization	Ammosov-Delone-Krainov; alagutas ionizáció számolására használt modell
APT	–	attosecond pulse train	attoszekundumos impulzussorozat
ATI	–	above threshold ionization	küszöb feletti ionizáció
CEP	–	carrier to envelope phase	vivő-burkoló fázis
CWE	–	coherent wake emission	koherens ébredő tér keltés
DAP	–	double attosecond pulse	dupla attoszekundumos impulzus
DC	–	static electric field (shorthand for direct current)	sztatikus elektromos tér
DFG	–	difference frequency generation	különbség-frekvencia keltés
FEL	–	free-electron laser	szabadelektron-lézer
(i)FT	–	(inverse) Fourier transform	(inverz) Fourier transzformáció
FTL	–	Fourier transform limit	Fourier korlát
FWHM	–	full width at half maximum	félértékszélesség
GA	–	genetic algorithm	genetikus algoritmus
GD	–	group delay	csoportkésleltetés
GDD	–	group delay dispersion	csoportkésleltetés-diszperzió
HHG	–	high-order harmonic generation	magasrendű felharmonikus-keltés
HOH	–	high-order harmonic	magasrendű felharmonikus
IR	–	infrared	infravörös
MIR	–	mid-infrared	közép-infravörös
NIR	–	near infrared	közeli infravörös
o.c.	–	optical cycle	optikai ciklus
PMM	–	phase-mismatch	fázisillesztetlenség
QPM	–	quasi-phase-matching	kvázi fázisillesztés
RABITT	–	reconstruction of attosecond beating by interferometric two-photon transtion	interferometrikus, kétfoton-átmeneten alapuló attoszekundumos impulzus-sorozat rekonstruálás
ROM	–	relativistic oscillating mirror	relativisztikus oszcilláló tükör
SAP	–	single attosecond pulse	izolált attoszekundumos impulzus
SFA	–	strong field approximation	erős-tér közelítés
TEM	–	transverse electric mode	transzverzális módus
TOD	–	third-order dispersion	harmadrendű diszperzió
UV	–	ultraviolet	ultraibolya
x-ray	–	part of the electromagnetic spectrum characterized by vacuum wavelengths below 10 nm	röntgen; sugárzás, melyet 10 nm-nél rövidebb vákuumbeli hullámhossz jellemez
XUV	–	extreme ultraviolet; part of the spectrum between ultraviolet and x-ray	extrém ultraibolya

Notations/Jelölések

General considerations

Here we list some of the most commonly used variables, and some general rules used in the notations. Subscript 1 (O_1) refers to quantities at the laser frequency, q (O_q) refers to harmonic order q, and a (O_a) refers to a weak assisting field.

Variables that are used to denote electric field and spectral amplitudes and have a tilde on top ($\widetilde{O}$) refer to complex quantities, and variables written in bold ($\boldsymbol{O}$) to vector quantities.

To conform with the generally accepted notations several symbols denote multiple quantities in different contexts. For example the variable A denotes vector potential, phase-modulation amplitude, transition probability amplitude and the first element of the ABCD ray-transfer matrix. It should be clear from the the context to which quantity it refers at any point, because these different quantities appear in different sections. Therefore the table below is just a guide, it does not list general rules.

Notations

e	–	Euler's number, or elementary charge	Euler szám, vagy elemi töltés
E	–	electric field amplitude	elektromos tér amplitúdója
Env	–	envelope	burkoló
H	–	harmonic field amplitude	harmonikusok elektromos terének amplitúdója
I	–	irradiance, optical intensity	intenzitás
I_p	–	ionization energy	ionizációs energia
k	–	wavenumber, wavevector	hullámszám, hullámvektor
Δk	–	wavevector mismatch	fázisillesztetlenség hullámvektora
q	–	harmonic order	harmonikus rend
φ	–	phase	fázis
ϕ	–	phase of the propagated field	propagált tér fázisa
λ	–	wavelength	hullámhossz
t	–	time	idő
τ	–	time delay	időkésleltetés
T	–	oscillation period	periódus
n	–	refractive index	törésmutató
ω	–	angular frequency	körfrekvencia
U_p	–	ponderomotive energy	ponderomotoros energia
w	–	beam radius	nyalábsugár
z_r	–	Rayleigh range	Rayleigh távolság
z	–	distance from the laser focus	fókusztól mért távolság

Acknowledgments

I would like to thank everybody who helped me – directly or indirectly – to complete this thesis.

I owe special thanks to my supervisor, Katalin Varjú, for guiding me through the wast and busy jungle of physics research and for helping me to find answers to not just questions in science, but to "life, the universe and everything".

I owe many thanks to Valer Tosa, my first supervisor in attosecond physics, who still helps me today in my research.

I would like to thank my colleagues in Lund for their company and help during my visit at the Department of Atomic Physics, especially to Diego Guenot, David Kroon, Cord Arnold, Piotr Rudawsky, Christoph Heyl and all the other PhD students and colleagues at the department. I owe special thanks to my supervisors in Lund during our experimental campaign, especially to Anne L'Huillier and Johan Mauritsson.

I thank the coordinators of the ATTOFEL network Marc Vrakking and Thomas Schultz for creating and managing this network, which made possible for me to visit several research institutions, make new friends and start collaborations all over Europe. I thank all the ATTOFEL fellows with whom I started this journey in attosecond physics research, for their support and pleasant company during network meetings.

I also thank the ATTOFEL network for financial support, which made possible for me to visit several summer schools and the network meetings, where I got to know the European attosecond research community. The opportunities opened to me by ATTOFEL contributed significantly to the research presented in this thesis. I also thank the Hungarian Scientific Research Fund (OTKA NN107235) for financial support.

Köszönetnyilvánítás

Köszönetemet szeretném kifejezni mindazoknak, akik közvetve, vagy közvetlenül hozzájárultak a dolgozatom megírásához és az ehhez vezető, évekig tartó munka eredményességéhez.

Köszönettel tartozom elsősorban témavezetőmnek, Varjú Katalinnak, a rengeteg segítségért, útmutatásért és bíztatásért, amelyek nélkül ez a dolgozat biztosan nem készülhetett volna el, valamint a végtelen türelméért és támogatásáért, amivel segített átvészelni az elmúlt néhány év, számomra legnehezebb időszakait.

Köszönöm Dr. Hopp Bélának, Dr. Szabó Gábornak, Dr. Osvay Károlynak és Dr. Rácz Bélának, hogy biztosították a doktori fokozatszerzéshez szükséges feltételeket.

Köszönettel tartozom korábbi témavezetőimnek Tosa Valernak, aki bevezetett az attoszekundumos fizikába, Néda Zoltánnak, aki megtanította nekem a kutatás alapjait és feltárta előttem a tudományos kutatás lényegét, Vicsek Tamásnak, akitől rengeteg új megközelítési módot és nagyon sok emberséget tanultam, valamint Bődi Kálmánnak, középiskolás fizikatanáromnak és osztályfőnökömnek, aki megszeretette velem a fizikát.

Hálás vagyok Kovács Katalinnak, aki mindig segítőkész, türelmes és megértő volt közös munkánk során, és aki tulajdonképp elindított ezen az úton, azzal, hogy gondolt rám, mikor a kolozsvári kutatóintézetbe fiatal munkaerőt kerestek.

Köszönöm családomnak, hogy mindig mellettem álltak és támogattak. Köszönöm édesanyámnak és nővéremnek a sok bíztatást és kitartó támogatást. Köszönettel tartozom édesapámnak, akitől megtanultam, hogy a dolgok megértéséhez hozzá tartozik az, hogy ezeket darabjaira szedjük, és aki megszeretette velem a műszaki tudományokat, azzal hogy feltárta előttem az építés csodáját: hogy képesek vagyunk egyszerű elemi összetevőkből teljesen új és összetett szerkezeteket alkotni.

Köszönettel tartozom közvetlen munkatársaimnak, akiktől nagyon sokat tanultam a munkám során, különösen Dombi Péternek, Hebling Jánosnak, Farkas Győzőnek, Fülöp Józsefnek, Bódi Balázsnak, Major Balázsnak és Farkas Balázsnak.

Köszönettel tartozom a TeWaTi csoport tagjainak, hogy befogadtak ebbe a közösségbe. Különös hálával tartozom Dr. Börzsönyi Ádámnak, Dr. Sipos Áronnak és Kiss Bálintnak, hogy a mindennapjaimat feldobták jelenlétükkel, poénjaikkal és segítségükkel.

Köszönettel tartozom továbbá irodatársaimnak, Péter Viktóriának, Szalai Anikónak, Szekeres Gábornak, Dr. Vass Csabának és Jójárt Péternek, hogy feldobták a hangulatot a sok, számítógép előtt eltöltött idő alatt.

Köszönöm továbbá barátaimnak és volt évfolyamtársaimnak az állandó támogatást.

Appendices

A Calculation of the ionization rate

Free electron generation by long-wavelength electromagnetic fields in the tunnelling regime can be calculated in the frame of the Keldysh theory [195], where the instantaneous rate of ionization is calculated for a DC field. To determine the instantaneous rate, the Ammosov-Delone-Krainov (ADK) formula can be used [187]. This is a reasonably good approximation in the limit when the Keldysh parameter is $\gamma \ll 1$, although for very short ($\approx$1 cycle) pulses its accuracy worsens [188].

In the ADK model the time-dependent free-electron population is calculated as

$$\rho_e(t) = exp\left[-\int_{-\infty}^{t} w_{ADK}(t')dt'\right], \tag{A.1}$$

where w_{ADK} is the instantaneous DC ionization rate.

Using the formulation presented in [196] for an electron in a state with effective quantum number $n^* = \sqrt{I_{ph}/I_p}$, orbital quantum number l, and magnetic quantum number m, the ionization rate w_{ADK} in atomic units can be calculated as

$$w_{ADK}(t) = |C_{n^*l^*}|^2 f_{lm} I_p \sqrt{\frac{6}{\pi}} \left(\frac{2(2I_p)^{3/2}}{E(t)}\right)^{2n^*-|m|-3/2} exp\left(-\frac{2(2I_p)^{3/2}}{3E(t)}\right), \tag{A.2}$$

where I_{ph} is the ionization energy of a Hydrogen atom and

$$f_{lm} = \frac{(2l+1)(l+|m|)!}{2^{|m|}|m|!(l-|m|)!} \tag{A.3}$$

$$|C_{n^*l^*}|^2 = \frac{2^{2n^*}}{n^*\Gamma(n^*+l^*+1)\Gamma(n^*-l^*)} \tag{A.4}$$

Γ is an extension of the factorial to real and complex valued arguments, and called Gamma function.

In these equations $l^* = n^* - 1$ can be used. The ionization rate can be averaged over different magnetic quantum numbers [196], or $m = 0$ can also be used, because the ionization rate for electrons with $m = 0$ is much higher then for those with $m = \mp 1$ [187]. The free-electron density in a gas is calculated as $N_e = N_a \times \rho_e$, where N_a is the initial density of neutral atoms.

B Nonlinear refractive index

The third-order susceptibility causes the induced polarization to scale with the third power of the electric field amplitude. Due to this, the refractive index of neutral atoms can be expanded to contain a linear part n_0 and an intensity-dependent part [30]

$$n = n_0 + n_2 I. \tag{B.1}$$

The value of n_2 is related to $\chi^{(3)}$ by the relation

$$n_2 = \frac{3}{2n_0^2 \epsilon_0 c} \chi^{(3)}. \tag{B.2}$$

The intensity-dependence cause the refractive index to increase at the leading edge of the pulse, and decrease at the trailing edge, yielding the phenomenon called self-phase-modulation (among many others). Because the laser beam also has a spatial intensity distribution, a positive n_2 also causes the more intense, central part of the beam to propagate with slower phase-velocity, thus bending the phase-front and focusing the beam (self-focusing), it is thus an important effect in propagation The values of n_2 for noble gases can be determined from measurement data [197, 198, 199], or can be approximated by calculation [200]. Measurement data for n_2 values vary widely, and differences up to an order of magnitude appear between different results. For different gases n_2 varies significantly, for Argon it is $\approx 8 \times 10^{-20}$ cm^2/W, for neon it is about 10 times smaller [200]. In this thesis the values presented in [201] are used.

C Amplitude of harmonic phase modulation due to laser field interference

Here we describe the harmonic phase modulation induced by the interference of the driver with a weak assisting field, resulting Equation III.1 and Equation III.2. We take a driver laser field at an arbitrary point in the HHG medium along the z axis, and describe it as $E_1 sin(\varphi_1)$, where $\varphi_1 = \omega_1 t + |\vec{k}_1 \vec{z}|$ is the phase of the laser field at the chosen coordinate, that is a function of space and time. At the same point the assisting field can be described as $E_a sin(\varphi_1 + \delta)$, where $\delta = \varphi_a - \varphi_1$ denotes the phase difference between the two fields, $\varphi_a = \omega_1 t + |\vec{k}_a \vec{z}|$ being the phase of the low-intensity assisting field. Thus δ becomes a function of space, when the wavevectors $\vec{k}_1$ and $\vec{k}_a$ enclose a nonzero angle. The resulting wave can be calculated as

$$E_{tot} sin(\varphi_1 + \theta_{tot}) = E_1 sin(\varphi_1) + E_a sin(\varphi_1 + \delta), \tag{C.1}$$

with E_{tot} denoting its amplitude and θ_{tot} its phase.

In the following calculations we assume that $E_a \ll E_1$. The phase of the resulting wave then can be expressed as

$$\begin{aligned} \theta_{tot} &= arctan\left[\frac{E_a sin(\delta)}{E_1 + E_a cos(\delta)}\right] = arctan\left[\frac{\frac{E_a}{E_1} sin(\delta)}{1 + \frac{E_a}{E_1} cos(\delta)}\right] \\ &\approx arctan\left[\frac{E_a}{E_1} sin(\delta)\right] \approx \frac{E_a}{E_1} sin(\delta). \end{aligned} \tag{C.2}$$

This term has its first maximum at $\delta = \pi/2$, and the magnitude of the phase-modulation is given by E_a/E_1.

In HHG the phase of the generated harmonic depends on the phase of the generating wave multiplied by the harmonic order q [64]. As a result the phase-modulation of the generating field described by Equation C.2 will translate to a *direct* modulation of the harmonic phase with amplitude

$$\Delta\varphi_p \approx q\frac{E_a}{E_1}. \tag{C.3}$$

The harmonic's phase also depends on the intensity of the generating wave, this contribution is usually referred to as the atomic phase, as it is inherited from the electron which accumulates it during its travel from ionization to recombination. This is well approximated with $\varphi_I = -\alpha U_p/(\hbar\omega_1)$, where $U_p = e^2E^2/(4m_e\omega_1^2)$ is the ponderomotive

energy [63]. As the amplitude of the resulting wave in Equation C.1 is given by

$$E_{tot} = \sqrt{E_1^2 + E_a^2 + 2E_1E_a cos(\delta)}, \tag{C.4}$$

it is clear that the generating field's amplitude is also modulated with changing δ and it has its first maximum at $\delta = 0$. This amplitude modulation thus causes an *indirect* modulation of the harmonic phase. In this case the atomic phase being

$$\varphi_I = \frac{-\alpha e^2}{4m_e\hbar\omega_1^3}\left[E_1^2 + E_a^2 + 2E_1E_a cos(\delta)\right], \tag{C.5}$$

it is modulated with an amplitude given by

$$\Delta\varphi_I = \frac{-\alpha e^2}{2m_e\hbar\omega_1^3}E_1E_a. \tag{C.6}$$

Both of these factors have been described in [115, 65], for the most relevant case, when the phase difference is calculated for two counterpropagating waves, where $\varphi_1 = \omega_1 t - k_1 z$ and $\varphi_a = \omega_1 t + k_1 z$, giving $\delta = 2k_1 z$.

These two different sources of phase-modulation are comparable in magnitude, but the description above shows that they always occur with a shift of $\pi/2$ in the value of δ. This derivation forms the basis of our discussion in subsection III.4.1.

Bibliography

[1] V. Tosa, **E. Balogh**, and K. Kovács. Phase-matched generation of water-window x-rays. *Phys. Rev. A*, 80(4):045801, Oct 2009.

[2] **Emeric Balogh**, Jozsef A. Fulop, Janos Hebling, Peter Dombi, Gyozo Farkas, and Katalin Varju. Application of high intensity thz pulses for gas high harmonic generation. *Central European Journal of Physics*, 11(9):1135–1140, 2013.

[3] **Emeric Balogh**, Katalin Kovacs, Peter Dombi, Jozsef A. Fulop, Gyozo Farkas, Janos Hebling, Valer Tosa, and Katalin Varju. Single attosecond pulse from terahertz-assisted high-order harmonic generation. *Phys. Rev. A*, 84:023806, Aug 2011.

[4] **Emeric Balogh**, Katalin Kovács, Valer Tosa, and Katalin Varjú. A case study for terahertz-assisted single attosecond pulse generation. *Journal of Physics B: Atomic, Molecular and Optical Physics*, 45(7):074022, 2012.

[5] Katalin Kovács, **Emeric Balogh**, János Hebling, Valer Toşa, and Katalin Varjú. Quasi-phase-matching high-harmonic radiation using chirped thz pulses. *Phys. Rev. Lett.*, 108:193903, May 2012.

[6] K. Kovacs, **E. Balogh**, J. Hebling, V. Tosa, and K. Varju. Quasi-phase-matching high-harmonics with thz assistance. *AIP Conference Proceedings*, 1462(1):41–44, 2012.

[7] **E. Balogh** and K. Varjú. Quasi-phase-matched high-order harmonic generation by low-intensity assisting fields: field strength scaling and bandwidth. *submitted*.

[8] D. Kroon, D. Guenot, M. Kotur, **E. Balogh**, E. W. Larsen, C. M. Heyl, M. Miranda, M. Gisselbrecht, J. Mauritsson, P. Johnsson, K. Varju, A. L'Huillier, and C. L. Arnold. Attosecond pulse walk-off in high-order harmonic generation. *Optics Letters*, 39:2218, 2014.

[9] Diego Guenot, David Kroon, **Imre Balogh**, Witting Larsen Esben, Kotur Marija, Miranda Miguel, Thomas Fordell, Per Johnsson, Johan Mauritsson, Mathieu Gisselbrecht, Katalin Varju, Cord Arnold, Thomas Carette, Anatoly Kheifets, Eva Lindroth, Anne L'Huillier, and Marcus Dahlstrom. Measurements of relative photoemission time delays in noble gas atoms. *submitted*.

[10] **E. Balogh**, B. Balazs, V. Tosa, E. Goulielmakis, P. Dombi, and K. Varju. Genetic optimization of attosecond pulse generation in light-field synthesizers. *submitted*.

[11] Jan-Claude Diels and Wolfgang Rudolph. *Ultrafast laser pulse phenomena*. Elsevier Academic Press, 2006.

[12] J. Itatani, F. Quéré, G. L. Yudin, M. Yu. Ivanov, F. Krausz, and P. B. Corkum. Attosecond streak camera. *Phys. Rev. Lett.*, 88:173903, Apr 2002.

[13] Ferenc Krausz and Mark I. Stockman. Attosecond metrology: from electron capture to future signal processing. *Nature Photonics*, 8:205–213, 2014.

[14] I. N. Bronstein and K. A. Semendjajew. *A Concise Handbook of Mathematics*. Defense Technical Information Center, 1968.

[15] K Varju, Y Mairesse, B Carre, MB Gaarde, P Johnsson, S Kazamias, R Lopez-Martens, J Mauritsson, KJ Schafer, PH Balcou, A L'Huillier, and P Salieres. Frequency chirp of harmonic and attosecond pulses. *Journal of Modern Optics*, 52(2-3):379–394, JAN-FEB 2005.

[16] E. Wigner. On the quantum correction for thermodynamic equilibrium. *Phys. Rev.*, 40:749–759, Jun 1932.

[17] D. Gabor. Theory of communication. *J. Inst. Electr. Engineering (London)*, 93:429–457, 1946.

[18] Soo-Chang Pei and Jian-Jiun Ding. Relations between gabor transforms and fractional fourier transforms and their applications for signal processing. *Signal Processing, IEEE Transactions on*, 55(10):4839–4850, Oct 2007.

[19] Dawid Attwood. *Soft x-rays and extreme ultraviolet radiation*. Cambridge University Press, 2007.

[20] M. Harmand, R. Coffee, M. R. Bionta, M. Chollet, D. French, D. Zhu, D. M. Fritz, H. T. Lemke, N. Medvedev, B. Ziaja, S. Toleikis, and M. Cammarata. Achieving few-femtosecond time-sorting at hard x-ray free-electron lasers. *Nature Photonics*, 7:215–218, 2013.

[21] S. Corde, K. Ta Phuoc, G. Lambert, R. Fitour, V. Malka, A. Rousse, A. Beck, and E. Lefebvre. Femtosecond x rays from laser-plasma accelerators. *Rev. Mod. Phys.*, 85:1–48, Jan 2013.

[22] Eric Esarey, Sally K. Ride, and Phillip Sprangle. Nonlinear thomson scattering of intense laser pulses from beams and plasmas. *Phys. Rev. E*, 48:3003–3021, Oct 1993.

[23] A Paz, S Kuschel, C Rodel, M Schnell, O Jackel, M C Kaluza, and G G Paulus. Thomson backscattering from laser-generated, relativistically moving high-density electron layers. *New Journal of Physics*, 14(9):093018, 2012.

[24] C Thaury and F Quere. High-order harmonic and attosecond pulse generation on plasma mirrors: basic mechanisms. *Journal of Physics B: Atomic, Molecular and Optical Physics*, 43(21):213001, 2010.

[25] F. Quéré, C. Thaury, P. Monot, S. Dobosz, Ph. Martin, J.-P. Geindre, and P. Audebert. Coherent wake emission of high-order harmonics from overdense plasmas. *Phys. Rev. Lett.*, 96:125004, Mar 2006.

[26] Ferenc Krausz and Misha Ivanov. Attosecond physics. *Rev. Mod. Phys.*, 81(1):163–234, Feb 2009.

[27] Manuel Krebs, Steffen Hadrich, Stefan Demmler, Jan Rothhardt, Amelle Zair, Luke Chipperfield, Jens Limpert, and Andreas Tunnermann. Towards isolated attosecond pulses at megahertz repetition rates. *Nature Photonics*, 7:555, 2013.

[28] P Zeitoun, G Faivre, S Sebban, T Mocek, A Hallou, M Fajardo, D Aubert, P Balcou, F Burgy, D Douillet, S Kazamias, G de Lacheze-Murel, T Lefrou, S le Pape, P Mercere, H Merdji, AS Morlens, JP Rousseau, and C Valentin. A high-intensity highly coherent soft x-ray femtosecond laser seeded by a high harmonic beam. *Nature (London)*, 431(7007):426–429, SEP 23 2004.

[29] R Lopez-Martens, K Varju, P Johnsson, J Mauritsson, Y Mairesse, P Salieres, MB Gaarde, KJ Schafer, A Persson, S Svanberg, CG Wahlstrom, and A L'Huillier. Amplitude and phase control of attosecond light pulses. *Phys. Rev. Lett.*, 94(3):033001, JAN 28 2005.

[30] Robert W. Boyd. *Nonlinear Optics, Third Edition.* Academic Press, 2008.

[31] A. McPherson, G. Gibson, H. Jara, U. Johann, T. S. Luk, I. A. McIntyre, K. Boyer, and C. K. Rhodes. Studies of multiphoton production of vacuum-ultraviolet radiation in the rare gases. *J. Opt. Soc. Am. B*, 4(4):595–601, Apr 1987.

[32] M Ferray, A L'Huillier, X F Li, L A Lompre, G Mainfray, and C Manus. Multiple-harmonic conversion of 1064 nm radiation in rare gases. *Journal of Physics B: Atomic, Molecular and Optical Physics*, 21(3):L31, 1988.

[33] P. B. Corkum. Plasma perspective on strong field multiphoton ionization. *Phys. Rev. Lett.*, 71(13):1994–1997, Sep 1993.

[34] K. J. Schafer, Baorui Yang, L. F. DiMauro, and K. C. Kulander. Above threshold ionization beyond the high harmonic cutoff. *Phys. Rev. Lett.*, 70:1599–1602, Mar 1993.

[35] Anne L'Huillier, M. Lewenstein, P. Salières, Ph. Balcou, M. Yu. Ivanov, J. Larsson, and C. G. Wahlström. High-order harmonic-generation cutoff. *Phys. Rev. A*, 48:R3433–R3436, Nov 1993.

[36] Jeffrey L. Krause, Kenneth J. Schafer, and Kenneth C. Kulander. High-order harmonic generation from atoms and ions in the high intensity regime. *Phys. Rev. Lett.*, 68:3535–3538, Jun 1992.

[37] S. G. Preston, A. Sanpera, M. Zepf, W. J. Blyth, C. G. Smith, J. S. Wark, M. H. Key, K. Burnett, M. Nakai, D. Neely, and A. A. Offenberger. High-order harmonics of 248.6-nm krf laser from helium and neon ions. *Phys. Rev. A*, 53:R31–R34, Jan 1996.

[38] C. Dolle, C. Reinhardt, P. Simon, and B. Wellegehausen. Generation of 100 μj pulses at 82.8 nm by frequency tripling of sub-picosecond krf laser radiation. *Applied Physics B*, 75(6-7):629–634, 2002.

[39] C. Dolle, C. Reinhardt, P. Simon, and B. Wellegehausen. Spectral phase matching for highly efficient frequency tripling of short-pulse krf laser radiation in argon. *Applied Physics B*, 76(8):891–895, 2003.

[40] Tenio Popmintchev, Ming-Chang Chen, Alon Bahabad, Michael Gerrity, Pavel Sidorenko, Oren Cohen, Ivan P. Christov, Margaret M. Murnane, and Henry C. Kapteyn. Phase matching of high harmonic generation in the soft and hard x-ray regions of the spectrum. *PNAS*, 106(26):10516–10521, 2009.

[41] Tenio Popmintchev, Ming-Chang Chen, Paul Arpin, Margaret M. Murnane, and Henry C. Kapteyn. The attosecond nonlinear optics of bright coherent x-ray generation. *Nature Photonics*, 4(12):822–832, DEC 2010.

[42] M. Lewenstein, Ph. Balcou, M. Yu. Ivanov, Anne L'Huillier, and P. B. Corkum. Theory of high-harmonic generation by low-frequency laser fields. *Phys. Rev. A*, 49(3):2117–2132, Mar 1994.

[43] Maciej Lewenstein, Pascal Salières, and Anne L'Huillier. Phase of the atomic polarization in high-order harmonic generation. *Phys. Rev. A*, 52(6):4747–4754, Dec 1995.

[44] Zenghu Chang. *Fundamentals of Attosecond Optics*. CRC Press, 2011.

[45] E. H. Hauge and J. A. Støvneng. Tunneling times: a critical review. *Rev. Mod. Phys.*, 61:917–936, Oct 1989.

[46] P. Eckle, A. N. Pfeiffer, C. Cirelli, A. Staudte, R. Dorner, H. G. Muller, M. Buttiker, and U. Keller. Attosecond ionization and tunneling delay time measurements in helium. *Science*, 322(5907):1525–1529, 2008.

[47] Adrian N. Pfeiffer, Claudio Cirelli, Mathias Smolarski, Darko Dimitrovski, Mahmoud Abu-samha, Lars Bojer Madsen, and Ursula Keller. Attoclock reveals natural coordinates of the laser-induced tunnelling current flow in atoms. *Nature Physics*, 8(1):76–80, JAN 2012.

[48] G. Sansone, C. Vozzi, S. Stagira, and M. Nisoli. Nonadiabatic quantum path analysis of high-order harmonic generation: Role of the carrier-envelope phase on short and long paths. *Phys. Rev. A*, 70(1):013411, Jul 2004.

[49] M.V. Fedoryuk (originator). Encyclopedia of mathematics. http://www.encyclopediaofmath.org/index.php?title=Saddle_point_method. retreived on the 29th of October 2013.

[50] A. Erdélyi. *Asymptotic expansion*. Dover Publications Inc., New York, 1956.

[51] J M Dahlstrom, A L'Huillier, and A Maquet. Introduction to attosecond delays in photoionization. *Journal of Physics B: Atomic, Molecular and Optical Physics*, 45(18):183001, 2012.

[52] P. Salieres, B. Carre, L. Le Deroff, F. Grasbon, G. G. Paulus, H. Walther, R. Kopold, W. Becker, D. B. Milosevic, A. Sanpera, and M. Lewenstein. Feynman's path-integral approach for intense-laser-atom interactions. *Science*, 292(5518):902–905, 2001.

[53] C. Granados and L. Plaja. Invalidity of the ehrenfest theorem in the computation of high-order-harmonic generation within the strong-field approximation. *Phys. Rev. A*, 85:053403, May 2012.

[54] Ariel Gordon and Franz X. Kärtner. Quantitative modeling of single atom high harmonic generation. *Phys. Rev. Lett.*, 95:223901, Nov 2005.

[55] John W. Cooper. Photoionization from outer atomic subshells. a model study. *Phys. Rev.*, 128:681–693, Oct 1962.

[56] J. Higuet, H. Ruf, N. Thiré, R. Cireasa, E. Constant, E. Cormier, D. Descamps, E. Mével, S. Petit, B. Pons, Y. Mairesse, and B. Fabre. High-order harmonic spectroscopy of the cooper minimum in argon: Experimental and theoretical study. *Phys. Rev. A*, 83:053401, May 2011.

[57] Anh-Thu Le, Toru Morishita, and C. D. Lin. Extraction of the species-dependent dipole amplitude and phase from high-order harmonic spectra in rare-gas atoms. *Phys. Rev. A*, 78:023814, Aug 2008.

[58] Anh-Thu Le, R. R. Lucchese, S. Tonzani, T. Morishita, and C. D. Lin. Quantitative rescattering theory for high-order harmonic generation from molecules. *Phys. Rev. A*, 80:013401, Jul 2009.

[59] J. Perez-Hernandez, J. Ramos, L. Roso, and L. Plaja. Harmonic generation beyond the strong-field approximation: Phase and temporal description. *Laser Physics*, 20:1044–1050, 2010.

[60] C. C. Chirila, I. Dreissigacker, E. V. van der Zwan, and M. Lein. Emission times in high-order harmonic generation. *Phys. Rev. A*, 81:033412, Mar 2010.

[61] Y. Mairesse, A. de Bohan, L. J. Frasinski, H. Merdji, L. C. Dinu, P. Monchicourt, P. Breger, M. Kovacev, R. Taieb, B. Carre, H. G. Muller, P. Agostini, and P. Salieres. Attosecond synchronization of high-harmonic soft x-rays. *Science*, 302(5650):1540–1543, 2003.

[62] Dror Shafir, Hadas Soifer, Barry D. Bruner, Michal Dagan, Yann Mairesse, Serguei Patchkovskii, Misha Yu. Ivanov, Olga Smirnova, and Nirit Dudovich. Resolving the time when an electron exits a tunnelling barrier. *Nature*, 485(7398):343–346, MAY 17 2012.

[63] Mette B Gaarde, Jennifer L Tate, and Kenneth J Schafer. Macroscopic aspects of attosecond pulse generation. *J.Phys. B: At, Mol. and Opt. Phys.*, 41(13):132001, 2008.

[64] Philippe Balcou, Pascal Saliéres, Anne L'Huillier, and Maciej Lewenstein. Generalized phase-matching conditions for high harmonics: The role of field-gradient forces. *Phys. Rev. A*, 55(4):3204–3210, Apr 1997.

[65] Matt Landreman, Kevin O'Keeffe, Tom Robinson, Matt Zepf, Brendan Dromey, and Simon M. Hooker. Comparison of parallel and perpendicular polarized counterpropagating light for suppressing high harmonic generation. *J. Opt. Soc. Am. B*, 24(9):2421–2427, Sep 2007.

[66] M. Bellini, C. Lyngå, A. Tozzi, M. B. Gaarde, T. W. Hänsch, A. L'Huillier, and C.-G. Wahlström. Temporal coherence of ultrashort high-order harmonic pulses. *Phys. Rev. Lett.*, 81:297–300, Jul 1998.

[67] H. Merdji, M. Kovačev, W. Boutu, P. Salières, F. Vernay, and B. Carré. Macroscopic control of high-order harmonics quantum-path components for the generation of attosecond pulses. *Phys. Rev. A*, 74:043804, Oct 2006.

[68] Eugene Hecht. *Optics*. Addison Wesley, 4th edition edition, 2002.

[69] T. Ruchon, C. P. Hauri, K. Varju, E. Mansten, M. Swoboda, R. Lopez-Martens, and A. L'Huillier. Macroscopic effects in attosecond pulse generation. *New Journal of Physics*, 10:025027, FEB 29 2008.

[70] P. D. Maker, R. W. Terhune, M. Nisenoff, and C. M. Savage. Effects of dispersion and focusing on the production of optical harmonics. *Phys. Rev. Lett.*, 8:21–22, Jan 1962.

[71] B.L. Henke, E.M. Gullikson, and J.C. Davis. X-ray interactions: Photoabsorption, scattering, transmission, and reflection at e = 50-30,000 ev, z = 1-92. *Atomic Data and Nuclear Data Tables*, 54(2):181 – 342, 1993.

[72] C. T. Chantler. Theoretical form factor, attenuation, and scattering tabulation for z=1-92 from e=1-10 ev to e=0.4-1.0 mev. *Journal of Physical and Chemical Reference Data*, 24(1):71–643, 1995.

[73] C. T. Chantler. Detailed tabulation of atomic form factors, photoelectric absorption and scattering cross section, and mass attenuation coefficients in the vicinity of absorption edges in the soft x-ray (z=30-36, z=60-89, e=0.1 kev-10 kev), addressing convergence issues of earlier work. *Journal of Physical and Chemical Reference Data*, 29(4):597–1056, 2000.

[74] C.T. Chantler, K. Olsen, R.A. Dragoset, J. Chang, A.R. Kishore, S.A. Kotochigova, and D.S. Zucker. X-ray form factor, attenuation, and scattering tables. http://www.nist.gov/pml/data/ffast/. retreived on the 29th of May 2012.

[75] A. Börzsönyi, Z. Heiner, M. P. Kalashnikov, A. P. Kovács, and K. Osvay. Dispersion measurement of inert gases and gas mixtures at 800 nm. *Appl. Opt.*, 47(27):4856–4863, Sep 2008.

[76] A. E. Siegman. *Lasers*, chapter 16, page 626. University Science Books, 1986.

[77] P. Rudawski, C. M. Heyl, F. Brizuela, J. Schwenke, A. Persson, E. Mansten, R. Rakowski, L. Rading, F. Campi, B. Kim, P. Johnsson, and A. L'Huillier. A high-flux high-order harmonic source. *Review of Scientific Instruments*, 84(7):073103, 2013.

[78] J. Tate, T. Auguste, H. G. Muller, P. Salières, P. Agostini, and L. F. DiMauro. Scaling of wave-packet dynamics in an intense midinfrared field. *Phys. Rev. Lett.*, 98(1):013901, Jan 2007.

[79] A. D. Shiner, C. Trallero-Herrero, N. Kajumba, H.-C. Bandulet, D. Comtois, F. Légaré, M. Giguère, J-C. Kieffer, P. B. Corkum, and D. M. Villeneuve. Wavelength scaling of high harmonic generation efficiency. *Phys. Rev. Lett.*, 103:073902, Aug 2009.

[80] Giuseppe Sansone, Luca Poletto, and Mauro Nisoli. High-energy attosecond light sources. *Nature Photonics*, 5(11):656–664, NOV 2011.

[81] S. Kazamias, D. Douillet, F. Weihe, C. Valentin, A. Rousse, S. Sebban, G. Grillon, F. Augé, D. Hulin, and Ph. Balcou. Global optimization of high harmonic generation. *Phys. Rev. Lett.*, 90:193901, May 2003.

[82] C M Heyl, J Gudde, A L'Huillier, and U Hofer. High-order harmonic generation with microj laser pulses at high repetition rates. *Journal of Physics B: Atomic, Molecular and Optical Physics*, 45(7):074020, 2012.

[83] A. Paul, E.A. Gibson, Xiaoshi Zhang, A. Lytle, T. Popmintchev, Xibin Zhou, M.M. Murnane, I.P. Christov, and H.C. Kapteyn. Phase-matching techniques for coherent soft x-ray generation. *Quantum Electronics, IEEE Journal of*, 42(1):14 – 26, jan. 2006.

[84] Charles G. Durfee, Andy R. Rundquist, Sterling Backus, Catherine Herne, Margaret M. Murnane, and Henry C. Kapteyn. Phase matching of high-order harmonics in hollow waveguides. *Phys. Rev. Lett.*, 83:2187–2190, Sep 1999.

[85] E. Constant, D. Garzella, P. Breger, E. Mével, Ch. Dorrer, C. Le Blanc, F. Salin, and P. Agostini. Optimizing high harmonic generation in absorbing gases: Model and experiment. *Phys. Rev. Lett.*, 82(8):1668–1671, Feb 1999.

[86] J. A. Armstrong, N. Bloembergen, J. Ducuing, and P. S. Pershan. Interactions between light waves in a nonlinear dielectric. *Phys. Rev.*, 127:1918–1939, Sep 1962.

[87] Carles Serrat and Jens Biegert. All-regions tunable high harmonic enhancement by a periodic static electric field. *Phys. Rev. Lett.*, 104(7):073901, Feb 2010.

[88] Xiaoshi Zhang, Amy L. Lytle, Tenio Popmintchev, Xibin Zhou, Henry C. Kapteyn, Margaret M. Murnane, and Oren Cohen. Quasi-phase-matching and quantum-path control of high-harmonic generation using counterpropagating light. *Nature Physics*, 3(4):270–275, APR 2007.

[89] Oren Cohen, Xiaoshi Zhang, Amy L. Lytle, Tenio Popmintchev, Margaret M. Murnane, and Henry C. Kapteyn. Grating-assisted phase matching in extreme nonlinear optics. *Phys. Rev. Lett.*, 99:053902, Jul 2007.

[90] Oren Cohen, Amy L. Lytle, Xiaoshi Zhang, Margaret M. Murnane, and Henry C. Kapteyn. Optimizing quasi-phase matching of high harmonic generation using counterpropagating pulse trains. *Opt. Lett.*, 32(20):2975–2977, Oct 2007.

[91] Amy L. Lytle, Xiaoshi Zhang, Richard L. Sandberg, Oren Cohen, Henry C. Kapteyn, and Margaret M. Murnane. Quasi-phase matching and characterization of high-order harmonic generation in hollow waveguides using counterpropagating light. *Opt. Express*, 16(9):6544–6566, Apr 2008.

[92] P. L. Shkolnikov, A. Lago, and A. E. Kaplan. Optimal quasi-phase-matching for high-order harmonic generation in gases and plasma. *Phys. Rev. A*, 50:R4461–R4464, Dec 1994.

[93] M. Geissler, G. Tempea, and T. Brabec. Phase-matched high-order harmonic generation in the nonadiabatic limit. *Phys. Rev. A*, 62(3):033817, Aug 2000.

[94] T. Auguste, B. Carré, and P. Salières. Quasi-phase-matching of high-order harmonics using a modulated atomic density. *Phys. Rev. A*, 76:011802, Jul 2007.

[95] V Tosa, V S Yakovlev, and F Krausz. Generation of tunable isolated attosecond pulses in multi-jet systems. *New Journal of Physics*, 10(2):025016, 2008.

[96] J Biegert, A Heinrich, CP Hauri, W Kornelis, P Schlup, M Anscombe, KJ Schafer, MB Gaarde, and U Keller. Enhancement of high-order harmonic emission using attosecond pulse trains. *Laser Physics*, 15(6):899–902, JUN 2005.

[97] J Biegert, A Heinrich, CP Hauri, W Kornelis, P Schlup, MP Anscombe, MB Gaarde, KJ Schafer, and U Keller. Control of high-order harmonic emission using attosecond pulse trains. *Journal of Modern Optics*, 53(1-2):87–96, JAN 20 2006.

[98] Kenneth J. Schafer, Mette B. Gaarde, Arne Heinrich, Jens Biegert, and Ursula Keller. Strong field quantum path control using attosecond pulse trains. *Phys. Rev. Lett.*, 92:023003, Jan 2004.

[99] Mette B. Gaarde, Kenneth J. Schafer, Arne Heinrich, Jens Biegert, and Ursula Keller. Large enhancement of macroscopic yield in attosecond pulse train-assisted harmonic generation. *Phys. Rev. A*, 72:013411, Jul 2005.

[100] J. Seres, V. S. Yakovlev, E. Seres, Ch. Streli, P. Wobrauschek, Ch. Spielmann, and F. Krausz. Coherent superposition of laser-driven soft-x-ray harmonics from successive sources. *Nature Physics*, 3(12):878–883, 2007.

[101] A. Willner, F. Tavella, M. Yeung, T. Dzelzainis, C. Kamperidis, M. Bakarezos, D. Adams, M. Schulz, R. Riedel, M. C. Hoffmann, W. Hu, J. Rossbach, M. Drescher, N. A. Papadogiannis, M. Tatarakis, B. Dromey, and M. Zepf. Coherent control of high harmonic generation via dual-gas multijet arrays. *Phys. Rev. Lett.*, 107:175002, Oct 2011.

[102] A Willner, F Tavella, M Yeung, T Dzelzainis, C Kamperidis, M Bakarezos, D Adams, R Riedel, M Schulz, M C Hoffmann, W Hu, J Rossbach, M Drescher, V S Yakovlev, N A Papadogiannis, M Tatarakis, B Dromey, and M Zepf. Efficient control of quantum paths via dual-gas high harmonic generation. *New Journal of Physics*, 13(11):113001, 2011.

[103] Ivan Christov, Henry Kapteyn, and Margaret Murnane. Quasi-phase matching of high-harmonics and attosecond pulses in modulated waveguides. *Opt. Express*, 7(11):362–367, Nov 2000.

[104] Daniele Faccio, Carles Serrat, José M. Cela, Albert Farrés, Paolo Di Trapani, and Jens Biegert. Modulated phase matching and high-order harmonic enhancement mediated by the carrier-envelope phase. *Phys. Rev. A*, 81:011803, Jan 2010.

[105] A Paul, RA Bartels, R Tobey, H Green, S Weiman, IP Christov, MM Murnane, HC Kapteyn, and S Backus. Quasi-phase-matched generation of coherent extreme-ultraviolet light. *Nature*, 421(6918):51–54, JAN 2 2003.

[106] EA Gibson, A Paul, N Wagner, R Tobey, D Gaudiosi, S Backus, IP Christov, A Aquila, EM Gullikson, DT Attwood, MM Murnane, and HC Kapteyn. Coherent soft x-ray generation in the water window with quasi-phase matching. *Science*, 302(5642):95–98, 2003.

[107] Xiaoshi Zhang, Amy Lytle, Tenio Popmintchev, Ariel Paul, Nick Wagner, Margaret Murnane, Henry Kapteyn, and Ivan P. Christov. Phase matching, quasi-phase matching, and pulse compression in a single waveguide for enhanced high-harmonic generation. *Opt. Lett.*, 30(15):1971–1973, Aug 2005.

[108] M. Zepf, B. Dromey, M. Landreman, P. Foster, and S. M. Hooker. Bright quasi-phase-matched soft-x-ray harmonic radiation from argon ions. *Phys. Rev. Lett.*, 99:143901, Oct 2007.

[109] B. Dromey, M. Zepf, M. Landreman, and S. M. Hooker. Quasi-phasematching of harmonic generation via multimode beating in waveguides. *Opt. Express*, 15(13):7894–7900, Jun 2007.

[110] A. V. Birulin, V. T. Platonenko, and V. V. Strelkov. High-harmonic generation in interfering waves. *Journal of Experimental and Theoretical Physics*, 83(1):33–38, July 1996.

[111] Justin Peatross, Sergei Voronov, and I. Prokopovich. Selective zoning of high harmonic emission using counter-propagating light. *Opt. Express*, 1(5):114–125, Sep 1997.

[112] C. Serrat and J. Biegert. Enhancement of hhg yield. *NIMA*, 653(1):134 – 136, 2011.

[113] M.M. Fejer, G.A. Magel, D.H. Jundt, and R.L. Byer. Quasi-phase-matched second harmonic generation: tuning and tolerances. *Quantum Electronics, IEEE Journal of*, 28(11):2631–2654, nov 1992.

[114] H. Ren, A. Nazarkin, J. Nold, and Philip S. Russell. Quasi-phase-matched high harmonic generation in hollow core photonic crystal fibers. *Opt. Express*, 16(21):17052–17059, Oct 2008.

[115] S. L. Voronov, I. Kohl, J. B. Madsen, J. Simmons, N. Terry, J. Titensor, Q. Wang, and J. Peatross. Control of laser high-harmonic generation with counterpropagating light. *Phys. Rev. Lett.*, 87:133902, Sep 2001.

[116] Julia Sutherland, E. Christensen, N. Powers, S. Rhynard, J. Painter, and J. Peatross. High harmonic generation in a semi-infinite gas cell. *Opt. Express*, 12(19):4430–4436, Sep 2004.

[117] Tom Robinson, Kevin O'Keeffe, Matt Zepf, Brendan Dromey, and Simon M. Hooker. Generation and control of ultrafast pulse trains for quasi-phase-matching high-harmonic generation. *J. Opt. Soc. Am. B*, 27(4):763–772, Apr 2010.

[118] Pavel Sidorenko, Maxim Kozlov, Alon Bahabad, Tenio Popmintchev, Margaret Murnane, Henry Kapteyn, and Oren Cohen. Sawtooth grating-assisted phase-matching. *Opt. Express*, 18(22):22686–22692, Oct 2010.

[119] S. Kazamias, D. Douillet, C. Valentin, F. Weihe, F. Augé, Th. Lefrou, G. Grillon, S. Sebban, and Ph. Balcou. Observation of high-contrast coherence fringes in high-order harmonic generation. *Phys. Rev. A*, 68:033819, Sep 2003.

[120] A. L. Lytle, X. Zhang, J. Peatross, M. M. Murnane, H. C. Kapteyn, and O. Cohen. Probe of high-order harmonic generation in a hollow waveguide geometry using counterpropagating light. *Phys. Rev. Lett.*, 98:123904, Mar 2007.

[121] Kevin O'Keeffe, Tom Robinson, and Simon M. Hooker. Quasi-phase-matching high harmonic generation using trains of pulses produced using an array of birefringent plates. *Opt. Express*, 20(6):6236–6247, Mar 2012.

[122] E. Priori, G. Cerullo, M. Nisoli, S. Stagira, S. De Silvestri, P. Villoresi, L. Poletto, P. Ceccherini, C. Altucci, R. Bruzzese, and C. de Lisio. Nonadiabatic three-dimensional model of high-order harmonic generation in the few-optical-cycle regime. *Phys. Rev. A*, 61(6):063801, May 2000.

[123] Eiji Takahashi, Valer Tosa, Yasuo Nabekawa, and Katsumi Midorikawa. Experimental and theoretical analyses of a correlation between pump-pulse propagation and harmonic yield in a long-interaction medium. *Phys. Rev. A*, 68(2):023808, Aug 2003.

[124] V. Tosa, H. T. Kim, I. J. Kim, and C. H. Nam. High-order harmonic generation by chirped and self-guided femtosecond laser pulses. i. spatial and spectral analysis. *Phys. Rev. A*, 71(6):063807, Jun 2005.

[125] V. Tosa, H. T. Kim, I. J. Kim, and C. H. Nam. High-order harmonic generation by chirped and self-guided femtosecond laser pulses. ii. time-frequency analysis. *Phys. Rev. A*, 71(6):063808, Jun 2005.

[126] John Crank and Phyllis Nicolson. A practical method for numerical evaluation of solutions of partial differential equations of the heat conduction type. *Proc. Camb. Phil. Soc.*, 43:50–67, 1947.

[127] J. Crank and P. Nicolson. A practical method for numerical evaluation of solutions of partial differential equations of the heat-conduction type. *Advances in Computational Mathematics*, 6(1):207–226, 1996.

[128] William H. Press, Saul A. Teukolsky, William T. Vetterling, and Brian P. Flannery. *Numerical recipes*, chapter 20, pages 1043–1048. Cambridge University Press, 2007.

[129] Anne L'Huillier, Philippe Balcou, Sebastien Candel, Kenneth J. Schafer, and Kenneth C. Kulander. Calculations of high-order harmonic-generation processes in xenon at 1064 nm. *Phys. Rev. A*, 46(5):2778–2790, Sep 1992.

[130] Ian A. Walmsley and Victor Wong. Characterization of the electric field of ultrashort optical pulses. *J. Opt. Soc. Am. B*, 13(11):2453–2463, Nov 1996.

[131] P Tzallas, D Charalambidis, NA Papadogiannis, K Witte, and GD Tsakiris. Direct observation of attosecond light bunching. *Nature*, 426(6964):267–271, NOV 20 2003.

[132] Yasuo Nabekawa, Toshihiko Shimizu, Tomoya Okino, Kentaro Furusawa, Hirokazu Hasegawa, Kaoru Yamanouchi, and Katsumi Midorikawa. Conclusive evidence of an attosecond pulse train observed with the mode-resolved autocorrelation technique. *Phys. Rev. Lett.*, 96:083901, Feb 2006.

[133] P. Tzallas, E. Skantzakis, L. A. A. Nikolopoulos, G. D. Tsakiris, and D. Charalambidis. Extreme-ultraviolet pump-probe studies of one-femtosecond-scale electron dynamics. *Nature Physics*, 7(10):781–784, 2011.

[134] Eiji J. Takahashi, Pengfei Lan, Oliver D. Mucke, Yasuo Nabekawa, and Katsumi Midorikawa. Attosecond nonlinear optics using gigawatt-scale isolated attosecond pulses. *Nature Communications*, 4:2691, 2013.

[135] P. M. Paul, E. S. Toma, P. Breger, G. Mullot, F. Augé, Ph. Balcou, H. G. Muller, and P. Agostini. Observation of a train of attosecond pulses from high harmonic generation. *Science*, 292(5522):1689–1692, 2001.

[136] M Hentschel, R Kienberger, C Spielmann, GA Reider, N Milosevic, T Brabec, P Corkum, U Heinzmann, M Drescher, and F Krausz. Attosecond metrology. *Nature*, 414(6863):509–513, NOV 29 2001.

[137] E S Toma and H G Muller. Calculation of matrix elements for mixed extreme-ultraviolet–infrared two-photon above-threshold ionization of argon. *Journal of Physics B: Atomic, Molecular and Optical Physics*, 35(16):3435, 2002.

[138] K Varju, P Johnsson, R Lopez-Martens, T Remetter, E Gustafsson, J Mauritsson, MB Gaarde, KJ Schafer, C Erny, I Sola, A Zair, E Constant, E Cormier, E Mevel, and A L'Huillier. Experimental studies of attosecond pulse trains. *Laser Physics*, 15(6):888–898, JUN 2005.

[139] C. J. Foot. *Atomic physics*. Oxford University Press, 2005.

[140] Eugene P. Wigner. Lower limit for the energy derivative of the scattering phase shift. *Phys. Rev.*, 98:145–147, Apr 1955.

[141] K. Klunder, J. M. Dahlstrom, M. Gisselbrecht, T. Fordell, M. Swoboda, D. Guenot, P. Johnsson, J. Caillat, J. Mauritsson, A. Maquet, R. Taieb, and A. L'Huillier. Probing single-photon ionization on the attosecond time scale. *Phys. Rev. Lett.*, 106:143002, Apr 2011.

[142] R. Bourgain, J. Pellegrino, S. Jennewein, Y. R. P. Sortais, and A. Browaeys. Direct measurement of the wigner time delay for the scattering of light by a single atom. *Opt. Lett.*, 38(11):1963–1965, Jun 2013.

[143] M. Schultze, M. Fieß, N. Karpowicz, J. Gagnon, M. Korbman, M. Hofstetter, S. Neppl, A. L. Cavalieri, Y. Komninos, Th. Mercouris, C. A. Nicolaides, R. Pazourek, S. Nagele, J. Feist, J. Burgdörfer, A. M. Azzeer, R. Ernstorfer, R. Kienberger, U. Kleineberg, E. Goulielmakis, F. Krausz, and V. S. Yakovlev. Delay in photoemission. *Science*, 328(5986):1658–1662, 2010.

[144] Misha Ivanov and Olga Smirnova. How accurate is the attosecond streak camera? *Phys. Rev. Lett.*, 107:213605, Nov 2011.

[145] K Varju, Y Mairesse, P Agostini, P Breger, B Carre, LJ Frasinski, E Gustafsson, P Johnsson, J Mauritsson, H Merdji, P Monchicourt, A L'Huillier, and P Salieres. Reconstruction of attosecond pulse trains using an adiabatic phase expansion. *Phys. Rev. Lett.*, 95(24):243901, DEC 9 2005.

[146] Y. Mairesse and F. Quéré. Frequency-resolved optical gating for complete reconstruction of attosecond bursts. *Phys. Rev. A*, 71:011401, Jan 2005.

[147] G. Laurent, W. Cao, H. Li, Z. Wang, I. Ben-Itzhak, and C. L. Cocke. Attosecond control of orbital parity mix interferences and the relative phase of even and odd harmonics in an attosecond pulse train. *Phys. Rev. Lett.*, 109:083001, Aug 2012.

[148] G. Laurent, W. Cao, I. Ben-Itzhak, and C. L. Cocke. Attosecond pulse characterization. *Opt. Express*, 21(14):16914–16927, Jul 2013.

[149] E. Goulielmakis, M. Schultze, M. Hofstetter, V. S. Yakovlev, J. Gagnon, M. Uiberacker, A. L. Aquila, E. M. Gullikson, D. T. Attwood, R. Kienberger, F. Krausz, and U. Kleineberg. Single-cycle nonlinear optics. *Science*, 320(5883):1614–1617, 2008.

[150] Kun Zhao, Qi Zhang, Michael Chini, Yi Wu, Xiaowei Wang, and Zenghu Chang. Tailoring a 67 attosecond pulse through advantageous phase-mismatch. *Opt. Lett.*, 37(18):3891–3893, Sep 2012.

[151] Tenio Popmintchev, Ming-Chang Chen, Dimitar Popmintchev, Paul Arpin, Susannah Brown, Skirmantas Alisauskas, Giedrius Andriukaitis, Tadas Balciunas, Oliver D. Mucke, Audrius Pugzlys, Andrius Baltuska, Bonggu Shim, Samuel E. Schrauth, Alexander Gaeta, Carlos Hernandez-Garcia, Luis Plaja, Andreas Becker, Agnieszka Jaron-Becker, Margaret M. Murnane, and Henry C. Kapteyn. Bright coherent ultrahigh harmonics in the kev x-ray regime from mid-infrared femtosecond lasers. *Science*, 336(6086):1287–1291, 2012.

[152] Arthur K Mills, T J Hammond, Matthew H C Lam, and David J Jones. Xuv frequency combs via femtosecond enhancement cavities. *Journal of Physics B: Atomic, Molecular and Optical Physics*, 45(14):142001, 2012.

[153] F. Calegari, C. Vozzi, M. Negro, G. Sansone, F. Frassetto, L. Poletto, P. Villoresi, M. Nisoli, S. De Silvestri, and S. Stagira. Efficient continuum generation exceeding 200 ev by intense ultrashort two-color driver. *Opt. Lett.*, 34(20):3125–3127, Oct 2009.

[154] Eiji J. Takahashi, Pengfei Lan, Oliver D. Mücke, Yasuo Nabekawa, and Katsumi Midorikawa. Infrared two-color multicycle laser field synthesis for generating an intense attosecond pulse. *Phys. Rev. Lett.*, 104:233901, Jun 2010.

[155] Alexander Sell, Alfred Leitenstorfer, and Rupert Huber. Phase-locked generation and field-resolved detection of widely tunable terahertz pulses with amplitudes exceeding 100 mv/cm. *Opt. Lett.*, 33(23):2767–2769, Dec 2008.

[156] DB Milosevic and AF Starace. Control of high-harmonic generation and laser-assisted x-ray atom scattering with static electric and magnetic fields. *Laser Physics*, 10(1):278–293, 2000.

[157] Songsong Tang, Li Zheng, and Xianfeng Chen. Approach to extreme ultraviolet supercontinuum in a two-color laser field. *Optics Communications*, 283(1):155–159, JAN 1 2010.

[158] Min Qi Bao and Anthony F. Starace. Static-electric-field effects on high harmonic generation. *Phys. Rev. A*, 53(6):R3723–R3726, Jun 1996.

[159] Bingbing Wang, Xiaofeng Li, and Panming Fu. The effects of a static electric field on high-order harmonic generation. *Journal of Physics B: Atomic, Molecular and Optical Physics*, 31(9):1961, 1998.

[160] Vladimir D. Taranukhin and Nickolay Yu. Shubin. High-order harmonic generation by atoms with strong high-frequency and low-frequency pumping. *J. Opt. Soc. Am. B*, 17(9):1509–1516, Sep 2000.

[161] Weiyi Hong, Peixiang Lu, Pengfei Lan, Qingbin Zhang, and Xinbing Wang. Few-cycle attosecond pulses with stabilized-carrier-envelope phase in the presence of a strong terahertz field. *Opt. Express*, 17(7):5139–5146, Mar 2009.

[162] Yang Xiang, Yueping Niu, and Shangqing Gong. Control of the high-order harmonics cutoff through the combination of a chirped laser and static electric field. *Phys. Rev. A*, 79(5):053419, May 2009.

[163] Chang-Long Xia, Gang-Tai Zhang, Jie Wu, and Xue-Shen Liu. Single attosecond pulse generation in an orthogonally polarized two-color laser field combined with a static electric field. *Phys. Rev. A*, 81(4):043420, Apr 2010.

[164] Liqiang Feng and Tianshu Chu. Quantum path control on the harmonic emission in the presence of a terahertz field. *Chemical Physics*, 405(0):26 – 31, 2012.

[165] Katalin Varju, Per Johnsson, Johan Mauritsson, Anne L'Huillier, and Rodrigo Lopez-Martens. Physics of attosecond pulses produced via high harmonic generation. *American Journal of Physics*, 77(5):389–395, MAY 2009.

[166] Z. Chang, A. Rundquist, H. Wang, I. Christov, H. C. Kapteyn, and M. M. Murnane. Temporal phase control of soft-x-ray harmonic emission. *Phys. Rev. A*, 58:R30–R33, Jul 1998.

[167] C. Bourassin-Bouchet, Z. Diveki, S. de Rossi, E. English, E. Meltchakov, O. Gobert, D. Guénot, B. Carré, F. Delmotte, P. Salières, and T. Ruchon. Control of the attosecond synchronization of xuv radiation with phase-optimized mirrors. *Opt. Express*, 19(4):3809–3817, Feb 2011.

[168] Mark Mero, Fabio Frassetto, Paolo Villoresi, Luca Poletto, and Katalin Varjú. Compression methods for xuv attosecond pulses. *Opt. Express*, 19(23):23420–23428, Nov 2011.

[169] Pascal Salières, Anne L'Huillier, and Maciej Lewenstein. Coherence control of high-order harmonics. *Phys. Rev. Lett.*, 74:3776–3779, May 1995.

[170] Y. Mairesse, A. de Bohan, L. J. Frasinski, H. Merdji, L. C. Dinu, P. Monchicourt, P. Breger, M. Kovačev, T. Auguste, B. Carré, H. G. Muller, P. Agostini, and P. Salières. Optimization of attosecond pulse generation. *Phys. Rev. Lett.*, 93(16):163901, Oct 2004.

[171] E. Gustafsson, T. Ruchon, M. Swoboda, T. Remetter, E. Pourtal, R. Lopez-Martens, Ph. Balcou, and A. L'Huillier. Broadband attosecond pulse shaping. *Optics Letters*, 32(11):1353–1355, JUN 1 2007.

[172] A. Wirth, M. Th. Hassan, I. Grguras, J. Gagnon, A. Moulet, T. T. Luu, S. Pabst, R. Santra, Z. A. Alahmed, A. M. Azzeer, V. S. Yakovlev, V. Pervak, F. Krausz, and E. Goulielmakis. Synthesized light transients. *Science*, 334(6053):195–200, 2011.

[173] Shu-Wei Huang, Giovanni Cirmi, Jeffrey Moses, Kyung-Han Hong, Siddharth Bhardwaj, Jonathan R Birge, Li-Jin Chen, Irina V Kabakova, Enbang Li, Benjamin J Eggleton, Giulio Cerullo, and Franz X Kärtner. Optical waveform synthesizer and its application to high-harmonic generation. *Journal of Physics B: Atomic, Molecular and Optical Physics*, 45(7):074009, 2012.

[174] L Roos, M B Gaarde, and A L'Huillier. Tailoring harmonic radiation to different applications using a genetic algorithm. *Journal of Physics B: Atomic, Molecular and Optical Physics*, 34(24):5041, 2001.

[175] Xi Chu and Shih-I Chu. Optimization of high-order harmonic generation by genetic algorithm and wavelet time-frequency analysis of quantum dipole emission. *Phys. Rev. A*, 64:021403, Jul 2001.

[176] Ido Schaefer and Ronnie Kosloff. Optimal-control theory of harmonic generation. *Phys. Rev. A*, 86:063417, Dec 2012.

[177] I. P. Christov, R. Bartels, H. C. Kapteyn, and M. M. Murnane. Attosecond time-scale intra-atomic phase matching of high harmonic generation. *Phys. Rev. Lett.*, 86:5458–5461, Jun 2001.

[178] I. A. Ivanov and A. S. Kheifets. Tailoring the waveforms to extend the high-order harmonic generation cutoff. *Phys. Rev. A*, 80:023809, Aug 2009.

[179] Zhao Di and Li Fu-Li. Extension of high-order harmonic cutoff frequency by synthesizing the waveform of a laser field via the optimization of classical electron trajectory in the laser field. *Chinese Physics B*, 22(6):064215, 2013.

[180] A. Ben Haj Yedder, C. Le Bris, O. Atabek, S. Chelkowski, and A. D. Bandrauk. Optimal control of attosecond pulse synthesis from high-order harmonic generation. *Phys. Rev. A*, 69:041802, Apr 2004.

[181] R Bartels, S Backus, E Zeek, L Misoguti, G Vdovin, IP Christov, MM Murnane, and HC Kapteyn. Shaped-pulse optimization of coherent emission of high-harmonic soft x-rays. *Nature (London)*, 406(6792):164–166, JUL 13 2000.

[182] Randy A. Bartels, Margaret M. Murnane, Henry C. Kapteyn, Ivan Christov, and Herschel Rabitz. Learning from learning algorithms: Application to attosecond dynamics of high-harmonic generation. *Phys. Rev. A*, 70:043404, Oct 2004.

[183] Carsten Winterfeldt, Christian Spielmann, and Gustav Gerber. Colloquium: Optimal control of high-harmonic generation. *Rev. Mod. Phys.*, 80:117–140, Jan 2008.

[184] R. Spitzenpfeil, S. Eyring, C. Kern, C. Ott, J. Lohbreier, J. Henneberger, N. Franke, S. Jung, D. Walter, M. Weger, C. Winterfeldt, T. Pfeifer, and C. Spielmann. Enhancing the brilliance of high-harmonic generation. *Applied Physics A*, 96(1):69–81, 2009.

[185] Katalin Kovacs and Valer Tosa. Quantum trajectories of electrons in arbitrary laser fields. *Journal of Modern Optics*, 57(11):977–983, 2010.

[186] Matteo Lucchini, Francesca Calegari, Kyungseung Kim, Giuseppe Sansone, and Mauro Nisoli. Nonadiabatic quantum path analysis of the high-order harmonic generation in a highly ionized medium. *New Journal of Physics*, 14(3):033009, 2012.

[187] M.V. Ammosov, N.B. Delone, and V.P. Krainov. Tunnel ionization of complex atoms and of atomic ions in an alternating electromagnetic field. *Journal of Experimental and Theoretical Physics*, 64:1191, 1986.

[188] Ivan Christov. Propagation of ultrashort pulses in gaseous medium:breakdown of the quasistatic approximation. *Opt. Express*, 6(2):34–39, Jan 2000.

[189] Mette B. Gaarde and Kenneth J. Schafer. Space-time considerations in the phase locking of high harmonics. *Phys. Rev. Lett.*, 89:213901, Oct 2002.

[190] Jing Miao, Zhinan Zeng, Peng Liu, Yinghui Zheng, Ruxin Li, Zhizhan Xu, V. T. Platonenko, and V. V. Strelkov. Generation of two attosecond pulses with tunable delay using orthogonally-polarized chirped laser pulses. *Opt. Express*, 20(5):5196–5203, Feb 2012.

[191] Eiji J. Takahashi, Tsuneto Kanai, Kenichi L. Ishikawa, Yasuo Nabekawa, and Katsumi Midorikawa. Coherent water window x ray by phase-matched high-order harmonic generation in neutral media. *Phys. Rev. Lett.*, 101(25):253901, Dec 2008.

[192] Tzvi Diskin and Oren Cohen. Quasi-phase-matching of only even-order high harmonics. *Opt. Express*, 22(6):7145–7153, Mar 2014.

[193] József András Fülöp, László Pálfalvi, Matthias C. Hoffmann, and János Hebling. Towards generation of mj-level ultrashort thz pulses by optical rectification. *Optics Express*, 19(16):15090–15097, Aug 2011.

[194] J. A. Fülöp, L. Pálfalvi, S. Klingebiel, G. Almási, F. Krausz, S. Karsch, and J. Hebling. Generation of sub-mj terahertz pulses by optical rectification. *Opt. Lett.*, 37(4):557–559, Feb 2012.

[195] L. V. Keldysh. Ionization in the field of a strong electromagnetic wave. *Zh. Eksp. Teor. Fiz.*, 47:1945–1957, 1964.

[196] S F J Larochelle, A Talebpour, and S L Chin. Coulomb effect in multiphoton ionization of rare-gas atoms. *Journal of Physics B: Atomic, Molecular and Optical Physics*, 31(6):1215, 1998.

[197] H.J. Lehmeier, W. Leupacher, and A. Penzkofer. Nonresonant third order hyperpolarizability of rare gases and n2 determined by third harmonic generation. *Optics Communications*, 56(1):67 – 72, 1985.

[198] David P. Shelton and Julia E. Rice. Measurements and calculations of the hyperpolarizabilities of atoms and small molecules in the gas phase. *Chemical Reviews*, 94(1):3–29, 1994.

[199] Á. Börzsönyi, Z. Heiner, A.P. Kovács, M. P. Kalashnikov, and K. Osvay. Measurement of pressure dependent nonlinear refractive index of inert gases. *Opt. Express*, 18(25):25847–25854, Dec 2010.

[200] C. Bree, A. Demircan, and G. Steinmeyer. Method for computing the nonlinear refractive index via keldysh theory. *Quantum Electronics, IEEE Journal of*, 46(4):433–437, April 2010.

[201] J. K. Koga, N. Naumova, M. Kando, L. N. Tsintsadze, K. Nakajima, S. V. Bulanov, H. Dewa, H. Kotaki, and T. Tajima. Fixed blueshift of high intensity short pulse lasers propagating in gas chambers. *Physics of Plasmas*, 7(12):5223–5231, 2000.